Solar Orbiter / RPW and SWA-EAS numerical simulations with the SPIS software

RPW-EAS-SYS-TN-001760-LES-MSSL

Prepared and approved after verification by:	Function:	Signature:	Date
Stanislas Guillemant	Research Engineer		01/10/2016
Verified by:	**Function:**	**Signature:**	**Date**
The RPW Team			
The SWA-EAS Team			

CLASSIFICATION : PUBLIC ☒ **RESTRICTED** ☐

l'Observatoire de Paris | LESIA
Laboratoire d'Études Spatiales et d'Instrumentation en Astrophys

CNRS-Observatoire de PARIS
Section de MEUDON – LESIA
5, place Jules Janssen
92195 Meudon Cedex – France

Change Record

Issue	Rev.	Date	Authors	Modifications
1	1	17.10.2016	S. Guillemant	Creation and inclusion of RPW part
2	1	18.04.2017	S. Guillemant	Inclusion of EAS part

Acronym List

Acronym	Definition	Acronym	Definition
EAS	Electron Analyzer System	PAS	Proton-Alpha Sensor
EMC	Electro Magnetic Cleanliness	SEE	Secondary Electron Emission under ambient Electron impact
HIS	Heavy Ion Sensor	SEEP	Secondary Electron Emission under ambient Proton impact
S/C	Spacecraft	SA	Solar Arrays
RPW	Radio & Plasma Waves instrument	SolO	Solar Orbiter
SWA	Solar Wind Analyzer	SPIS	Spacecraft Plasma Interaction System

Table of Contents

1. General

This document presents in a first part numerical simulation results and output analysis of the Solar Orbiter - RPW modelling work on the spacecraft electrostatic environment using the Spacecraft Plasma Interaction Analysis and Simulation Toolkit (hereafter referred to as SPIS). This modelling was necessary to precisely estimate the effect of the Solar Orbiter spacecraft platform on the RPW ability and performances to measure the DC/LF electric fields and satellite potential in the Solar Wind.

The tasks required include providing a detailed and adaptable model of the Solar Orbiter spacecraft together with the definition of the characteristics of those surfaces which will be exposed to the space environment and that will have, or may possibly have, an effect on the electrostatic environment measure by the RPW Antennas.

In a second part, this document will present numerical simulations results and output analysis of the Solar Orbiter – SWA-EAS modelling work. Numerical simulations are the only mean to make a realistic and accurate quantitative model of the satellite induced perturbations on instrument measurements. Older SPIS developments have enabled the user to add scientific instruments (Langmuir probes, particle detectors, …) in the simulation domain as to mimic expected measurements.

The tasks required here include providing a detailed and adaptable model of the Solar Orbiter spacecraft together with the definition of the characteristics of those surfaces which will be exposed to the space environment and that will have, or may possibly have, an effect on the electron population (*e.g.* modification of trajectories of electrons entering the instrument) to be measured by the SWA-EAS instrument. Model runs should be performed using realistic parameters representing the environments to be sampled by Solar Orbiter (*i.e.* over distances of 0.28 to 1.4 AU), in order that the major perturbations to the environment, and their effects on the SWA-EAS measurements can be identified and quantified. Moreover, capacity should be built in order to provide the means, in the post-launch period, to run the models for specific environments encountered and/or to assess the impact of a varying (or previously unanticipated) perturbation to the ambient plasma environment. The presence of an eventual baffle set behind EAS instrument will also be investigated, concerning its effects on EAS outputs, especially regarding the secondary electron pollution on measurements

2. Context

➢ Introduction

In this report are presented numerical simulations of spacecraft/plasma interactions, focused on electric field measurements within the Solar wind.

The satellite studied is the future ESA Solar Orbiter mission (also called SOLO in this report), scheduled for a launch in 2018 with a NASA participation, which is dedicated to solar and heliospheric physics. It has been selected within the ESA Cosmic Vision Programme 2015-2025. Solar Orbiter will study, through a combination of in-situ and remote sensing observations the heliosphere and its magnetic field, the solar wind and solar energetic particles among other phenomena. It will provide close-up, high-latitude observations of the Sun. Solar Orbiter will have a highly elliptic orbit: between 0.9 Astronomical Unit (AU) at aphelion and 0.28 AU at perihelion. Electric field measurements will be performed through the deployable antenna system provided by Stellar Scientific: the Radio and Plasma Waves (RPW) instrument.

In the Solar wind and especially at its perihelion the whole spacecraft will be submitted to an intense electromagnetic radiation flux (10 times that at Earth) leading to specific thermal and spacecraft plasma interactions issues. For instance, fluxes of low energy secondary and photoelectrons, emitted by the spacecraft itself, and deflected towards instruments by local electrostatic structure. The local plasma potential is indeed modified by various spacecraft induced effects such as the charging of covering material, the presence of an ion wake and high secondary electron / photoelectron densities, which in turn might affect any measurement. Numerical simulations allow comprehension of such events.

Simulations will be performed using the Spacecraft Plasma Interaction System (SPIS). This software toolkit allows spacecraft-plasma interactions and spacecraft charging modelling. Initiated by ESA including CNES support and following an open-source approach in the frame of the Spacecraft Plasma Interactions Network in Europe (SPINE) community, it is developed in an Open Source approach and oriented towards a future community-based development. The 5th version of the code used in this study has been recently delivered and allows modelling of satellite scientific instruments and associated measurements (particle detector, Langmuir probes…).

➢ Measuring a DC field with the RPW experiment

The principle of measuring DC electric fields by the RPW instrument is summarized on Figures below. In the solar wind and in the absence of an external electric field (*E*) the 3 RPW antennas, which are all in the $(Z,Y)_{SC}$ plane and are thus equally illuminated, in the ideal case would float at the same potential ($\Phi_1 = \Phi_2 = \Phi_3 = \Phi$). Note that the antenna potentials are potentials respect to the plasma ($\Phi = 0$ far from the antennas). This floating potential will mainly depend on the density of the Solar Wind and will roughly vary between a few Volts to a few tens of Volts, as can be seen in the lower left corner of Figure 1 for a zero bias current. On this Figure it can also be seen that when a bias current is applied, the floating potential of each antenna will exhibit much lower amplitudes of variation around a value closer to the plasma potential. In reality, the potential of each antenna will in addition be affected by the electrostatic environment of the spacecraft. This results in systematic measurement errors on the DC/LF *E* field and satellite potential that has to be assessed. Therefore, it is important to study those aspects of the spacecraft that affect most the electrostatic environment of the spacecraft and particularly the RPW antennas.

When an external electric field $\vec{E}$ is present in the plasma, then the electric potentials of the antennas are modified in a way which is described in Figure 2. In this case the difference of potential between two antennas is equal to $\vec{E} \cdot \overrightarrow{L_{eff}}$, where $\overrightarrow{L_{eff}}$ is the antenna effective length vector in DC.

These vectors constitute one of the main calibrations parameters for the RPW DC/LF measurements. They can be modelled using SPIS.

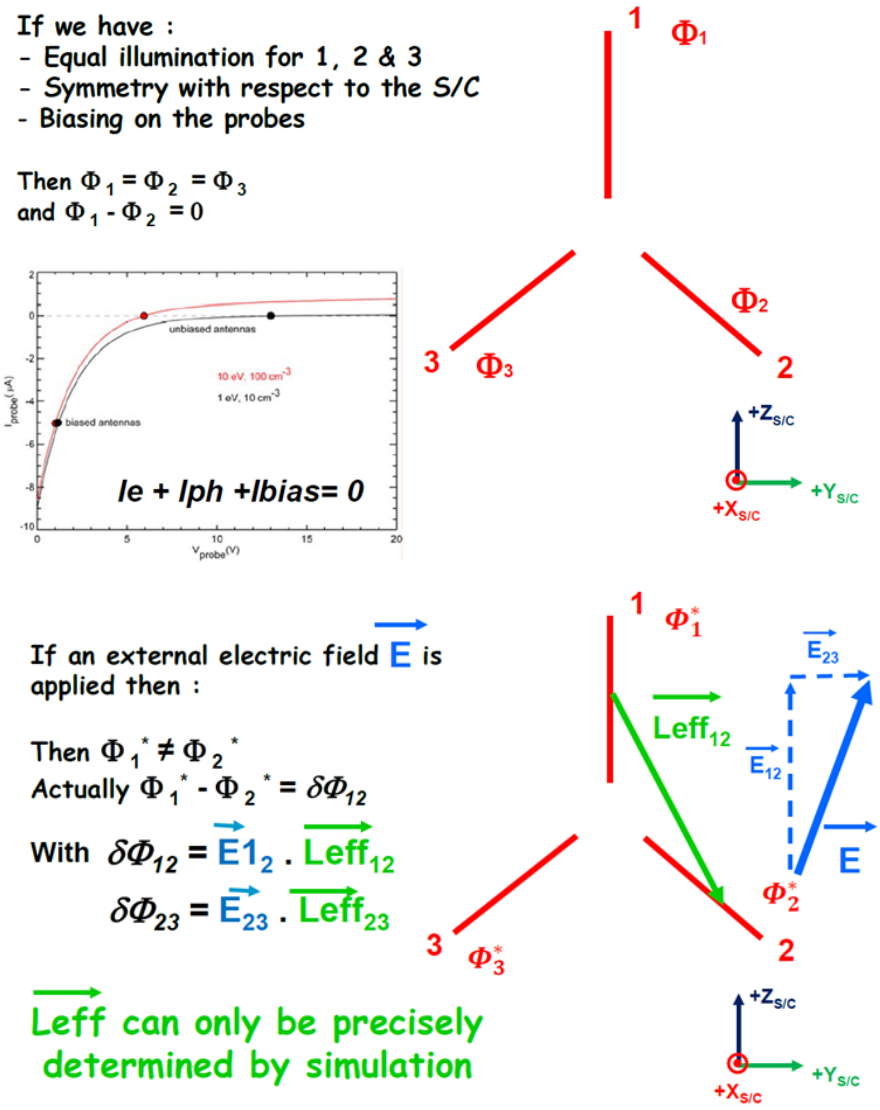

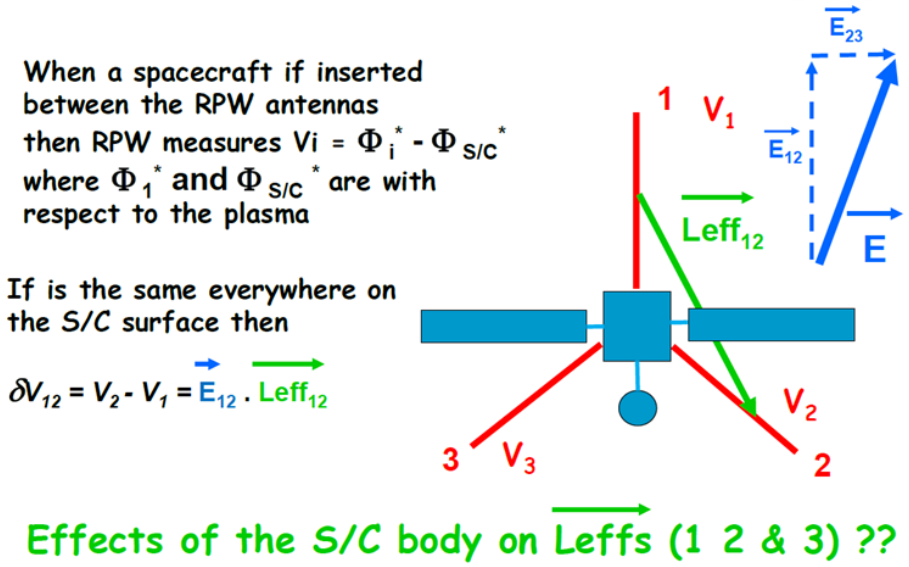

3. Spacecraft and instrument modelling

This phase is performed through the GMSH software embedded in SPIS (a 3D finite element grid generator with a build-in CAD engine and post-processor). Combining the interactive graphical user interface or ASCII text files using Gmsh's scripting language, the user generates .geo file(s) that will be used by SPIS for the simulation. The geometry should contain:

• The external boundary, corresponding to a priori the undisturbed plasma and made of one closed surface;

• The computational volume corresponding to the surrounding plasma;

• The inner boundary which stands for the spacecraft structure, defined by one or several closed surfaces.

The user has to define within the geometry what the physical elements are that SPIS will have to deal with, such as the external boundary, the computational volume and the different physical surfaces of the satellite.

Within the GMSH phase of geometry construction, the user defines the meshing grid size on each point of the satellite structure. The mesh dimension also has to be defined on the external boundary. One particular specification of the meshing for SPIS is that the size of any surface cell or volume element must be inferior to half of the local plasma Debye length (meaning that near the satellite the eventual secondary and photoelectron populations should be taken into account for the Debye length estimations). Furthermore, meshing on spacecraft or instrument surfaces should contain more than one cell per surface. This seems obvious but it is necessary to obtain a correct modelling of particle/surfaces interactions, with an acceptable local resolution of current balance. This might thus generate an impressive total number of cells when the geometry contains very small elements.

Important: geometry of satellite and RPW system evolved during this study. First studies presented in this report were performed several months ago when some SC geometry elements and characteristics weren't totally defined and still under reflection. Lots of simulations have been performed considering older spacecraft model (dimensions, configuration…) and different covering materials (type and properties). In this report we present old and recent cases meaning that models and corresponding materials considered are not necessarily up-to-date. New information concerning precise dimensions, materials and configuration were provided all through this study and last updates few days ago, which implied new urgent simulations. In any case some of them are still likely to be changed in the next future: this is why simulation inputs supplied with this work are up-to-date for now but easily modifiable

in order to update CAD models and SC configuration for further new series of in-depth studies in order to test other Solar Orbiter structure evolutions.

In the same manner old simulations were considering an outdated reference frame for SolO. This doesn't change global results but only alters convention of presenting outputs. Recently the official Solar Orbiter XYZ reference frame has been applied for the last presented cases. X axis points the Sun, normal to SC heatshield, Y axis perpendicular to X aligned with solar arrays rotation axis, and Z parallel to the upper RPW antenna (RPW1). Last CAD model is up-to-date.

3.1. RPW modelling

The RPW system (Figure 1) is way too complex to be modelled as it is in GMSH. SPIS simulations have to consider simplified geometries. RPW main elements supposed to have the most important influence for the spacecraft/plasma interaction simulations have been identified and retained. These are the boom, the preamp, the heat shield and the stacer, which have been designed in GMSH.

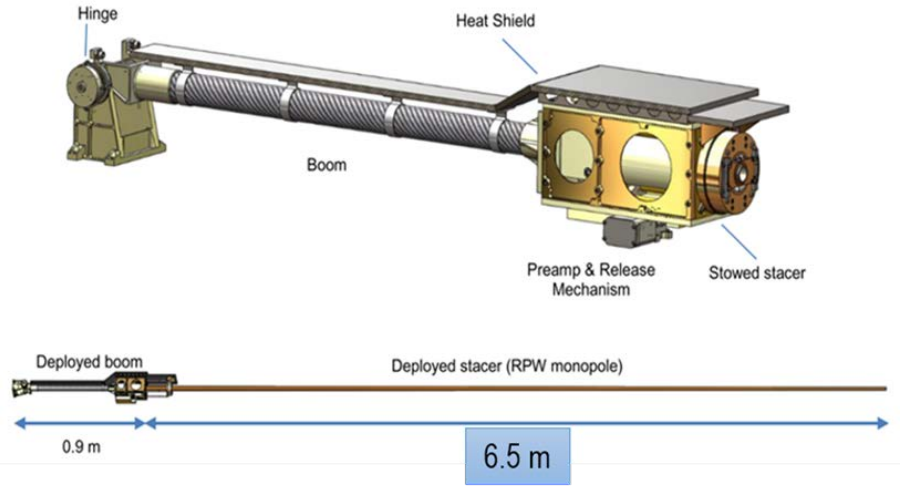

Figure 1 : RPW antenna configuration

It is possible to model wires and booms using the usual and realistic 3D tubes or simplified 1D thin wire models. The 3D model has several constraints. Even though it is more precise and closer to reality, conditions about meshing of the tube are quite heavy. In order to obtain a precision on the charging potentials inferior to 5%, it is necessary to mesh the antenna with cell size (*dx*) smaller than the radius *r*/8.

In the case of the RPW geometry with a maximum radius of 1.4 cm close to the pre-amplifier, it gives *dx* for the meshing as small as 1.75 mm. As we have 3 antennas of 6.5 m long plus 3 booms of 60 cm long composing the RPW experiment, the number of tetrahedra obtained in the simulation box exceeded few millions, leading to extremely long durations of computations, provided that powerful computers with huge amount of available RAM capacities are at disposal. This was not possible in the context of the parametric study needed by LESIA. Rising the dx size to *r*/4 leads to a misleading of the potentials of 15%, with still a number of tetrahedra unacceptable for respecting the delays. However, a 3D CAD model of RPW has been generated and is available with other CAD files used for this study.

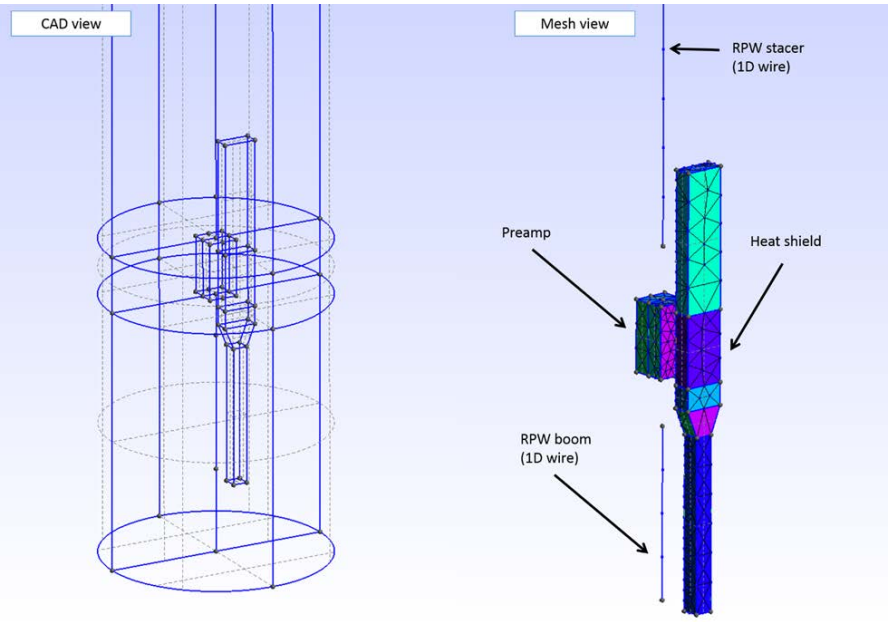

Figure 2 : GMSH modelling of RPW antenna

The 1D modelling method (Figure 2) is much better for the meshing constraints: we need to respect $dx > 10\ r$ (r being the "virtual" radius of the antenna, it does not appear in GMSH but is configured during the SPIS setting of the simulation). In our case dx must be larger than 14 cm to avoid jumps of potentials between two cells on the wire. The amount of cells in the simulation box thus becomes much adapted for the computation duration (few tenth of thousands tetrahedra). However, this dx generates issues due to the proximity of several small elements (bottom of RPW, top of the boom, pre-amplifier and sunshield of the RPW).

In SPIS it is necessary to have more than one single tetrahedron between two different physical elements. As in this configuration the RPW parts are extremely small and close to each other, in order to respect the ratio dx/r, it was necessary to enlarge the spatial gap between them, to increase the heat shield thickness and also to locally adapt the mesh size on those element surfaces to ensure the quality of the grid and avoid a too large number of cells due to small dx values. It is also necessary to avoid any direct contact between two different physical elements. This means that in our model all main RPW elements will be physically disconnected, even though they will be electrically related. With this type of configuration SPIS will work on a multi-scale simulation, considering elements of sizes varying between few millimetres (the stacer radius, the heat shield thickness) to several meters (the antenna length, the simulation box dimension). Consequently, the mesh size dx will be locally adapted to those elements dimensions: for instance, $dx \sim$ few centimetres in the vicinity of the preamp to several meters on the boundary of the simulation box.

After their dimension measurements according the STEP file model of the instrument (provided by ESA), the geometries and spacing have been adapted for the GMSH model. A refinement mesh box appears on Figure 3. It aims at controlling the meshing size extension in the vicinity of small elements and also generate the thin wires constituting the 3 RPW antennas and the 3 booms (through two planes intersection within those boxes). As explained previously: the various modelling constraints required to increase the heat shield thickness (from 6 mm in reality to 5 cm here). The gap between the shield and the protected elements behind it has been enlarged (12 mm to 12 cm). A 5 cm physical gap between the preamp and the two wires has been created. The boom length is therefore reduced of the same value but the RPW antenna length is conserved (6.5 m). Booms and stacers being modelled as 1D thin wires, the virtual radius are entered directly in SPIS. For the perfectly cylindrical booms 1.5 cm for the booms.

For the stacers, the real configuration is based on a conical tube with a tip diameter of 1.8 cm and a base diameter of 2.8 cm. As for SPIS the wire radius is a constant, the average radius of 1.15 cm is retained.

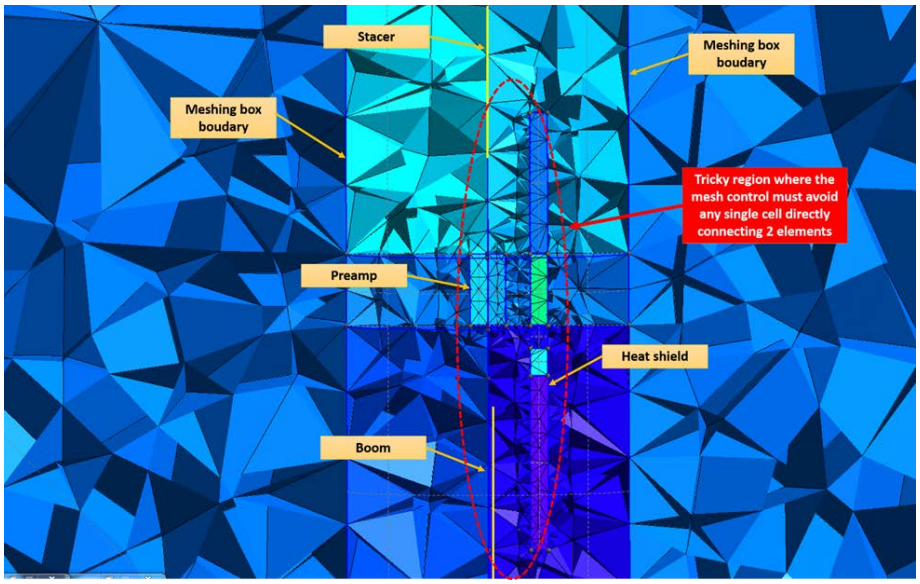

Figure 3 : Cutting plane of the meshing of RPW1 focused on the preamp, viewed in the Y-Z plane. Each meshed physical element is identified. The key region where the grid must be properly investigated is circled in red.

Real RPW system allows injection of biasing current in the antennas, in order to bring stacer potentials as close as possible to local plasma potential. Those I_{bias} currents can vary independently between +/- 70 µA, with 1024 possible steps, and will be injected with a precision inferior to 0.15 µA. Electric potential of any antenna with respect to the SC ground can be measured with an accuracy of 2 mV. It is thus possible to generate I_{bias}-V_{RPW} curves, characterizing antenna's response to the total current balance. This parametric study will also be performed in the following.

3.2. Spacecraft modelling

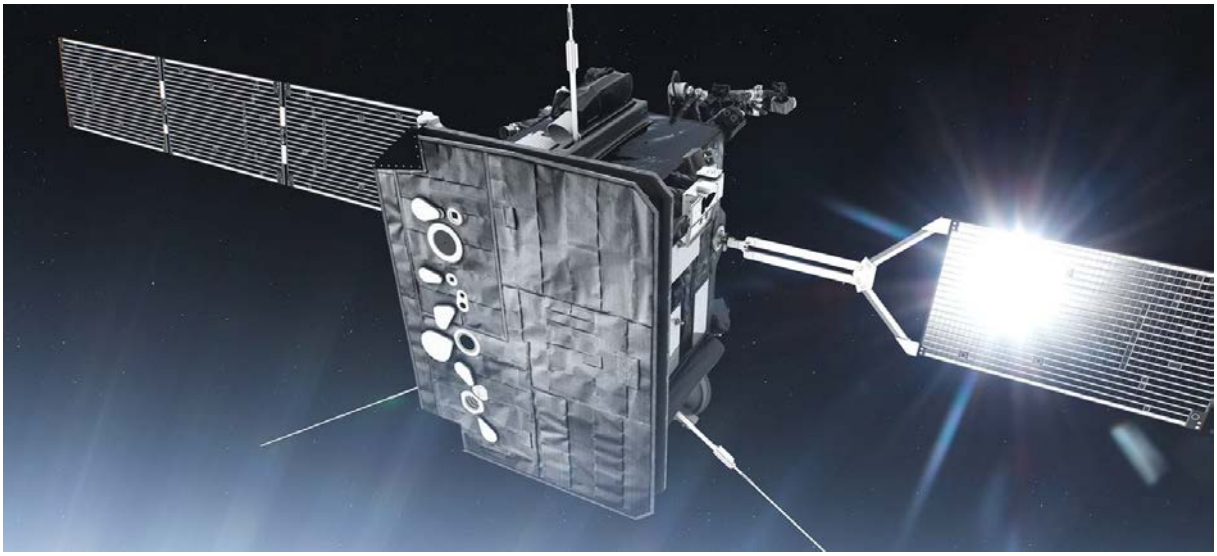

Figure 4 :Artist view of Solar Orbiter spacecraft (credit : ESA)

SolO (Figure 4) remains a complex satellite that also had to be simplified as a CAD model for SPIS simulations. Important points to be considered and respected are localisation, dimensions and properties of non-conducting elements which will be charged to different electrostatic potentials and might thus disturb RPW measurements. Also, elements in the vicinity of RPW antennas should be carefully reported as they will emit secondary particles (photoelectrons, SEEE and SEEP) which will surround and possibly contaminate the stacers. A specific care has also been observed to respect as much as possible the real satellite dimensions in general.

Main dielectric elements that cannot be neglected during simulations are the 2 solar arrays sunlit faces, so as the 2 yokes sunlit faces. Yokes are those "Y"-shaped elements connecting solar arrays to SC body, possibly rotated around their main axis (*Y* in the Solar Orbiter reference frame) with an angle (SAA) depending on the heliocentric distance (Figure 5). This angle varies as follows, considering the heliocentric distance "*d*":

- d > 0.9 UA, Angle=0°
- 0.75 UA < d < 0.9 UA, Angle=30°
- 0.55 UA < d < 0.75 UA, Angle=60°
- 0.45 UA < d < 0.55 UA, Angle=70°
- 0.28 UA < d < 0.45 UA, Angle=76.5°

In this study we focus on Solar Orbiter perihelion environment conditions. SAA is thus set at 76.5° *w.r.t. X* axis for the last cases. As explained above-mentioned, old simulations considered a null angle which means a solar panel fully normal to the Sun. Note that for first simulations, yokes and rotation angle of solar panels are not yet considered.

The spacecraft CAD model used for the first set of simulations is displayed on Figure 6, and the computational meshed volume considered on Figure 7.

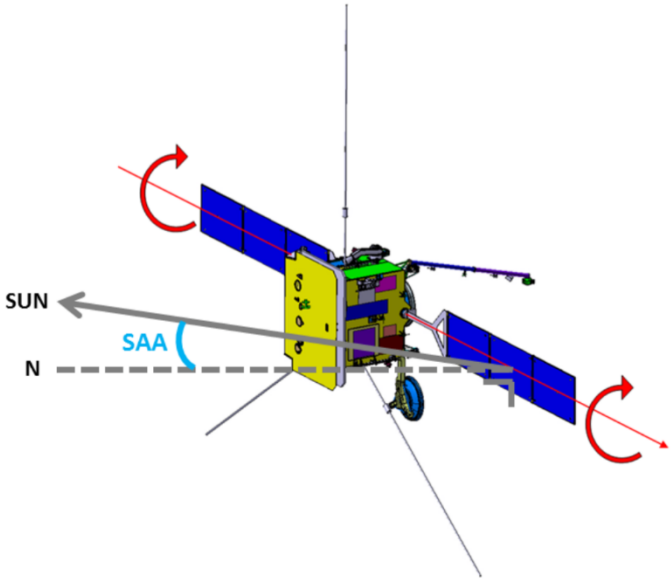

Figure 4-1: Solar Array Steering

The Solar Aspect Angle (SAA) is defined as the angle between the direction of the sun vector and the normal vector to the solar panel (SAA is 0° if the sun vector is perpendicular to the solar array surface and 90° if parallel). See RD1 section 5.5.4 for the SA reference frame

Figure 5 : Definition of Solar Aspect Angle (SAA)

Note also that angles between RPW antennas 1, 2 and 3 are not identical. Angle between 1 and 2 equals to 125°, as for the angle between 1 and 3, while the one between 2 and 3 is smaller (110°). This also appears on the following Figure 6.

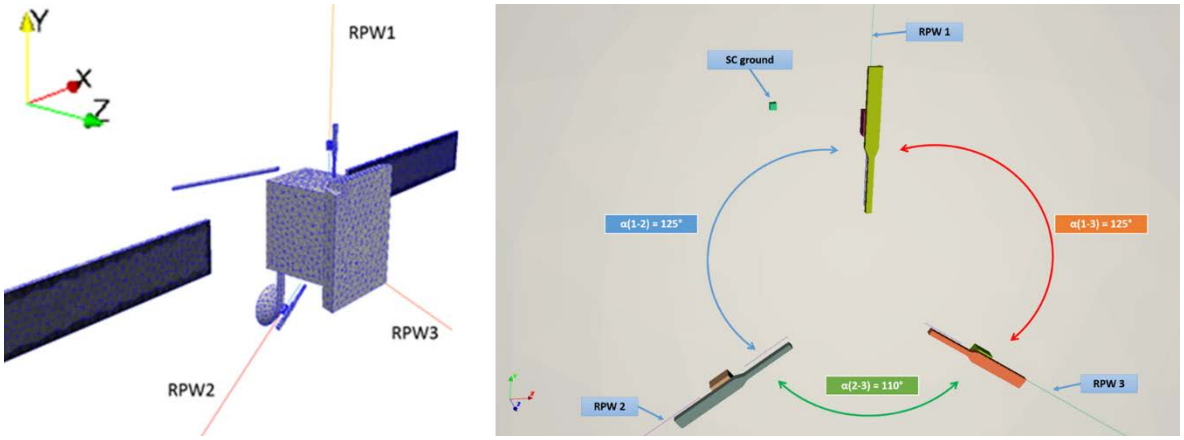

Figure 6 : GMSH CAD model of Solar Orbiter

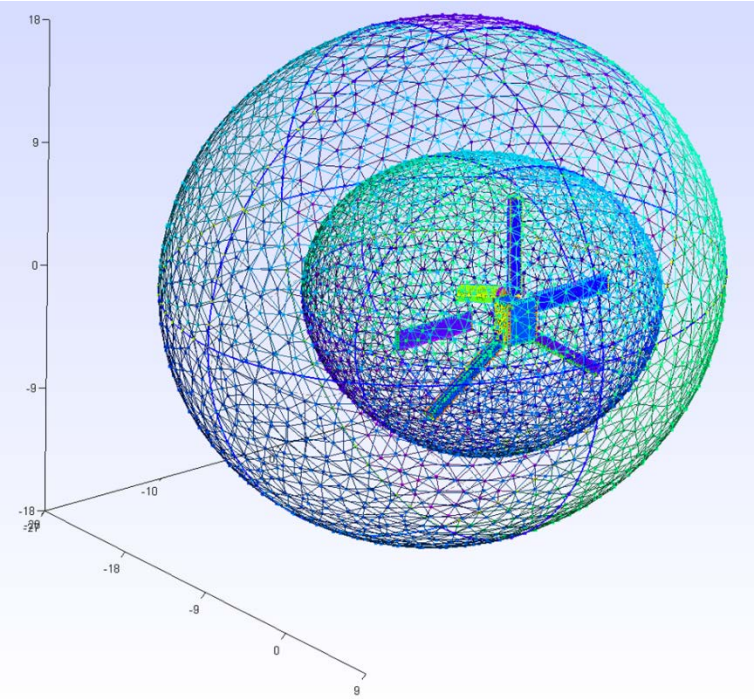

Figure 7 : GMSH meshed model of Solar Orbiter in its simulation volume

3.3. Materials

Here are covering materials used in SPIS to model Solar Orbiter. Preliminary simulations simplified the system by considering only few different materials on the structure. Note that the three RPW stacers were defined as gold wires (according to the previous RPW technical configuration). Those materials will change in further simulations as new updates have been provided during this work.

Elements	Material
SC body, HGA, HGA mast, rear Boom	Black Kapton (BK2K)
SC sunshield	Steel (STEE)
Rear SA faces and sides, RPW shields preamp and boom	Carbon Fiber (CFRP)
Front SA faces	Solar Cell (CERS)

In further simulations, new SC elements and covering materials have been implemented. It will be specified when those cases will be introduced.

3.4. Electrical circuit

All physical elements are directly grounded to the Spacecraft mass. Only the 3 stacers are decoupled of the system. In the real configuration it is planned to link each monopole to its corresponding preamp through an impedance made of a 10 MOhm resistor mounted in series with a 60 pF capacity. However, in SPIS the series coupling between two electrical nodes is not implemented yet. We thus neglect the resistor and impose a single capacity CRPW to impose the decoupling between ground and monopoles. The cubic satellite, the booms, shields and preamps will with this configuration float to the same electrostatic potential (which value will depend on the plasma conditions). On the contrary, each RPW stacer will have its own steady potential. 4 potential values are therefore expected by the end of each simulation.

Note that the coherence of the real stacer capacitive coupling and CRPW is not important for this study. It will only affect the duration necessary to reach the equilibrium potential on the antennas, and the fluctuation rate of this potential due to statistic variations of particles and currents arriving on the wires. Large capacities imply too long simulation durations while too small values generate strong potential variations which are not compatible with the degree of precision expected for this study.

This is also the case for the Spacecraft capacity C_{SC}, which can be seen as "component" capacitor plugged between the spacecraft at plasma ground located at infinity. Electrodes are indeed the charges on top of spacecraft surfaces and in its sheaths. This capacitance value depends on plasma conditions. It occurs that after several simulation tests: the only way of maintaining of relative stability and coherence between the various potentials is to set $C_{SC} = C_{RPW}$. Indeed SPIS cannot handle $C_{RPW} << C_{SC}$ (the circuit solver encounter numerical issues in this case) and if $C_{RPW} < C_{SC}$ the monopole potentials fluctuate so much that their respecting values over time cross the others, leading to high difficulties to estimate average potential gradients between the stacers. The tests also concluded that the ideal capacity value for the environment here considered (Solar Orbiter at 0.28 AU from the Sun) is to be 10^{-6} F, to ensure acceptable simulation durations.

3.5. Environment

The plasma conditions considered for this first set of simulations are those at 0.28 AU from the Sun. This region is indeed the perihelion of Solar Orbiter, its closest position to the Sun and therefore the worst conditions concerning particle density and temperature, solar flux, photoemission and secondary electron emission rates. SPIS being a Particle-In-Cell (PIC) code, it is possible to set different particle generation and transport processes. In this study main parameters are set as follow:

- Ions: H+, PIC with Maxwellian distribution and drift,
- Electrons: PIC with Maxwellian velocity distribution function,
- Photoelectrons: PIC with Maxwellian velocity distribution function and with a characteristic temperature $k_B T_{ph}$ = 3 eV,
- Secondary Electrons under Electron impact (SEEE): PIC with Maxwellian velocity distribution function and with a characteristic temperature $k_B T$ SEEE = 2 eV, backscattered electrons with 2/3 of their initial energy,
- Secondary Electrons under Proton impact (SEEP): PIC with Maxwellian velocity distribution function and with a characteristic temperature $k_B T$ SEEP = 2 eV,
- External boundary conditions: Fourier, 1/R2 decrease of potential

Environment parameters	Values at 0.28 AU from the Sun
Sun flux (# 1 AU)	12.76
Electron and Proton density (m^{-3})	1.04×10^8
Electron temperature (eV)	21.37
Proton temperature (eV)	27
Spacecraft velocity in X direction (m/s)	60000.0
Proton bulk velocity in Z direction (m/s)	-400000.0

In SPIS it is not possible to generate an electric field directly over the plasma volume. Only the E field generated by electrostatic charging of satellite surfaces is considered. In this case the spacecraft is considered as motionless and the plasma is moving through the simulation box (with thermal and/or bulk velocities set by user).

In order to create E we have to impose a magnetic field (uniform and time constant over the simulation box), and impose a velocity to the spacecraft. In SPIS the reference basis of the magnetic field is the one of the plasma, as in the Solar wind the plasma is “frozen” in the magnetic field. So

simulating a physical case using B fixes the reference basis of the simulation where V_{plasma} = 0. In this basis we have to set the spacecraft velocity in the reference of the plasma *V*, combining both plasma bulk velocity (related to the solar wind velocity) and the satellite motion over its orbit.

Finally, the "V cross B" electric field generated over the simulation box, constant and uniform, is expressed as: $E=V\times B$. At perihelion the electric field induced by the magnetic field will also be the highest as *B* is stronger close to the Sun. This last environment characteristic will be considered later.

4. Simulation results with older SolO configuration: first estimations about SC and RPW behaviour

4.1. Case 1: SolO @ 0.28 AU without B

➢ SC Potentials

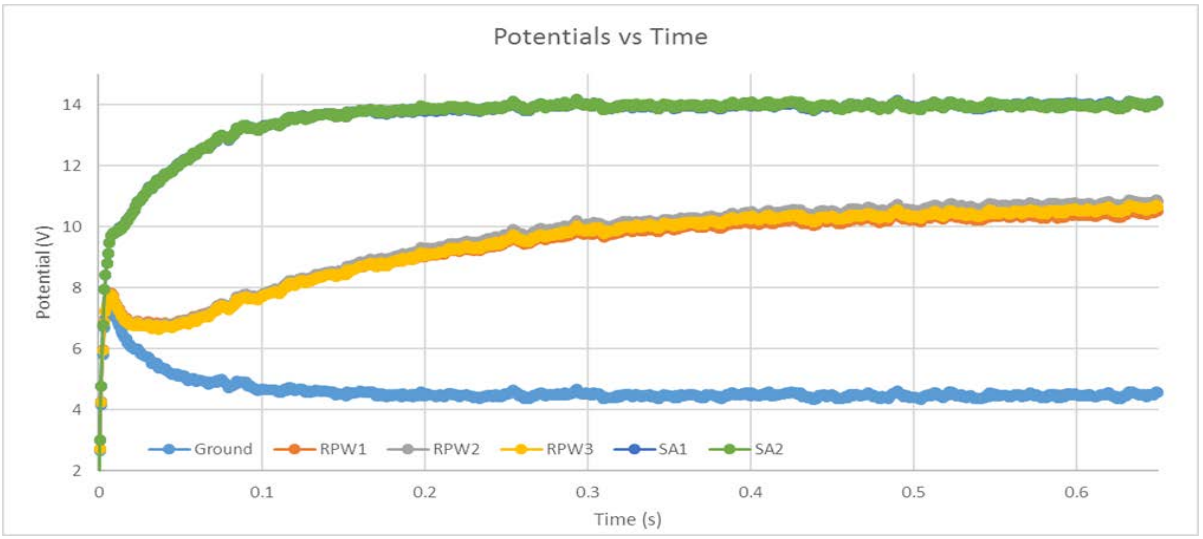

Figure 8 : Case 1 - Time evolution of SC potentials

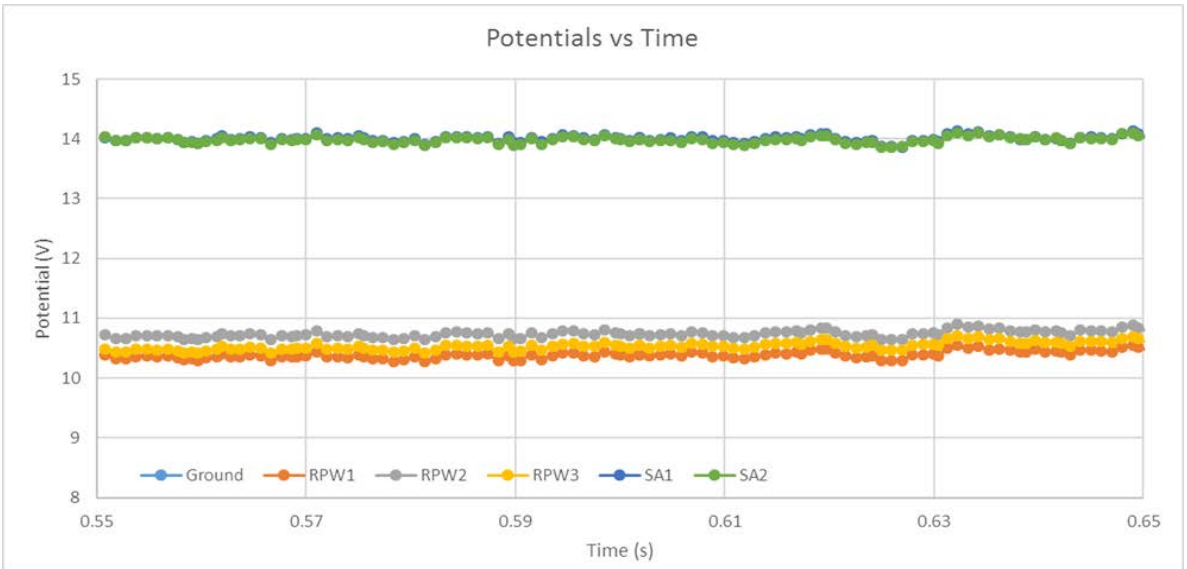

Figure 9 : Case 1 – Focus on Time evolution of SC potentials

In this case, no yokes, no rotated solar arrays. No imposed magnetic or electric field either. We do not inject any biasing current in the antennas.

With this simulation configuration, the equilibrium is reached after a numerical duration of 0.5 s. Because of potential fluctuations we have to reason in terms of average values for potentials and currents, in order to determine the final state of the RPW system. This increases the duration of the post-processing phase of simulations but obviously enhances the precision of the results. Average values are calculated from t = 0.55 to 0.65 s.

Evolution of electrostatic potentials on the different satellite elements over time are presented on Figure 8 and Figure 9. Spacecraft and other grounded elements (booms, heat shields and preamps) are at the same potentials. In the following each monopole will be called RPW# for simpler notation. Mean potential values are in this case:

In average *after t = 0.55 s*	Potential Φ(V)	Standard deviation σ(V)
SC ground	**4.48**	0.05
RPW1 (+Y)	**10.39**	0.06
RPW2 (-X)	**10.74**	0.06
RPW3 (+X)	**10.54**	0.07
SA1(-X)	**14**	0.05
SA2(+X)	**13.98**	0.05

We remind that RPW2 and 3 are closer to each other than to RPW1, because of the smaller angle between them (110°). It appears that without B and E the monopoles are practically charged at the same potential, as expected given the symmetry conditions of this simulation case. We notice a good stability of the results, practically no difference between antennas potentials (max ~3%). Potential discrepancy is due to numerical/statistical issues (inherent to PIC codes), low SC capacitance and probably small meshing differences at some RPW regions leading to particle collection disparities.

Solar panels are highly charged compared to SC ground. This is simply due to the fact that here there is a quite non-realistic situation with arrays completely normal to sun direction. We might asses that in further simulations with inclined SA planes: the potential reached on CERS surfaces won't be so important. Here the print of electrostatic potential generated by solar cells outflanks their area until appearing in the spatial plane containing the 3 RPW antennas… Problematic for electric fields measurements.

➢ Plasma in volume

Concerning the plasma, we present in Figure 10 the electrostatic potential. It shows that small irregularities along wires remain due to meshing issues, without consequences on the charging values. Even when reworked, the automatically generated mesh can contain irregular cells. The potential structure in volume looks symmetric due to the absence of imposed *V* cross *B* electric field. Negative potential areas are present in the wake (due to a lack of positive charges in the ion wake, combined with secondary electron populations emitted by all SC surfaces), and in the ram (strong densities of photoelectrons + SEEE + SEEP).

Concerning particles density in the volume, a light wake effect on ions appears on this Figure due to proton bulk velocity and physical obstacles (including the 1D wires). The ion wake clearly appears. High densities of photoelectrons, secondary electrons under electron impact (SEE) are present around RPW elements (Figure 11). These are due to the environment conditions: strong UV flux and high densities of impacting particles. The densest population are photoelectrons, meaning that their current on RPW elements will be the highest. For instance at 2 cm of RPW1, the amount of photoelectrons

reaches 1.6×10^{9} m^{-3}, and at 30 cm from the stacer this density decreases to 1.6×10^{8} m^{-3} *i.e.* still higher than ambient electron density (1.04×10^{8} m^{-3}).

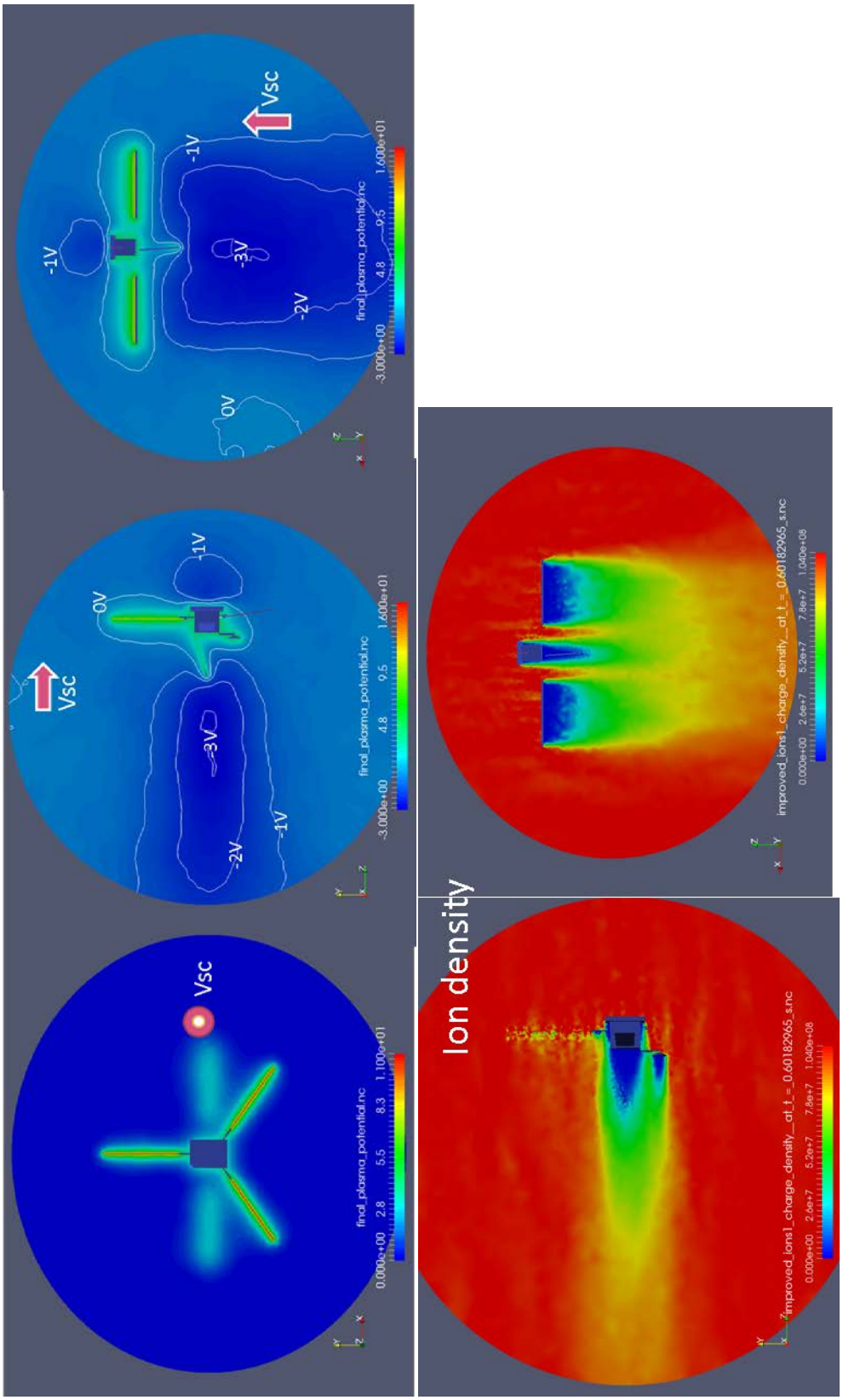

Figure 10 : Case 1 - Plasma potential (on top) and ion density (bottom) in several cutting planes of the simulation volume

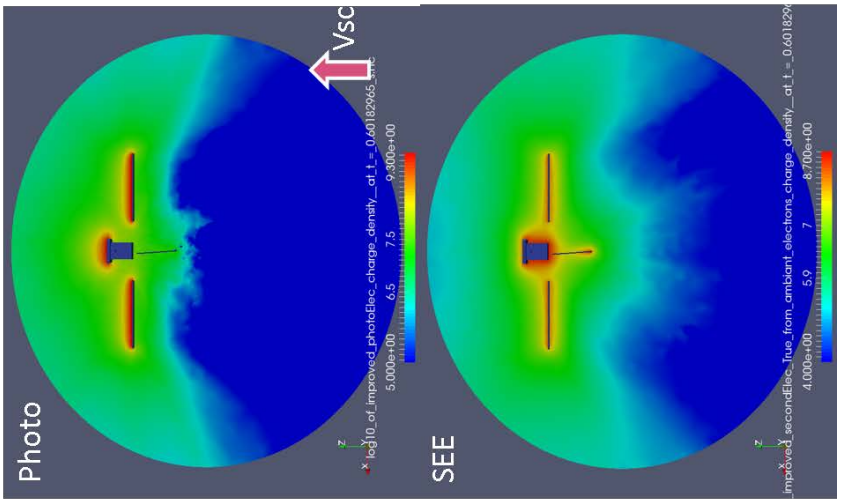
Photo
Vsc
SEE

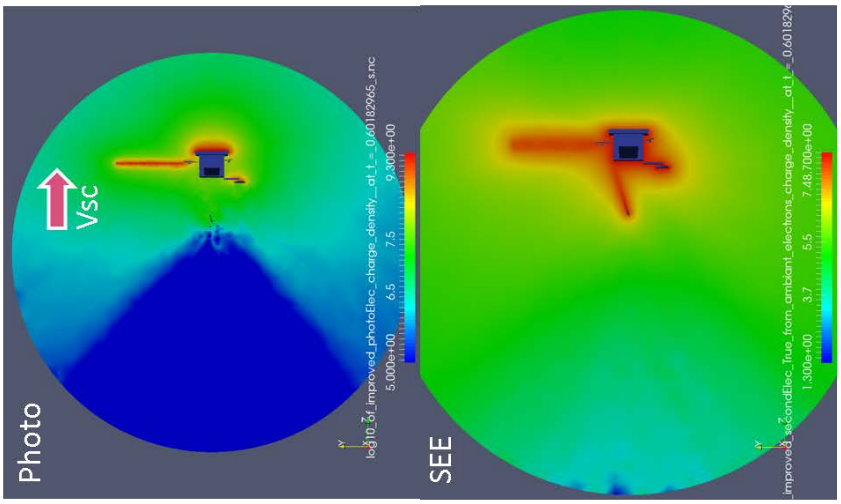
Photo
Vsc
SEE

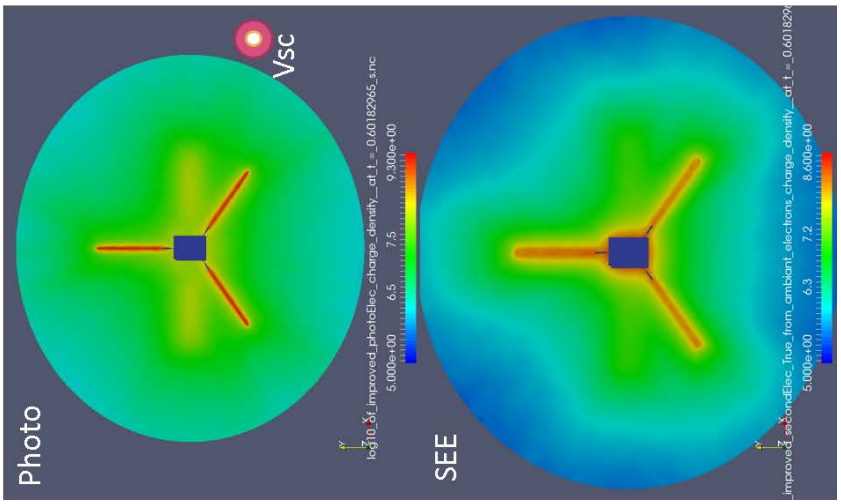
Photo
Vsc
SEE

Figure 11 : Log of Photoelectron density (top) and SEEE density (bottom)

➢ Conclusion.

This first and simplified case gave a good idea of general spacecraft behaviour when this one is immersed in the perihelion environment. Strong photoelectron emission, mainly contained in the ram region of the structure. High densities of SEEE and SEEP which totally surround the satellite and its instruments. RPW themselves are powerful sources of secondary particles. Potential discrepancy of stacers also appears. We should have in an ideal situation the same potentials reached on RPW1, 2 and 3 surfaces as they are equally illuminated and exposed to a "symmetric" environment. However, due to even small local meshing differences and numerical issues inherent to PIC codes we find a 3% gap between antenna potentials. Note that RPW2 and 3 are closer to each other, and to the "HGA + solar arrays" combination which remains a source of positive charging and secondary particles.

4.2. Case 2: SolO @ 0.28 with a magnetic field

Including now to the previous case 1 a non-realistic magnetic field *Bx* = 0.8 µT. SolO design remains unchanged (Figure 12).

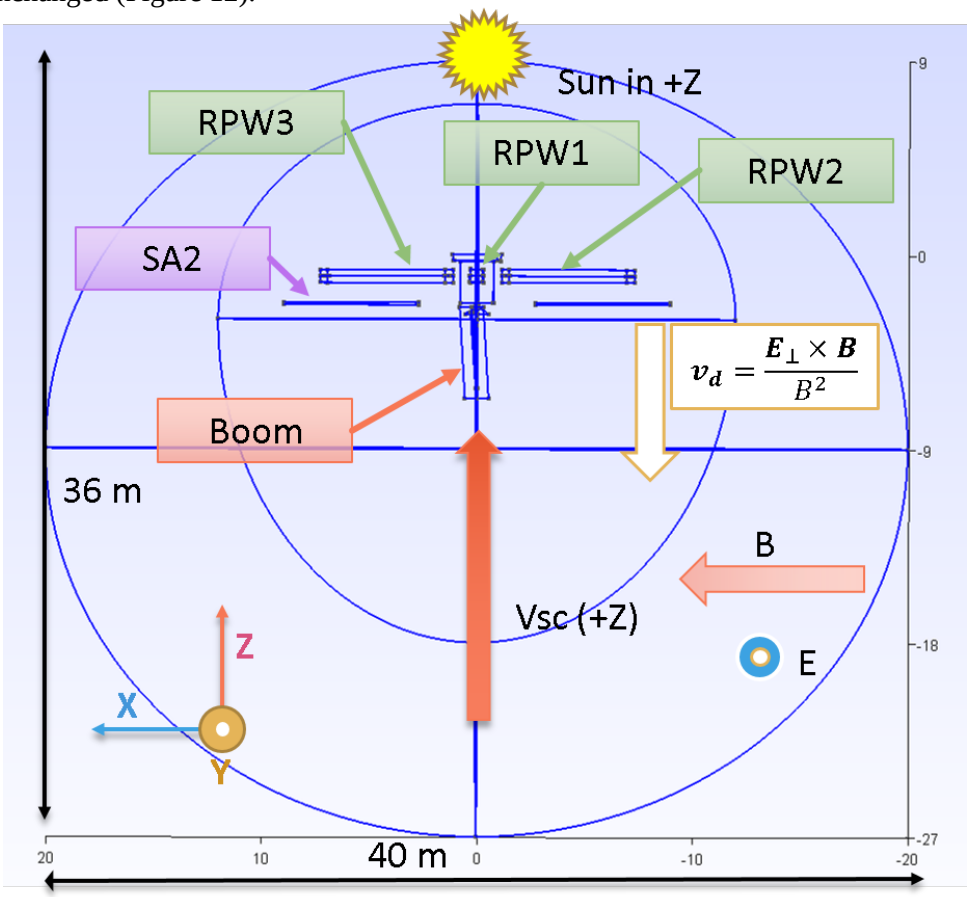

Figure 12 : Global configuration of SolO and V cross B electric field in Case 2

Simulating a physical case using *B* fixes the reference basis of the simulation where the plasma velocity $V_{plasma} = 0$. In this basis we have to set the spacecraft velocity in the reference of the plasma *V*, combining both plasma bulk velocity (related to the solar wind velocity) and the satellite motion over its orbit. In this case, $V_{protons} = 0$, and for the spacecraft $V_{SC\_Z} = 4\times10^5$ m/s.

Finally, with this new configuration the resulting *VxB* electric field is $\boldsymbol{E} = E_Y \boldsymbol{e_Y} = 0.32$ V/m

The magnetic field forces the electrons to be magnetized (the field in the simulation is intentionally much stronger than in the real wind in order to emphasize a strong electric field on the RPW antennas). Indeed, in the spacecraft frame magnetized particles (with a Larmor radius *r* smaller than the simulation domain) are subject to a drift motion given by:

$$V_d = (E_{perp} \times B) / B^2$$

Therefore, here the particle drift velocity = V_{dZ} = - 4×10^5 m/s: also affecting equally all RPW stacers. Indeed, previous simulations (not reported here) with a differently oriented *B* generated a drift velocity of electrons, in the -X direction. This resulted in a global motion of particles from RPW2 to RPW3, generating a stronger discrepancy in current balance between antennas, and consequently in final steady potentials. The actual orientation of *B* avoids those issues.

➢ SC potentials

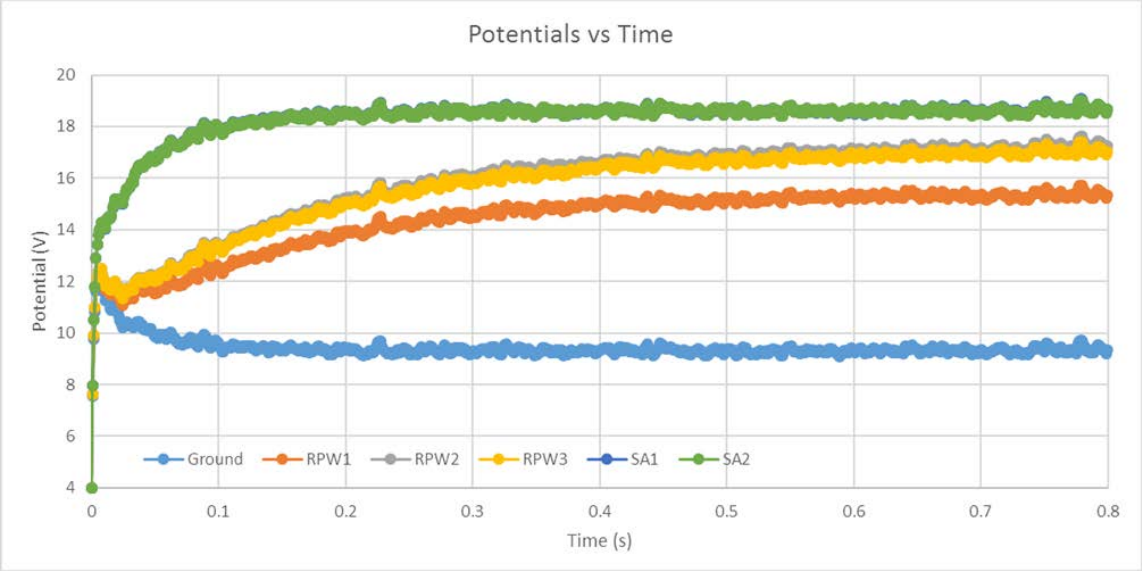

Figure 13 : Case 2 – Time evolution of SC potentials

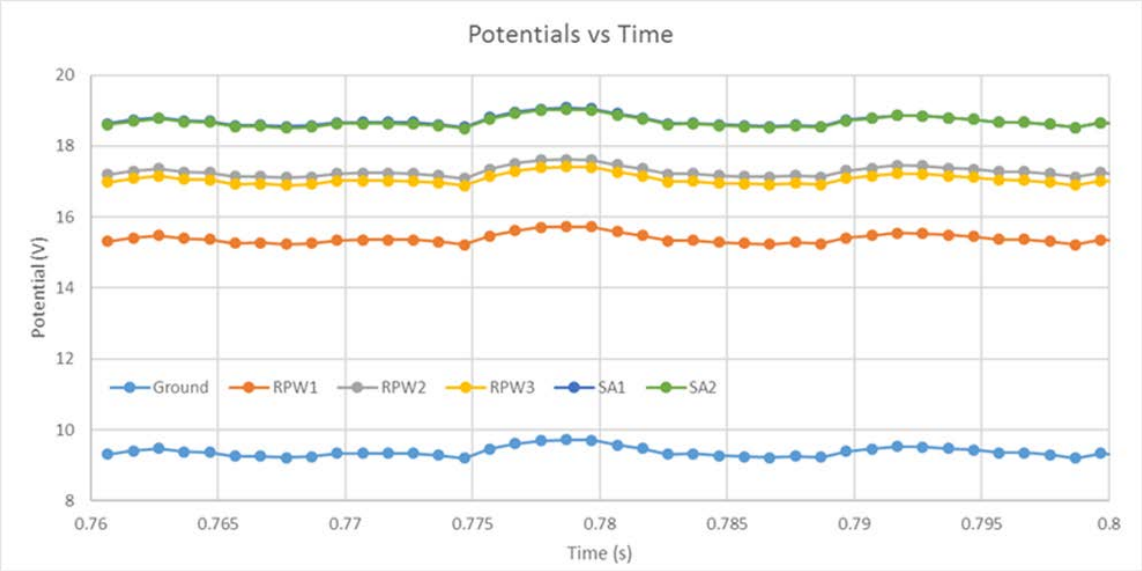

Figure 14 :Case 2 – Focus on time evolution of SC potentials

We estimate that in this Case 2 potential equilibrium is reached after 0.6 s. Average values of potential and corresponding standard deviations are calculated after this time and presented in the next table.

In average *after t = 0.6 s*	Potential (V)	Standard deviation (V)
SC ground	**9.38**	0.11
RPW1 (+Y)	**15.39**	0.11
RPW2 (-X)	**17.28**	0.13
RPW3 (+X)	**17.06**	0.12
SA1(-X)	**18.71**	0.11
SA2(+X)	**18.68**	0.11

Important point. It is firstly remarkable that all SC potentials increased when compared to previous case 1 without *B* (Figure 13 and Figure 14). Indeed, when a induced electric field is applied in the simulation box, potentials given by SPIS (in the live monitoring and in the output text files) suppose that SC potential is referenced to zero. It is theoretically impossible to define a zero which really corresponds to the reference for the entire spacecraft. The only situation that could work would be the case of a small spherical satellite centered in a box which middle is crossed by an isopotential at zero volt, in the moving reference frame of the satellite. This situation is completely inapplicable for the present study.

As for SPIS it is impossible to define a null reference of plasma potential within the satellite reference frame the actual zero is arbitrarily set on the upper point of the spacecraft (according to the +Y oriented electric field in this case).

Therefore, when a strong electric field is applied, it is more relevant to rely on potential differences between SC elements. Which is actually our point of interest when dealing with RPW potentials.

➢ Plasma in volume

Plasma potential for Case 2 is displayed on Figure 15, as the ion density which does not present major difference with the previous Case 1 situation. Ions are not affected by *E* on the scale of this simulation box size, contrarily to secondary particles, as it appears on Figure 16. Secondary and photoelectrons tend to follow drift velocity direction and the force *qE* induced by *V* cross *B* field.

As aforesaid the combined effect of *B* and *E* submit all charged particles to different forces which will affect their motion in the volume. The gyration around *B* (with gyroradius $r=(mv_\perp)/qB$) is calculated as:

Value of *r*	Bz = 8×10^{-7} T
Protons (m)	660
Thermal electrons (m)	14
SEE and photoelectrons (m)	5

➢ Estimation of RPW effective length

As in this case an electric field is applied it is possible to use theoretical reasoning presented in Section 2. Using results extracted from Figure 14, we can plot the time evolution of potential differences between each couple of stacer. The plot is displayed on Figure 17.

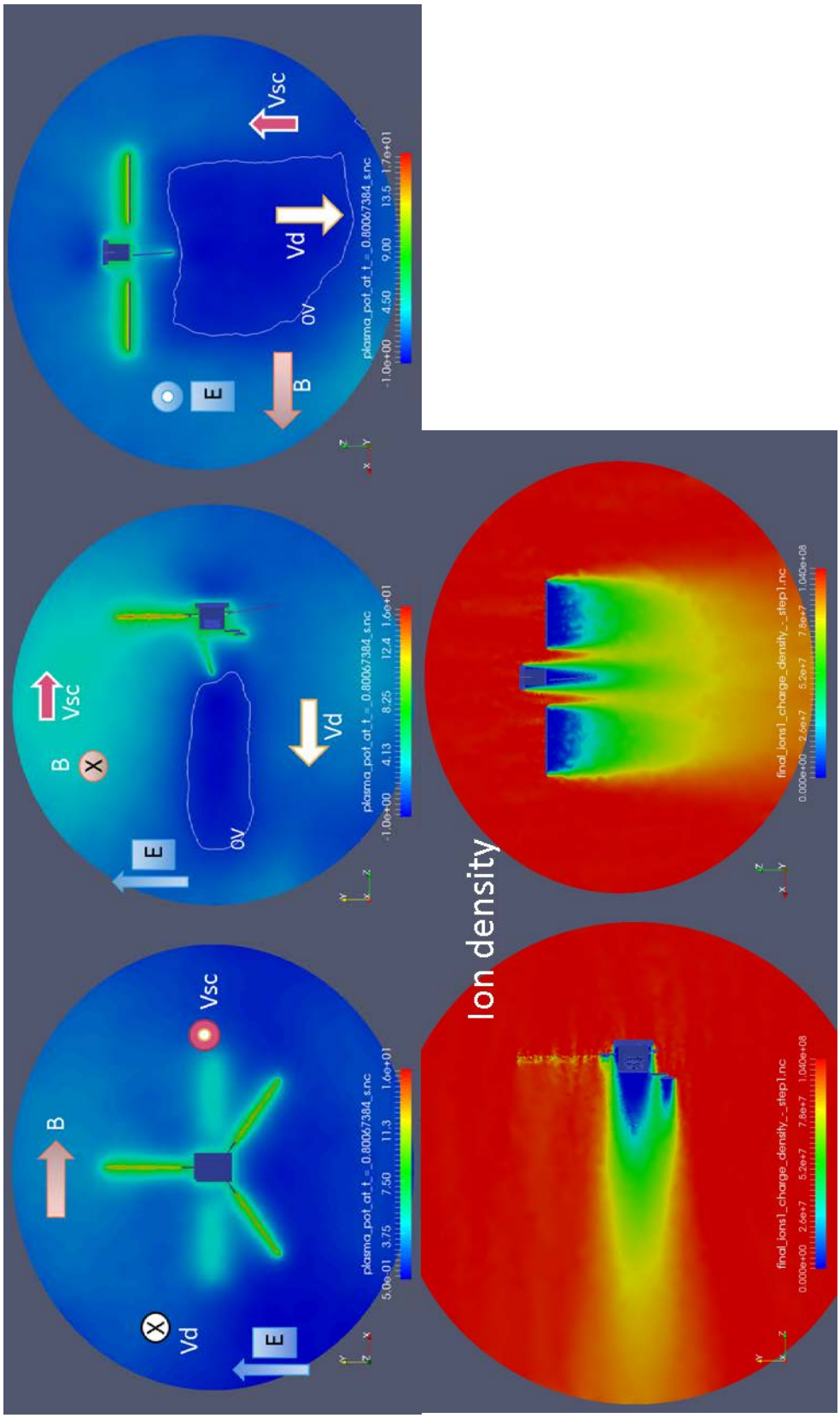

Figure 15 : Case 2 - Plasma potential (on top) and ion density (bottom)

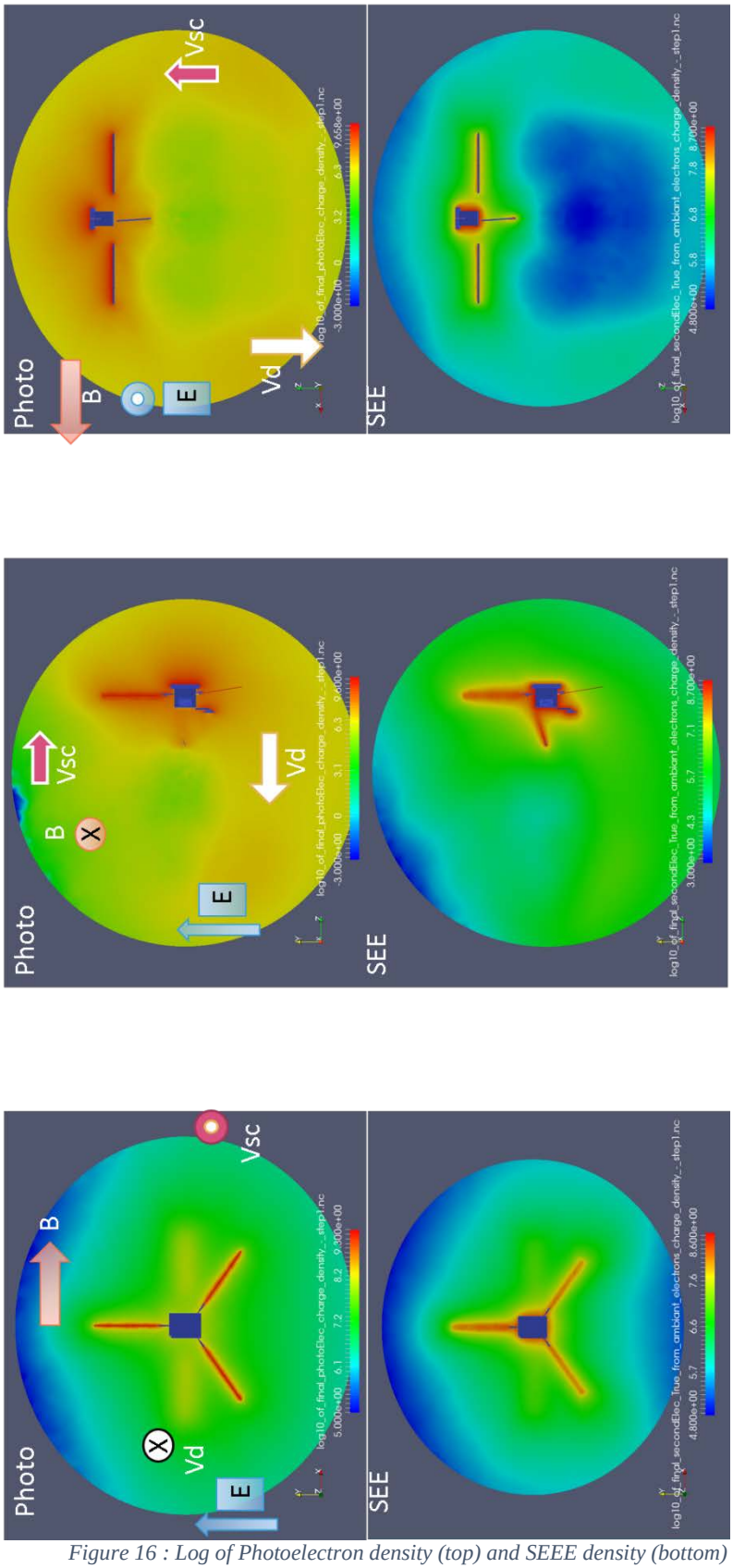

Figure 16 : Log of Photoelectron density (top) and SEEE density (bottom)

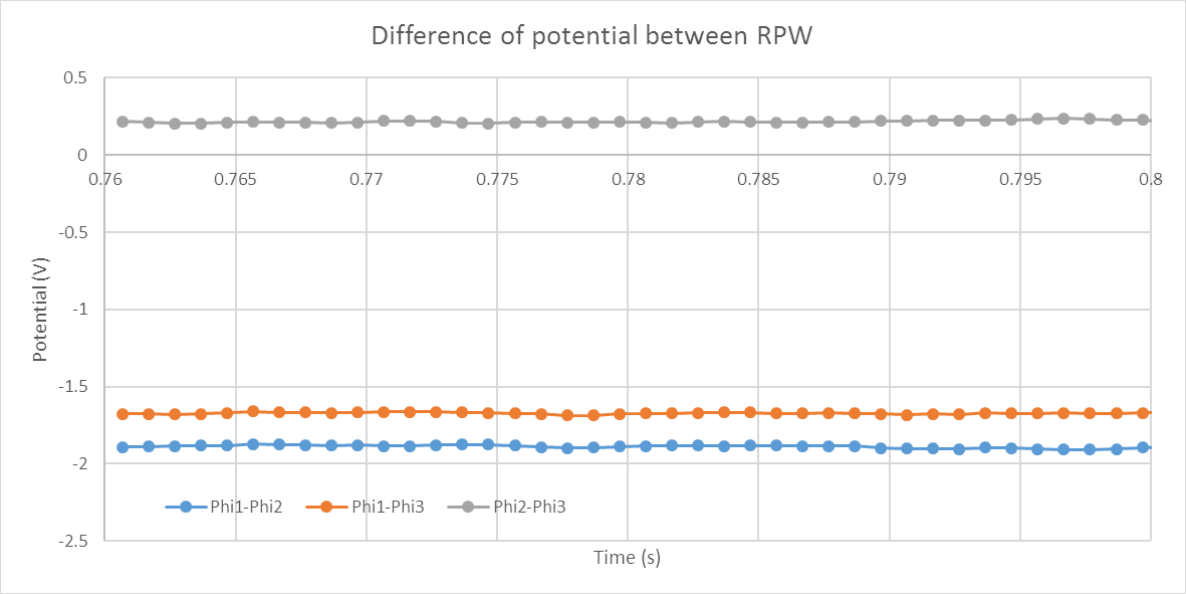

Figure 17 : Case 2 – Time evolution of potential differences between RPW stacers

In average	$\Delta\varphi_{1\text{-}2} = \varphi_1 - \varphi_2$	$\Delta\varphi_{1\text{-}3} = \varphi_1 - \varphi_3$	$\Delta\varphi_{2\text{-}3} = \varphi_2 - \varphi_3$
$\Delta\varphi$ (V)	**-1.89**	**-1.67**	**0.22**
Standard deviation σ of $\Delta\varphi$ (V)	**0.05**	**0.04**	**0.02**

Considering the average values of $\boldsymbol{\Delta\varphi}$ for couples of stacers 1-2 and 1-3, knowing the background E applied on the system $\boldsymbol{E} = E_Y \boldsymbol{e_Y}$ = 0.32 V/m, we have an estimate of the corresponding vertical effective length: $L_{eff} = -\Delta\varphi/E$ which gives $L_{eff(1\text{-}2)}$ = 5.9 m and $L_{eff(1\text{-}3)}$ = 5.2 m.

Those estimates have to be compared to the RPW real configuration (Figure 18).

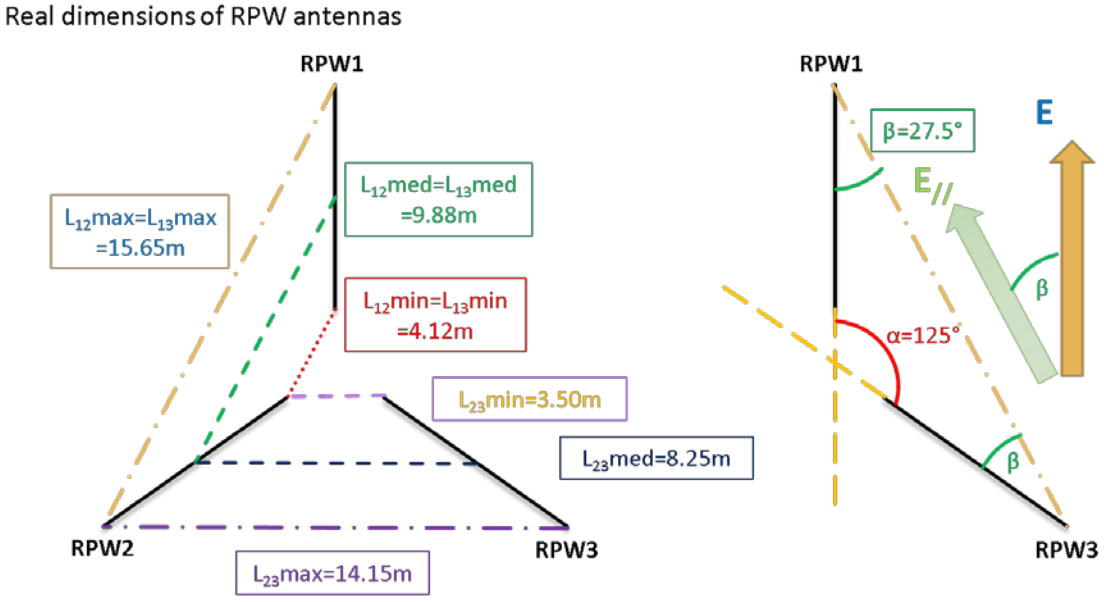

Figure 18 : Main dimensions of the real RPW configuration

The calculated $L_{eff(1-2)}$ and $L_{eff(1-3)}$ have to be renamed $L_{eff(A-B),Y}$ as they refer to the vertical vision of the applied electric field. As E is vertical in this case, we cannot consider $L_{eff(2-3)}$ which is perpendicular to the orientation of electric field. Those effective length values around 5 and 6 m sound disappointing compared to real dimensions between RPW farthest tips. But it has to be reminded that the RPW system is geometrically complex and electrostatically charged and different levels ($\Phi_{preamp} = \Phi_{RPW\text{-}Boom} \neq \Phi_{RPW}$). And this system contains in its center the entire Solar Orbiter body, also charged to a certain potential. Thus the RPW capacity to recover the ambient *E* field is intrinsically slashed by the entire system configuration. Solar Orbiter surrounding electric field is unfortunately not constituted by a pack of perfectly straight lines. They are distorted in the vicinity of the charged structure, which bias the field estimation.

➢ Simple comparison with a "supposedly perfect case"

A quick test concerning 3 conducting spherical probes alone (*i.e.* without SC body at their center) immersed in the same plasma environment that Case 2 allows understanding this distorted field phenomenon. This system configuration is displayed on Figure 19, with real distances between the probes, final potentials reached and *E* field orientation and intensity. With this ideal situation we know the exact orientation of the effective lengths of the system.

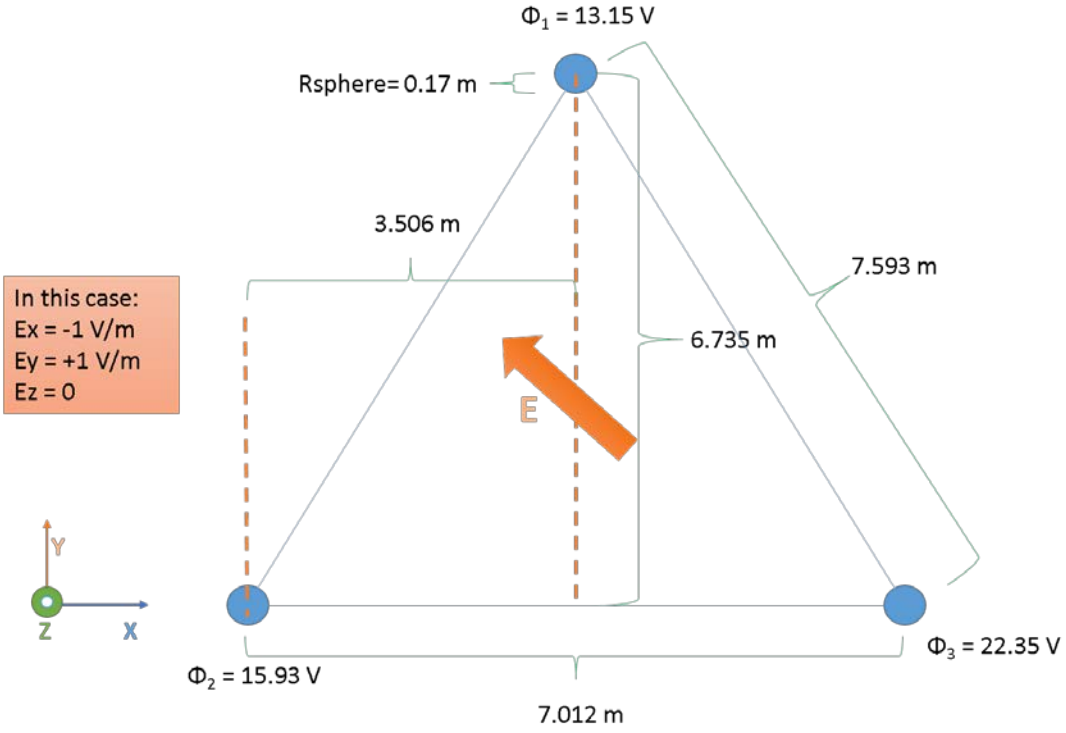

Figure 19 : Presentation of the ideal test, considering only 3 spherical antennas and an oriented E field

Considering an electric field $\vec{E}$ of coordinates (E_x, E_y, E_z), linked to potential *V* in the reference frame (x, y, z) of the RPW system. $\overrightarrow{L_{ij}}$ being the effective length vector of coordinates (L_{ijx}, L_{ijy}, L_{ijz}) in the same basis, with $i \neq j$ and (i, j) = (1, 2, 3).

$$\vec{E} = -\vec{\nabla}V = -\frac{\partial V}{\partial x}\vec{x} - \frac{\partial V}{\partial y}\vec{y} - \frac{\partial V}{\partial z}\vec{z}$$

$$\delta V_{ij} = V_j - V_i = -\vec{E}.\overrightarrow{L_{ij}} = -E_x L_{ijx} - E_y L_{ijy} - E_z L_{ijz}$$

In our case: $L_{ijz} = 0$ whatever *i* and *j* are. Then:

(1) $\delta V_{12} = V2 - V1 = -E_x L_{12x} - E_y L_{12y}$

(2) $\delta V_{13} = V3 - V1 = -E_x L_{13x} - E_y L_{13y}$

(3) $\delta V_{23} = V3 - V2 = -E_x L_{23x} - E_y L_{23y}$

As we have here:
$E_x = -E_y = -1$ V.m^{-1}
$E_z = 0$ V.m^{-1}

And given the configuration of the antennas we assume that:
$L_{12x} = -L_{13x} = L_x$
$L_{12y} = L_{13y} = L_y$
$L_{23y} = 0$

Simulation results give, on average:
$\delta V_{12} = 2.78$ V
$\delta V_{13} = 9.20$ V
$\delta V_{23} = 6.42$ V

Using previous equations, we obtain:
(1) + (2) → $-2L_y = 11.98$ → $L_y \sim -6$ m
(1) - (2) → $2L_x = -6.42$ → $L_x \sim -3.2$ m
(3) → $L_{23x} \sim 6.4$ m

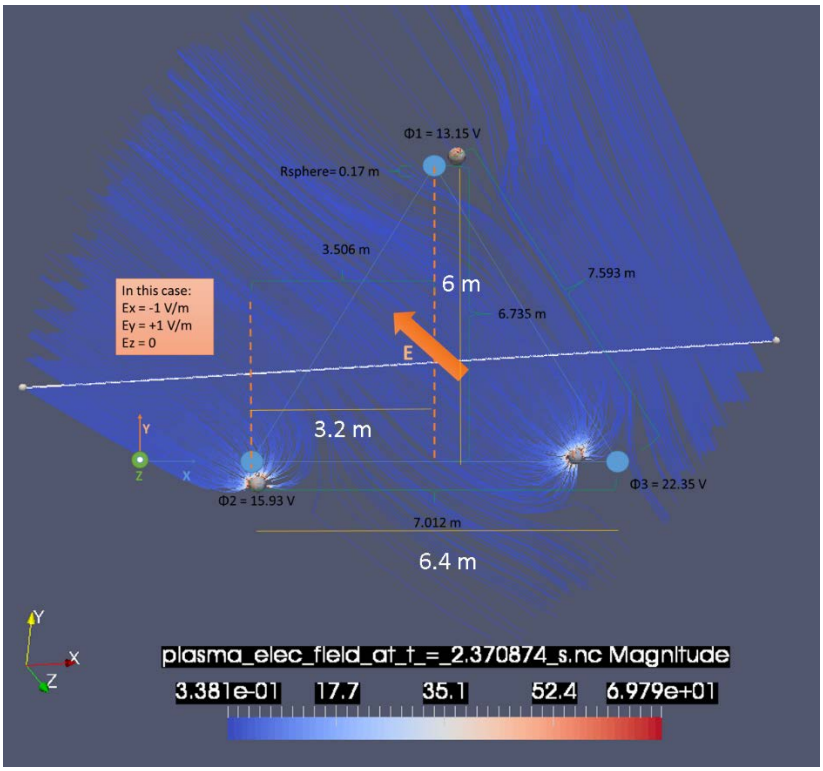

Figure 20 : Illustration of distorted E field in the vicinity of charged antennas. Electric field lines (blue) plotted are the ones passing by the arbitrary white line (in the plane containing all sphere centers).

Calculated $L_{eff1\text{-}2}$ and $L_{eff1\text{-}3}$ thus equals 6.8m. Compared to real distances between spheres, displayed on previous Figure 19, effective lengths lose 0.5 m on average. Figure 20 clearly illustrates this phenomenon. We choose arbitrarily a line (the white one on the Figure), contained in the plane of the probes, and plot all electric field lines (in blue) passing by this element. Those field lines are visibly deviated in the vicinity of the probes and generate this loss of determination accuracy on real electric field value. In the case of SolO + RPW system, the situation becomes obviously more complex and disturbed, especially with the charged SC body in the middle, which explains the important discrepancy between true spaces separating RPW tips and determined L_{eff}.

So we can predicate that own PRW elements non null potentials are disabilities in *E* estimations. That emphasizes the interest of injecting biasing currents into stacers in order to lower down this charging and spare electric field lines distortions in the vicinity of the wires.

4.3. Cases 3: parametric study with various *E* intensities

We base a series of simulations on previous Case 2 environment, making *B* (and thus the induced *E* intensity) values vary. Electric field orientation remains vertical. The focus is carried on final potential obtained on the SC elements and the corresponding effective lengths calculated.

Case	B (T)	E (V/m)	Ground (V)	RPW1 (V)	RPW2 (V)	RPW3 (V)	Phi1-2 (V)	Phi1-3 (V)	Phi2-3 (V)
Case A	0	**0**	4.48	10.39	10.74	10.54	**-0.35**	**-0.15**	**0.2**
Case B	8.00E-07	**0.32**	9.38	15.39	17.28	17.06	**-1.89**	**-1.67**	**0.22**

Case D	2.50E-06	**1**	17.79	23.39	28.29	28.09	**-4.90**	**-4.70**	**0.20**
Case C	4.00E-06	**1.6**	25.15	30.73	38.91	38.67	**-8.18**	**-7.94**	**0.24**

Starting from $E = -\Delta\varphi / L_{eff}$ it gives $\Delta\varphi = -L_{eff}.E$, with L_{eff} being the slope of the plot (see the next Figure 21). For each couple of stacers, the slope of the corresponding plot provides the vertical estimated effective length. RPW1-2 and RPW1-3 seem to represent lengths of 4.8 m.

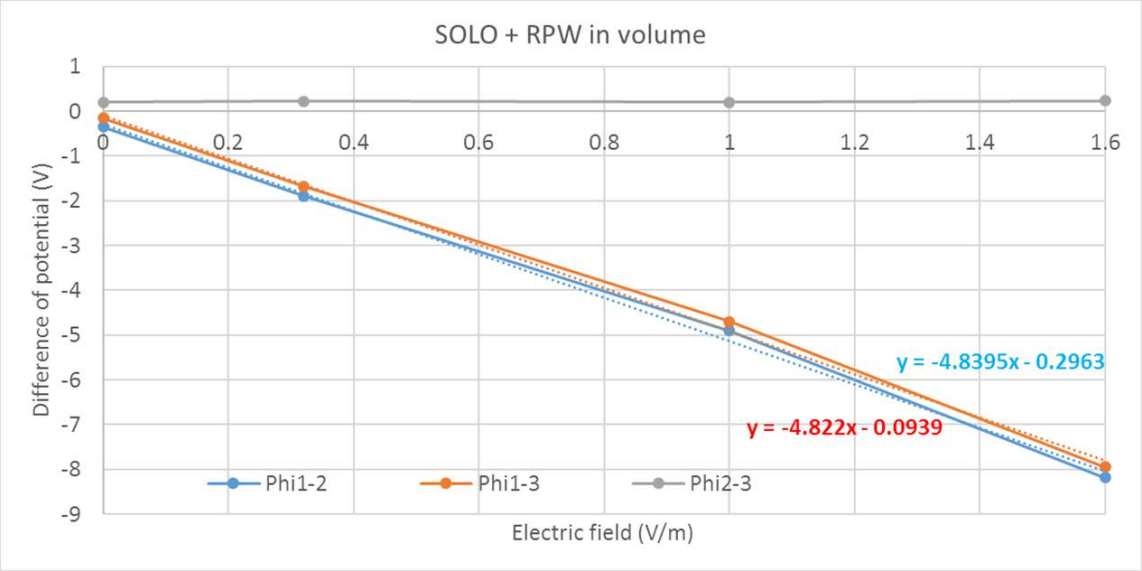

Figure 21 : Plot of $\Delta\varphi$ as a function of applied vertical Electric field for Solar Orbiter. Slope of the plot gives the estimated effective lengths of RPW system

In order to illustrate previous point broached in Section 4.2.4, we also performed a parametric study as the one summarized in Figure 21, but without Solar Orbiter body at the middle of RPW system. We thus only had the three antennas (including their shields, booms and preamps) in the simulation box. The next Figure 22 corresponds to Figure 21 but for this filtered geometry, it sums up difference of potentials obtained for the couples of stacers and the corresponding slopes providing the estimated effective lengths.

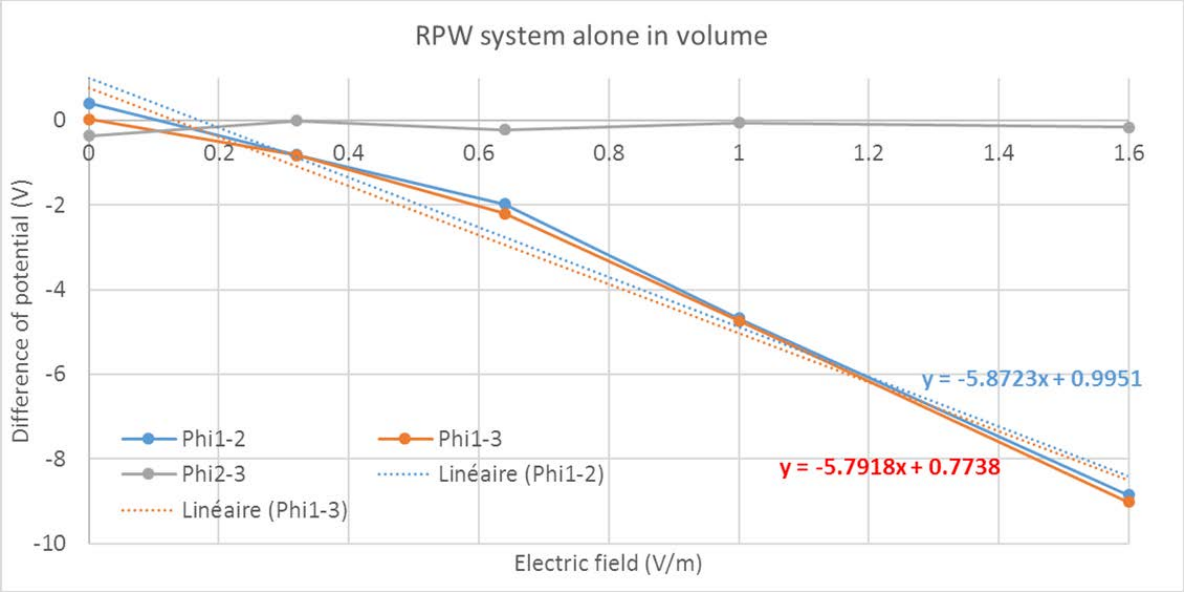

Figure 22 : Plot of $\Delta\varphi$ as a function of applied vertical Electric field for RPW without Solar Orbiter body. Slope of the plot gives the estimated effective lengths of the filtered RPW system

We can notice that as supposed, the absence of SC body enhanced the RPW effective lengths of 1 m on average (4.8 m → 5.8 m). Unfortunately, this ideal situation is unenforceable in reality.

4.4. Conclusion on simulations with older SolO configuration

This above series of simulations with now outdated Solar Orbiter and RPW configurations allowed to estimate the global behavior of the system within the perihelion environment. It emphasizes the strong secondary emission of spacecraft surfaces (photoelectrons + SEEE + SEEP) due to hot and dense environment. All satellite surrounding will be immersed in a secondary particle cloud, around any scientific instrument including RPW experiment. The ion wake will also be problematic as it will completely embrace the rear boom (which carries several instruments such as SWA-EAS detector).

First estimations concerning RPW effective lengths give values around 4.8 m which three times below real distances between stacer tips. This is partly due to proper wire potentials, indicating that biasing currents injected in the stacers to lower down their potentials will help enhancing their electric field determination abilities. Low effective length is also due to the presence of the charged SC body in the center of this system, including solar arrays dielectric faces more charged than the rest and disturbing the electrostatic pattern. Rotated arrays might help curbing this issue.

In the next Section we will present the new Solar Orbiter CAD model, more relevant with recent design updates concerning geometry and materials. New functionalities concerning injected biasing currents into the RPW antennas will also be applied and analyzed.

5. Study of Solar Arrays impacts on RPW effective lengths

5.1. Context

In this study we evaluate impacts of solar arrays configuration on RPW experiment, checking effects of their presence and rear covering materials on antennas effective lengths. Indeed, at this time some interrogations remain on the eventual presence of dielectric patches on solar panel shadowed faces. Unfortunately, having dielectric materials in the shadow usually leads to negative potentials on them, at levels which depend on material properties and ambient thermal electron properties. In such perihelion

environment, strong negative potentials are expected, with disturbing electrostatic patterns in the vicinity of RPW planes.

3 simulations are thus performed:

- First one without any solar panel – named “noSA”,
- Second with solar panels: sunlit face covered with dielectric CERS, sides and shadowed face with conductive CFRP – named “SAcond”
- Last simulation based on the second one but with solar arrays rear faces covered with dielectric Epoxy – named “SAdiel”.

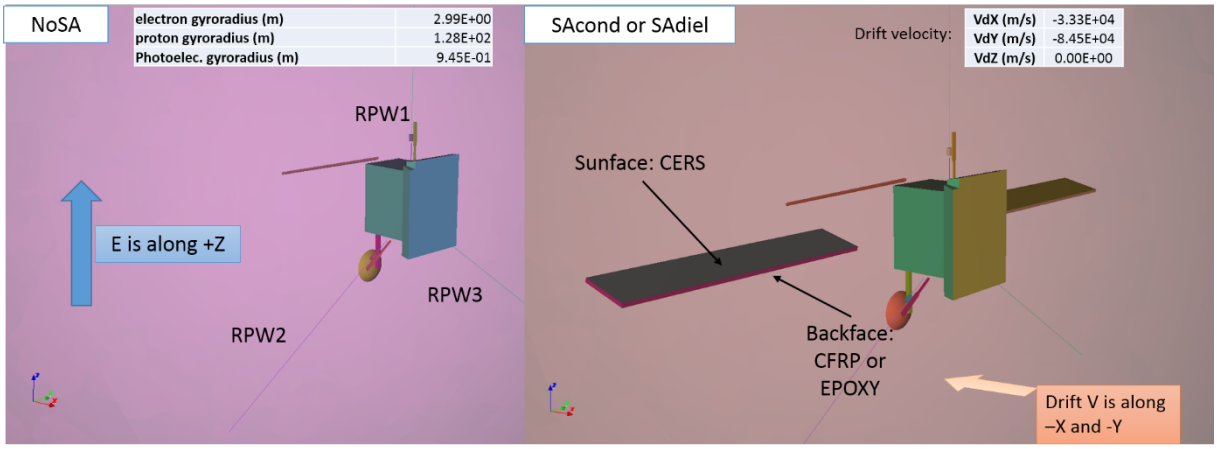

Figure 23: Global configuation of SolO and environment for this study

Figure 23 illustrates those configurations. All simulations consider Solar Orbiter at 0.28 AU from the Sun, *i.e.* the same environment described in previous Section 3.5. One slight difference is that for this study we consider thermal electrons with characteristic temperature of 30 eV, in order to approach the temperature of primary electrons which for Epoxy generate the most numerous secondary electrons, and this way estimate the most extreme charging situation for Epoxy dielectric material.

As explained in previous Section 3.5, with SPIS it is not possible to generate an electric field directly over the plasma volume. The spacecraft is considered as motionless and the plasma is moving through the simulation box (with thermal and/or bulk velocities set by user). To create E we impose a uniform magnetic field and a velocity to the spacecraft and set V_{plasma} = 0. The $E=V\times B$ electric field generated over the simulation box is constant and uniform. In those cases, we consider the following parameters:

Vx (m/s)	4.00E+05	**Bx (T)**	-4.06E-06	**Ex (V/m)**	0.00E+00	**Norm B (T)**	4.3639E-06
Vy (m/s)	-6.00E+04	**By (T)**	1.60E-06	**Ey (V/m)**	0.00E+00	**Norm (V/m)**	0.3964
Vz (m/s)	0.00E+00	**Bz (T)**	0.00E+00	**Ez (V/m)**	3.96E-01		

It can be noticed that the electric field obtained here (~0.4 V/m along +Z direction) is too strong compared with expected values at this heliocentric distance. This choice was made for this study to clearly see effective lengths modifications due to various solar arrays configurations. However, the strong B value generates an important particle drift velocity along X (-3.3 × 10^4 m/s) and Y (-8.4 × 10^4 m/s) axis, which will increase discrepancy between potentials on RPW2 and 3.

Estimated gyroradii are for this environment: 3 m for ambient electrons, 128 m for protons and 1 m for secondary and photoelectrons.

5.2. Geometry updates

Few changes have been operated on the previously used CAD model. First, it is now correctly oriented with respect to the official reference frame of Solar Orbiter: X axis points the Sun (normal to SC heatshield), Y axis perpendicular to X (aligned with solar arrays rotation axis), and Z parallel to the upper RPW antenna (RPW1).

Main evolutions for this study are the measurements made by ONERA (Toulouse) on Elgiloy and Niobium materials. Indeed, those substances will cover respectively the RPW stacers and shields, but weren't available in the SPIS material library. Their main properties (necessary for SPIS) have been partially determined and allowed the generation of those two new materials for the software material catalogue (new files "ELGI" and "NIOB"), and the update of RPW CAD model with relevant configuration of the structure. One key point is the changing between the old outdated gold covering layer on the stacers and the actual Elgiloy used element: the latest is 10 times less photo-emissive than gold. The main consequence of this modification should be the decrease of steady potentials on stacers (without considering any biasing current). However, some measurements concerning photoemission remain incomplete and require updates (to be performed by ONERA but still missing at this time). Other materials on SolO are unchanged.

Rotation of solar panels has also been implemented, with the previously detailed SAA angle depending on the heliocentric distance of the satellite (in our case at perihelion this angle - SAA - equals 76.5°). This new configuration might influence this electrostatic pattern in a region near RPW detection plane.

5.3. First and second case results: noSA and SAcond

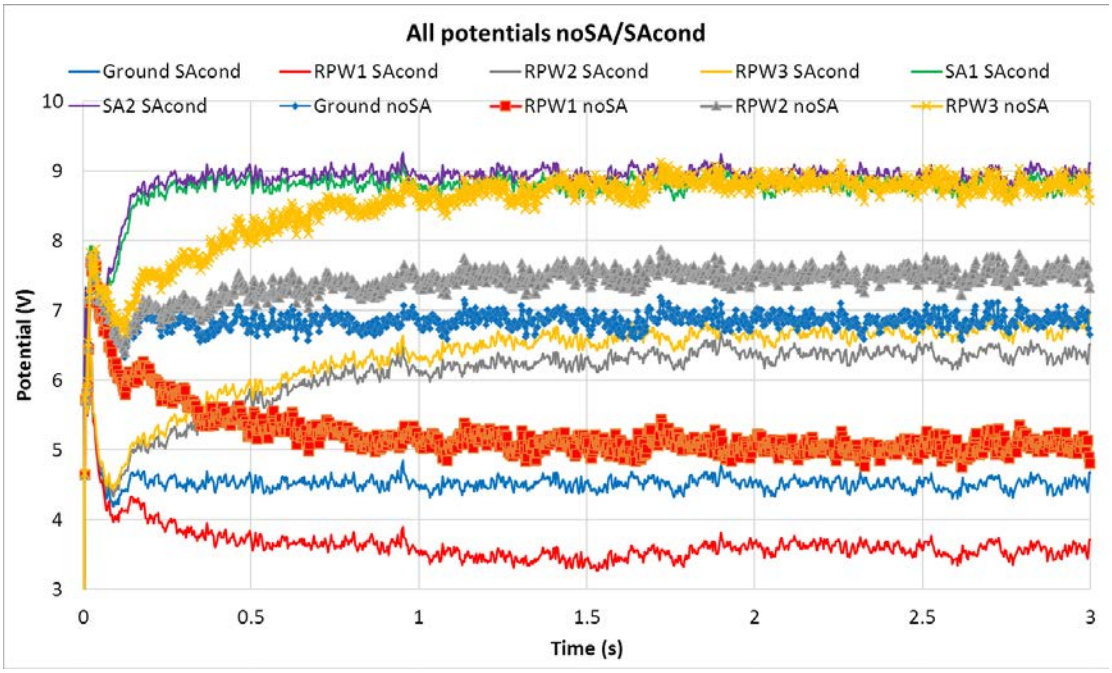

Figure 24 : Cases noSA and SAcond - Time evolution of SC potentials

This unrealistic first case without solar generators is considered as the reference regarding the two other simulations of this solar arrays study. We first compare cases without dielectrics in shadow because of the timescales: when non conducting materials are not in sunlight it takes at least ~ 250 seconds in our case for them to reach steady equilibrium potentials (and few days of simulation) while conducting ones are steady after 1 or 2 seconds. Figure 24 presents satellite potentials for noSA and SAcond.

It can be noticed on this Figure that the connection of solar arrays with sunlit dielectric faces to the spacecraft body globally decreased electrostatic potentials on conducting surfaces. The balance of currents between all SC elements being modified by higher positive potentials on those new surfaces, conducting surfaces weakened their potentials with respect to infinite. SC ground weakened from 6.86 to 4.50 V and antennas from a range of 8.81-5.04 V to 6.69-3.58 V. Solar array front faces are charged at 8.8-8.9 V on average.

Potential discrepancy between RPW2 and 3 (theoretically zero because of vertical electric field, but existing here due to drift velocity) is reduced by the presence of solar arrays. It reduces from 1.28 V for noSA to 0.32 V for SAcond. Indeed, the panels generate similar clouds of secondary particles close to those antennas and similar local electrostatic patterns which reduce asymmetry between collected currents on stacers. Discrepancies between RPW1 and 2, or 1 and 3, practically doesn't change when adding those solar arrays, as it appears more clearly on Figure 25.

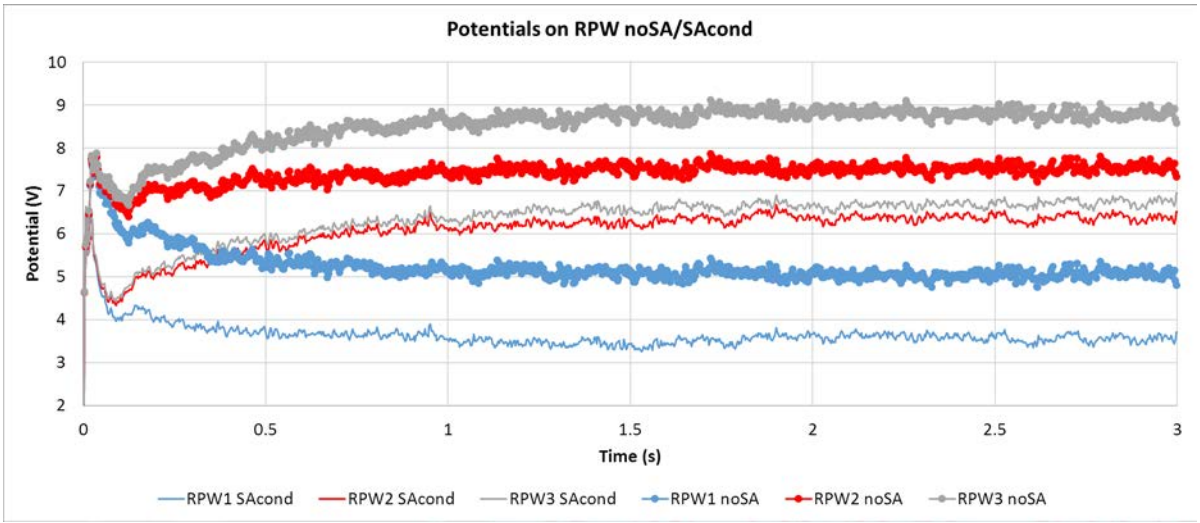

Figure 25 : Cases noSA and SAcond - Time evolution of RPW antennas

5.4. Third case results: SAdiel and comparison with previous cases

This case including dielectric material (Epoxy) on shadowed faces of solar panels took much more time to reach equilibrium (250 seconds). Because of very long timescale: simulation time steps had to be strongly increased to reach « quasi » equilibrium in a reasonable time… unfortunately it also increased potential fluctuations on SC elements, as it appears on Figure 26. We also notice, and this is quite important and *a priori* worrying, that epoxy elements here reach -120 V.

Including Epoxy faces on the backsides of solar generators reduced even more satellite potentials on conducting elements. Those high negatively charged elements repel very efficiently secondary electrons outside the simulation box, so they have less chances to be recollected by positive front faces of panels (which thus becomes even more positive regarding previous case SAcond). Correspondingly, other SC potentials decreased a little bit more, but numerical estimation of this decrease has become difficult and deceptive because of strong potential fluctuations, inherent to this last case setting. This appears obviously on Figure 27, with a focus on RPW potentials.

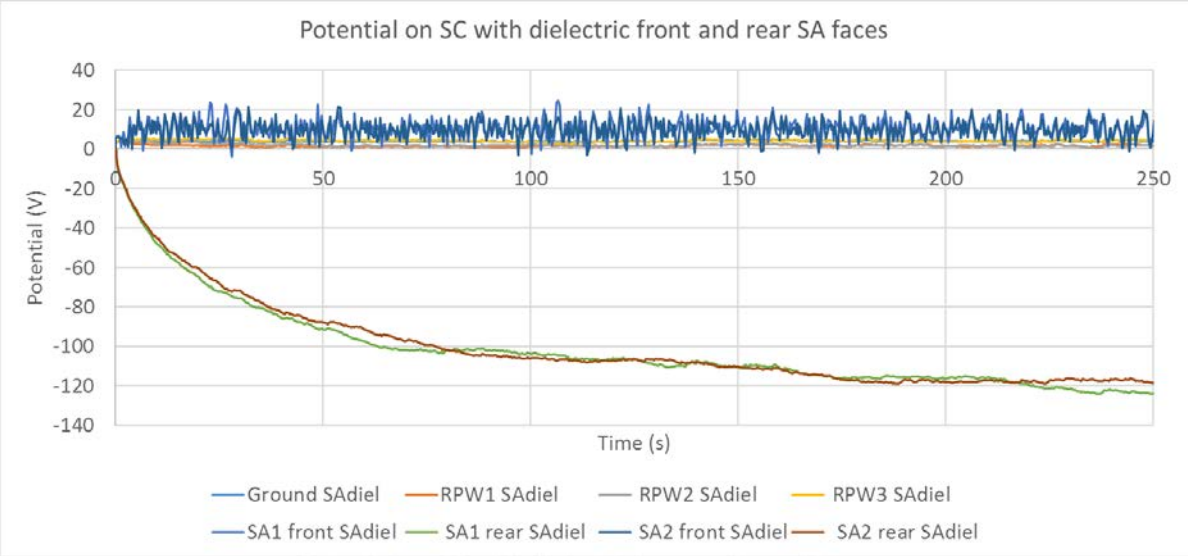

Figure 26 ; Case SAdiel - Time evolution of SC potentials

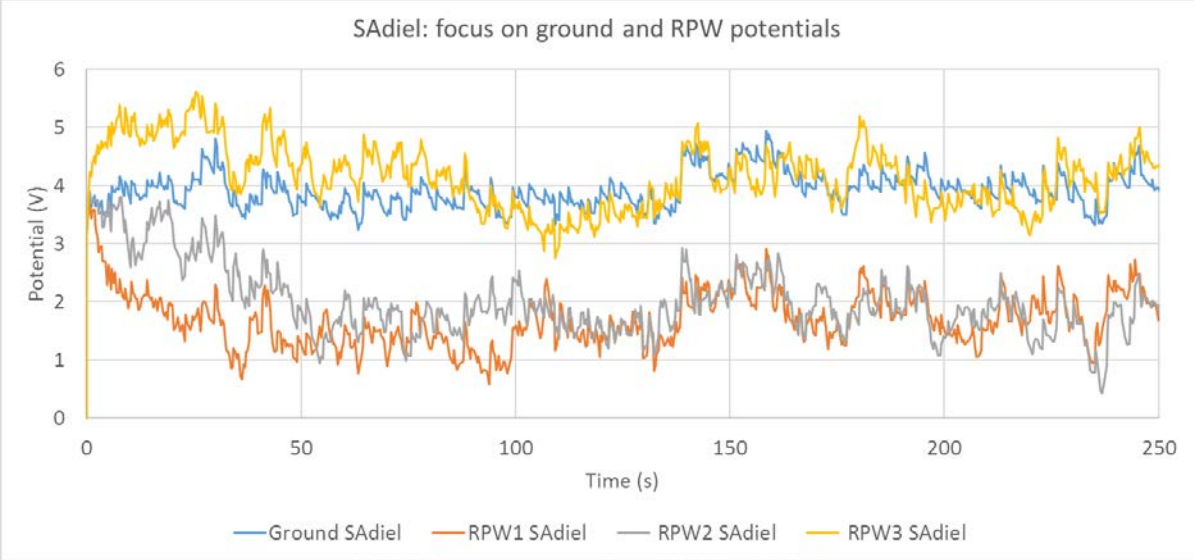

Figure 27 : Case SAdiel - Time evolution of SC ground and RPW potentials

	Ground (V)	RPW1 (V)	RPW2 (V)	RPW3 (V)	SA1 front (V)	SA2 front (V)	SA1 rear (V)	SA2 rear (V)	dP1-2 (V)	dP1-3 (V)	dP2-3 (V)	Diff # noSA dP1-2 (%)	Diff # noSA dP1-3 (%)	Diff # noSA dP2-3 (%)
noSA Φ	6.86	5.04	7.53	8.81	NA	NA	NA	NA	-2.49	-3.76	-1.28	NA	NA	NA
noSA σ	*0.10*	*0.10*	*0.10*	*0.10*	*NA*	*NA*	*NA*	*NA*	*0.03*	*0.06*	*0.04*			
SA cond Φ	4.50	3.58	6.37	6.69	8.80	8.93	4.50	4.50	-2.79	-3.11	-0.32	12	17	75
SA cond σ	*0.08*	*0.08*	*0.08*	*0.09*	*0.08*	*0.08*	*NA*	*NA*	*0.04*	*0.07*	*0.04*			
SA diel Φ	3.94	1.69	1.82	4.01	10.62	9.73	-123.25	-117.33	-0.13	-2.33	-2.20	95	39	72
SA diel σ	*0.31*	*0.43*	*0.39*	*0.46*	*4.48*	*4.43*	*0.47*	*0.71*	*0.40*	*0.48*	*0.47*			

Figure 28 : Study on SA impacts on RPW – overview of numerical values obtained for all cases. dP stands for difference of potential between RPW stacers, Φ for potentials and σ for the standard deviation

Table on Figure 28 summarise numerical values of potentials and standard deviations extracted from those three simulations. Those values are averaged over late stable potential period for each case. One important remark that can be made in addition to previous comments, is that dielectric surfaces in shadow for SAdiel strongly disturbed potentials on stacers, especially on the potential discrepancy between RPW2 and 3, leading to an eventual misinterpretation of corresponding measured electric fields. The explanation is a subtle combination of various phenomena, and will be detailed in the following.

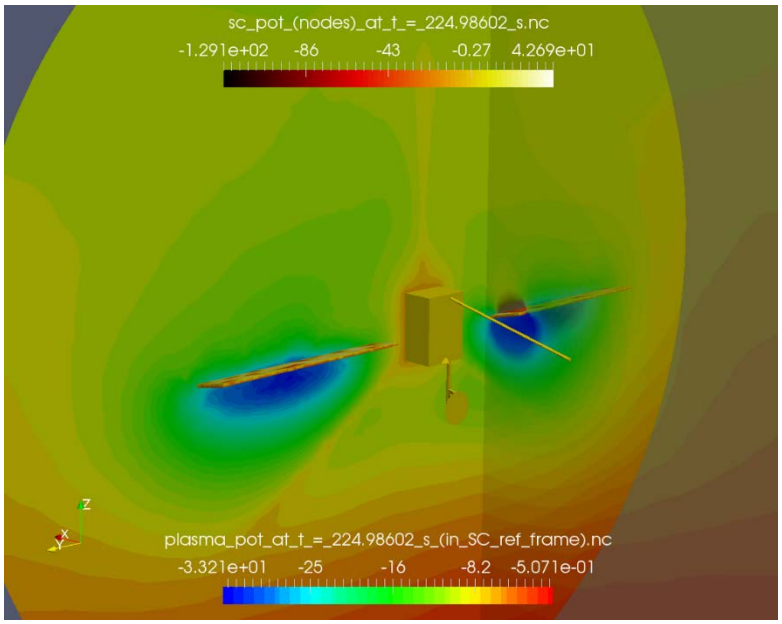

Figure 29 : SAdiel – plasma potential in the Y-Z plane (containing the RPW antennas) and the X-Z plane near SA1

First, dielectrics in shadows on rear solar array faces charge to strong negative potentials (~ -120 V). These two potential wells expand in space as volumes of negative electrostatic potentials, similar to "bubble regions", which sizes depend on surface charging levels and local space charge density (Debye length). This is illustrated on Figure 29, where the plasma potential in the *Y-Z* plane (containing the RPW antennas) and the *X-Z* plane near SA1 is displayed. It clearly shows the expansion of negative potential regions up to the RPW plane due to solar arrays shadowed dielectric faces. Next Figure 30 compares plasma and SolO potentials in the *Y-Z* plane containing RPW antennas for all cases, showing the SA influence on electrostatic pattern around RPW stacers.

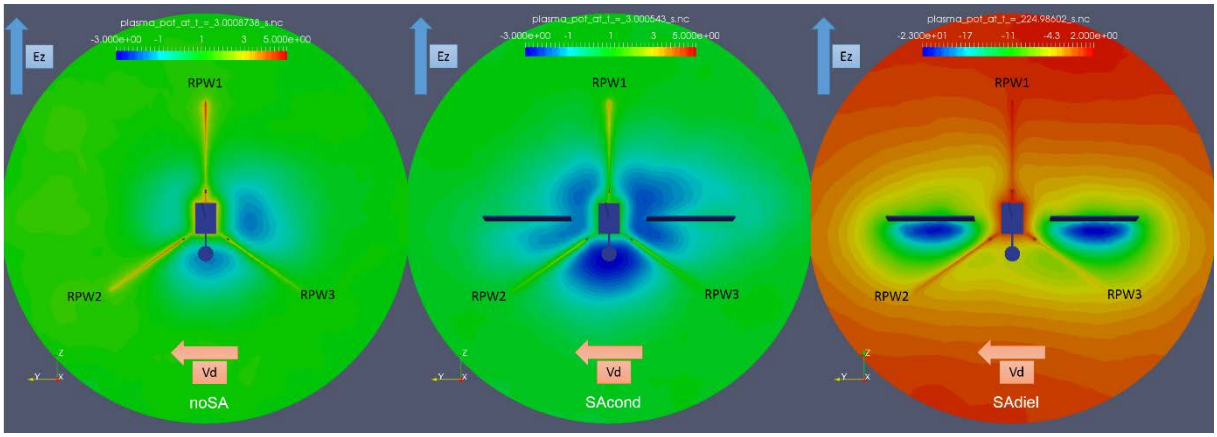

Figure 30 : Plasma and SolO potentials in the Y-Z plane containing RPW stacers for cases noSA (left), SAcond (center) and SAdiel (right). Here looking towards +X direction, i.e. showing the rear side of SolO.

Then, according to heliocentric distance of the satellite at 0.28 AU: solar panels are oriented at 76.5° around their rotation axis (*Y*), meaning that those negatively charged Epoxy areas are facing mostly downwards and a little bit behind the satellite (in the -*Z* and -*X* direction). This means practically towards RPW stacers 2 and 3, even though they are not directly pointed by Epoxy faces (also visible on Figure 29 and Figure 30).

Third, faces at -120 V and corresponding negative bubble regions efficiently repel low energy particles (secondary and photoelectrons). Those electrons are pushed outwards, around the negative potential bubbles which also includes the vicinity of bottom RPW antennas (2 and 3). This phenomenon is showed on Figure 31, which illustrates the secondary electron density on the RPW plane, and those two negative electrostatic potential regions (from -130 to -5 V) represented as 3D meshed volumes.

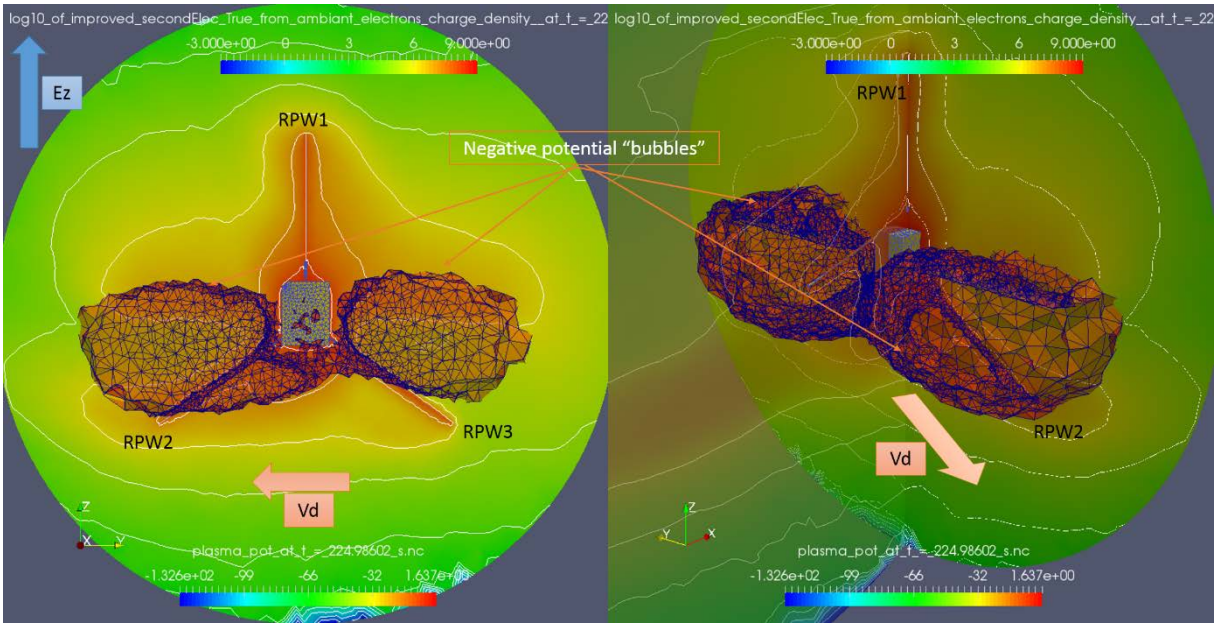

Figure 31 : SAdiel – Log10 of SEE density in the X-Z plane and corresponding iso-contours. 3D meshed volumes around SA corresponds to regions where plasma potential is below -5 V, and thus repel SEE from those zones. The red arrow identified as "Vd" stands for the drift velocity vector orientation, which pushes particles towards (-X, -Y) direction.

The next point is that as bottom stacers are positively charged, they will easily collect those forced out electrons, and consequently have their potential lowered down (as it is indicated on the table of Figure 28, when looking to potential values of RPW 2 and 3 between cases SAcond and SAdiel.

Finally, the drift velocity effect linked to ($E \times B$) pushes particles towards the -Y and -X direction, *i.e.* from RPW3 to RPW2. Electrons emitted by RPW3 will tend to flow towards RPW2, being thus less collected by their source (Φ_{RPW3} will remain positive) but more attracted by the other stacer (Φ_{RPW2} will thus decrease). This SEE density shift also appears on Figure 31. Consequently: $\Phi_{RPW2} = 1.82$ V < $\Phi_{RPW3} = 4.01$ V. This has to be compared to the previous case without dielectric faces in shadow.

Indeed, in the SAcond case all spacecraft surfaces were positively charged and we had no such repelling volumes around the structure. Secondary and photoelectrons thus remained in the close vicinity of all positive surfaces, mainly influenced by those local dominant electrostatic forces. In such situation: practically no discrepancy between SAcond stacers: $\Phi_{RPW2} = 6.37$ V ~ $\Phi_{RPW3} = 6.69$ V. However, for SAdiel, once repelled a bit farther from the satellite, electrons undergo the locally prevailing drift velocity and flow more efficiently towards the -Y side of the simulation box, generating the discrepancy between RPW3 and RPW2. The overview of those above-mentioned effects is presented on Figure 32, comparing the secondary electron density in the RPW plane for noSA, SAcond and SAdiel cases. On this Figure we notice the lack of secondary electrons around lower stacers in SAdiel (and photoelectrons behave in the same way) which extends the local Debye length and consequently the local potential effects. A diagram displaying all average potentials values obtained on various SC elements for all simulations of this Solar Array study is presented on Figure 33.

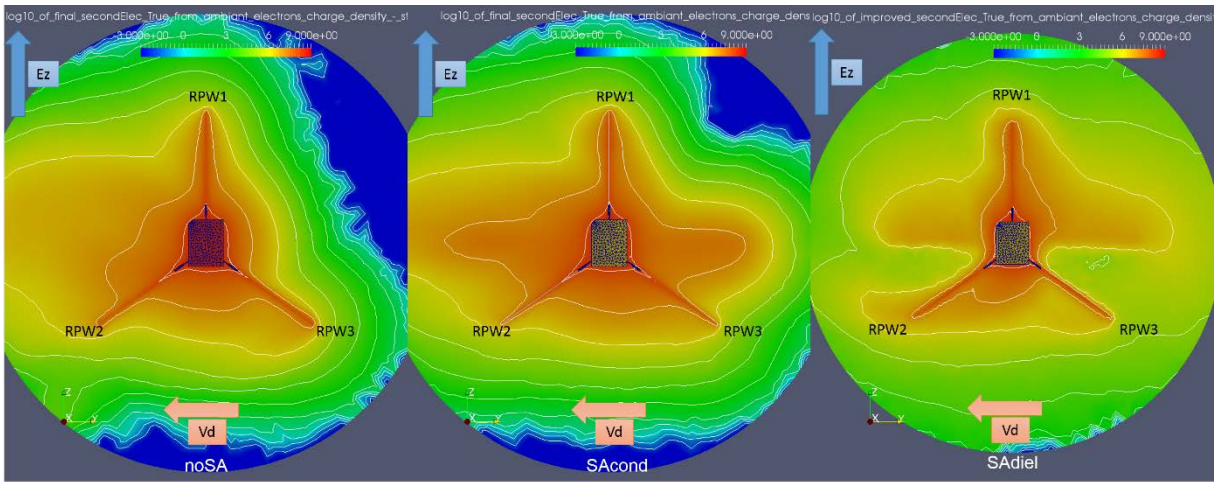

Figure 32 : Log10 of SEE density in the Y-Z plane containing RPW stacers for cases noSA (left), SAcond (center) and SAdiel (right). Here looking towards -X direction, i.e. showing the front side of SolO. Drift velocity Y component effect appears on those pictures with the visible shift of particle density from the +X side to -X side.

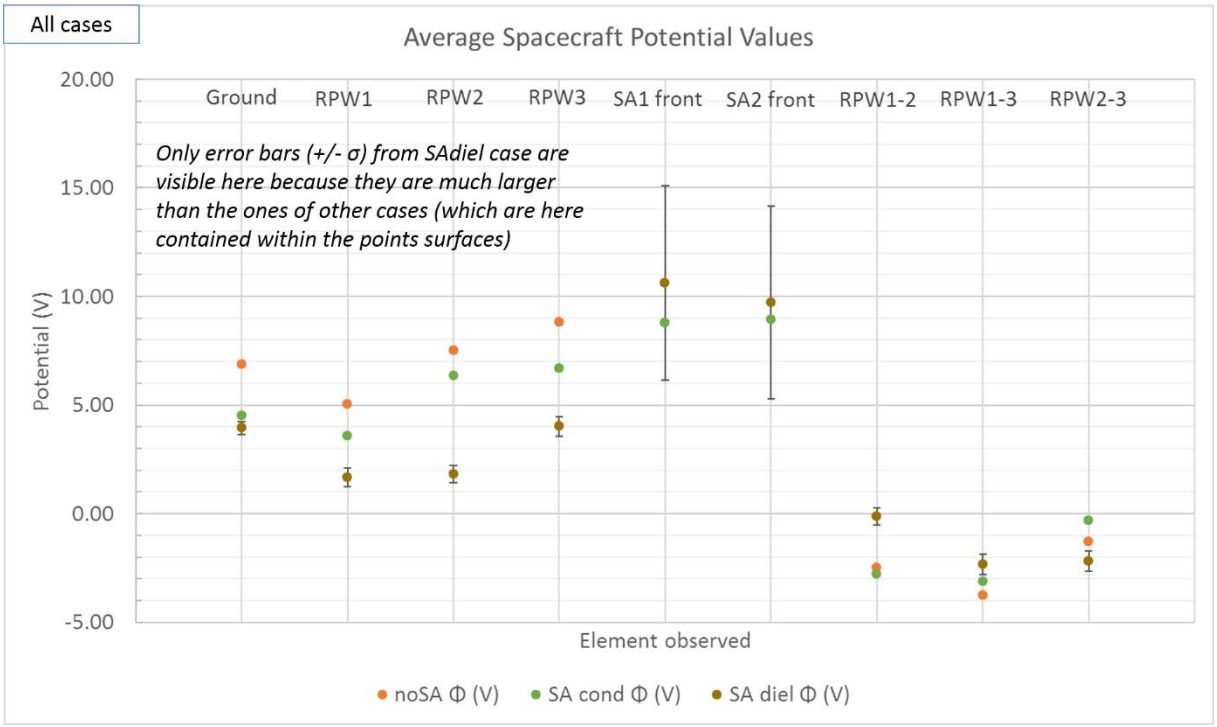

Figure 33: Diagram of average potentials values obtained on various SC elements for all simulations of this Solar Array study.

Now, it is needed to estimate those various physical effects, linked to the different SA configurations, on RPW effective lengths. However, accurate determination of uncertainty on effective length estimations need consideration of the fact that potential values on stacers have been averaged over certain time periods. Methodology of uncertainty on L_{eff} calculation is presented below.

L_{ij} being the effective length between RPW i and j, we have $E = -\partial\Phi_{ij} / L_{ij}$ so we can set:

$$\Delta E/E = \Delta(\partial\Phi_{ij}) / \partial\Phi_{ij} + \Delta L_{ij} / L_{ij}$$

with ΔX the uncertainty on X parameter: $\Delta X = +/- xx$ [unit].

We assume $\Delta E = 0$ considering that SPIS applies the exact electric field chosen by user.
So, with $\Delta(\partial\Phi_{ij}) / \partial\Phi_{ij} = (\Delta\Phi i + \Delta\Phi j) / (\Phi i - \Phi j)$, we finally have:

$\Delta L_{ij} = L_{ij} ((\Delta\Phi i + \Delta\Phi j) / (\Phi i - \Phi j))$ which is the uncertainty on the effective length.

It is thus possible to extend the previous table on Figure 28 with effective lengths determination for each simulation, and corresponding uncertainty on L_{eff}. Results are presented on the next Figure 34.

	dP1-2 (V)	dP1-3 (V)	dP2-3 (V)	Diff # noSA dP1-2 (%)	Diff # noSA dP1-3 (%)	Diff # noSA dP2-3 (%)	Leff1-2 (m)	Leff1-3 (m)	Leff2-3 (m)	ΔLeff1-2 (m)	ΔLeff1-3 (m)	ΔLeff2-3 (m)
noSA Φ	-2.49	-3.76	-1.28	NA	NA	NA	6.28	9.51	3.23	0.50	0.50	0.50
SA cond Φ	-2.79	-3.11	-0.32	12	17	75	7.05	7.86	0.82	0.40	0.43	0.43
SA diel Φ	-0.13	-2.33	-2.20	95	39	72	0.33	5.88	5.55	2.08	2.25	2.14

Figure 34 : Study on SA impacts on RPW – extension of previous table (Fig. 28). Overview of numerical values obtained for all cases. dP stands for difference of potential between RPW stacers, Φ for potentials, Leff for calculated effective lengths for each couple of stacers and ΔLeff for the corresponding uncertainty, computed thanks to the previous formula.

It appears on the previous table that solar arrays having both sides covered with non-conducting materials completely annihilated RPW capacity to provide ambient electric field determination. Indeed, for noSA and SAcond the RPW effective length uncertainties remain between +/- 40 and 50 cm, for averaged L_{eff}.of ~ 7.5 m. SAdiel situation, however, generates uncertainties greater than +/- 2 m, on strongly reduced L_{eff} (between 0.3 and 5.8 m). Again, note that L_{eff} between RPW2 and 3 should be zero as E is vertical, but the drift velocity of secondary particles and photoelectrons generates potential discrepancy not linked to E measurement.

5.5. Conclusion on study of Solar Arrays impacts on RPW effective lengths

The above study and simulation comparison showed how problematic, harmful and incapacitating the presence of fully dielectric rear solar array faces should be on the RPW instrument. Electric field determination by differences of potential between stacers would be erroneous, as RPW steady potential will be completely submitted to strong negative potentials effects behind the solar panels, with corresponding particle disturbances around them. The here-simulated drift velocity of particles, linked to the $E_{perp} \times B$, worsens electrostatic potential discrepancies and, finally, RPW system becomes effectively shortened and blinded by the environment.

Obviously, this study is based on a “worst case corresponding parameters”, as required by the working team, concerning the imposed magnetic field value, dielectric material properties and dimensioning, plasma conditions. One interesting study would be in the future to make those elements vary between this present extreme situation and more favourable conditions, to estimate how much SA could be degraded (*i.e.* with non-conducting rear faces) to reach RPW limitations. Several proportions of dielectric patches on rear SA faces should be considered, making vary in parallel the intensity of B (and thus the drift velocity), and the heliocentric distance of the system (which means changing densities and temperatures of particles, UV flux intensity, SC velocity and Solar Array Angle). It goes without saying that numerous cases involving long simulations will be necessary to fulfil the corresponding grid of situations. But in the frame of the present contract, all necessary inputs for this ideal study (*geo* files, meshes, physical groups and global parameters) are provided to the working teams to prepare the work.

6. Simulation results with recent Solar Orbiter configuration: biasing currents

6.1. Geometry updates

Global dimensioning of Solar Orbiter had been updated. Regarding previous model already presented in Section 3 (used in Section 4), and the intermediate evolutions presented on the last model of Section 5, special improvements have been brought to the SC heatshield, modelling apertures at the corners to prepare implementations of scientific instruments such as SWA-HIS and SWA-PAS. The spatial gap with respect to SC body (8 cm gap between shield rear face and SC body) has also been added (Figure 35).

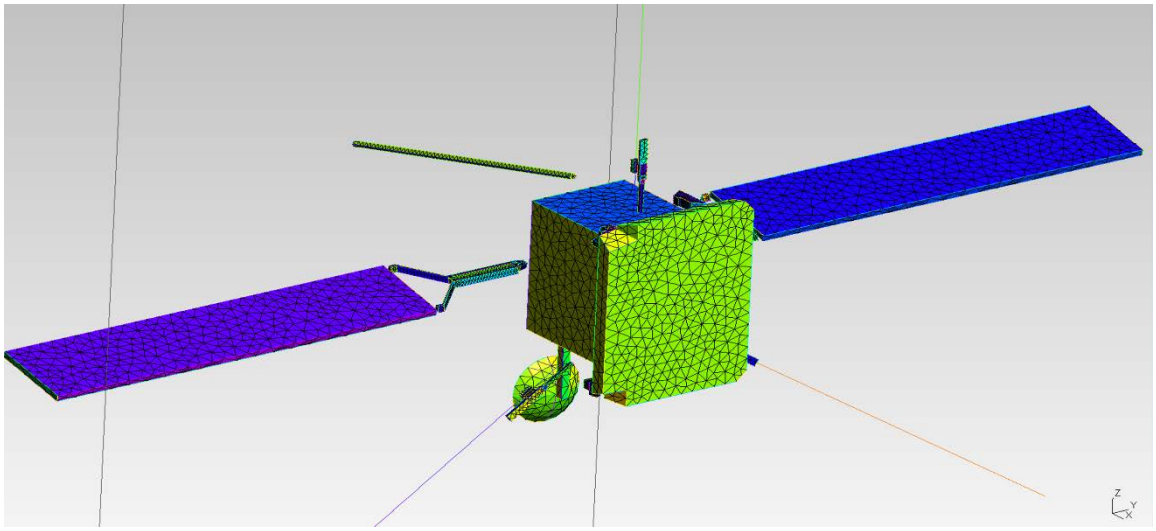

Figure 35 : New design of Solar Orbiter CAD model, more realistic. Here a focus on the Heatshield with apertures at the corners for SWA-HIS and PAS instruments

Solar array yokes (Figure 36), also above mentioned in Section 3.2, are now implemented. They stand for important elements as they are partly covered with non-conducting material on their sunlit faces (with Optical Solar Reflector or OSR). Rotation of “solar panels + yokes” assembly has also been implemented, with the previously detailed SAA angle depending on the heliocentric distance of the satellite (in our case at perihelion this angle - SAA - equals 76.5°). This new configuration might influence this electrostatic pattern in a region near RPW detection plane, especially since they might present non conducting elements on their shadow faces.

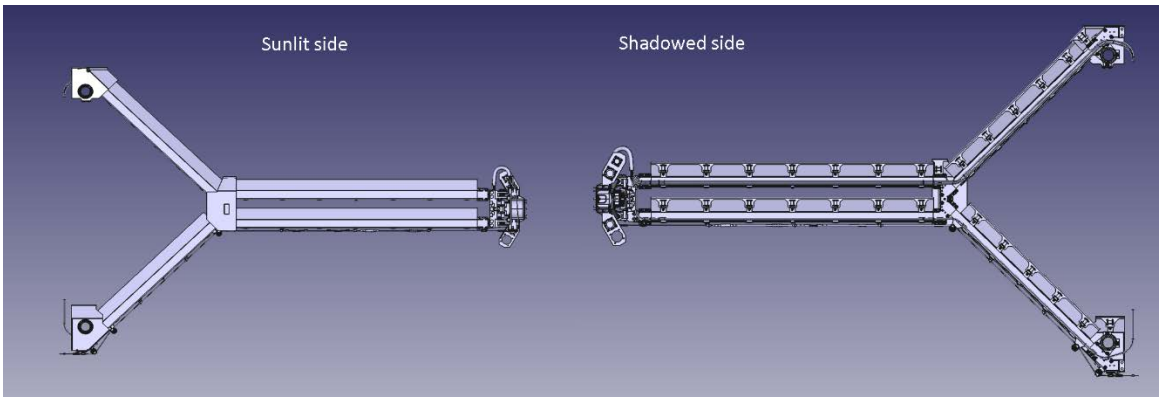

Figure 36 : Solar array yoke geometry (sunlit face on the left, shadowed face on the right). Front elements are shielded with OSR layers (non-conducting)

Other CAD improvements concern two instruments of the SWA experiment: HIS and PAS plus the SOLOHI instrument which have been added to our model HIS is shown on Figure 36, PAS on Figure 38 and SOLOHI on Figure 39. Indeed, some concerns have been reported about some parts of those instruments covered with a “possibly” not entirely conducting paint. Dielectric coatings in such environments and in the Sun shadow might reach strong negative potentials (~ -100 V). SPIS is the perfect tool to provide first estimations about possible consequences of such issues on environment measurement.

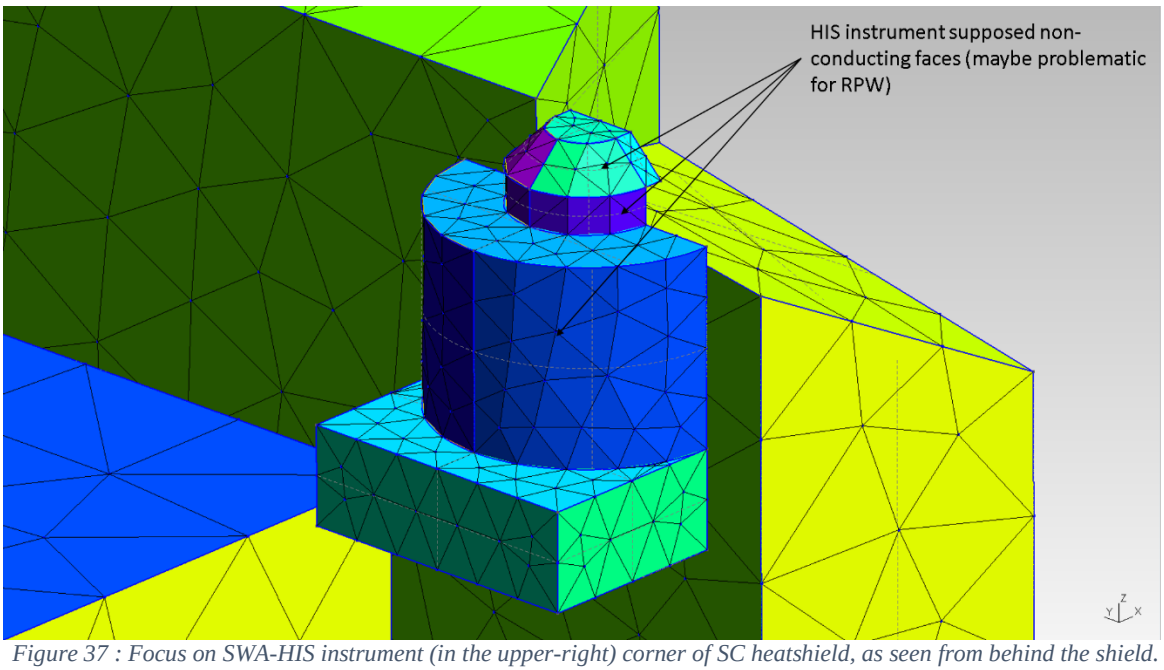

Figure 37 : Focus on SWA-HIS instrument (in the upper-right) corner of SC heatshield, as seen from behind the shield. Possibly non-conducting parts are pointed by arrows

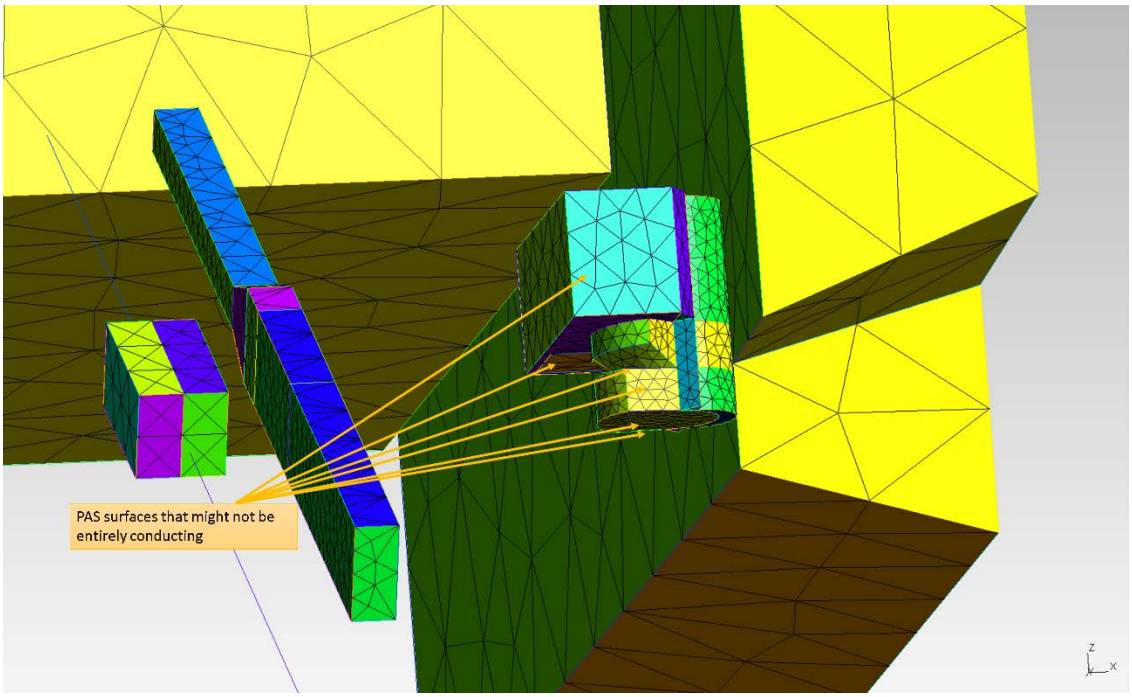

Figure 38 : Focus on SWA-PAS instrument (in the lower-right) corner of SC heatshield, as seen from behind the shield. Possibly non-conducting parts are pointed by arrows

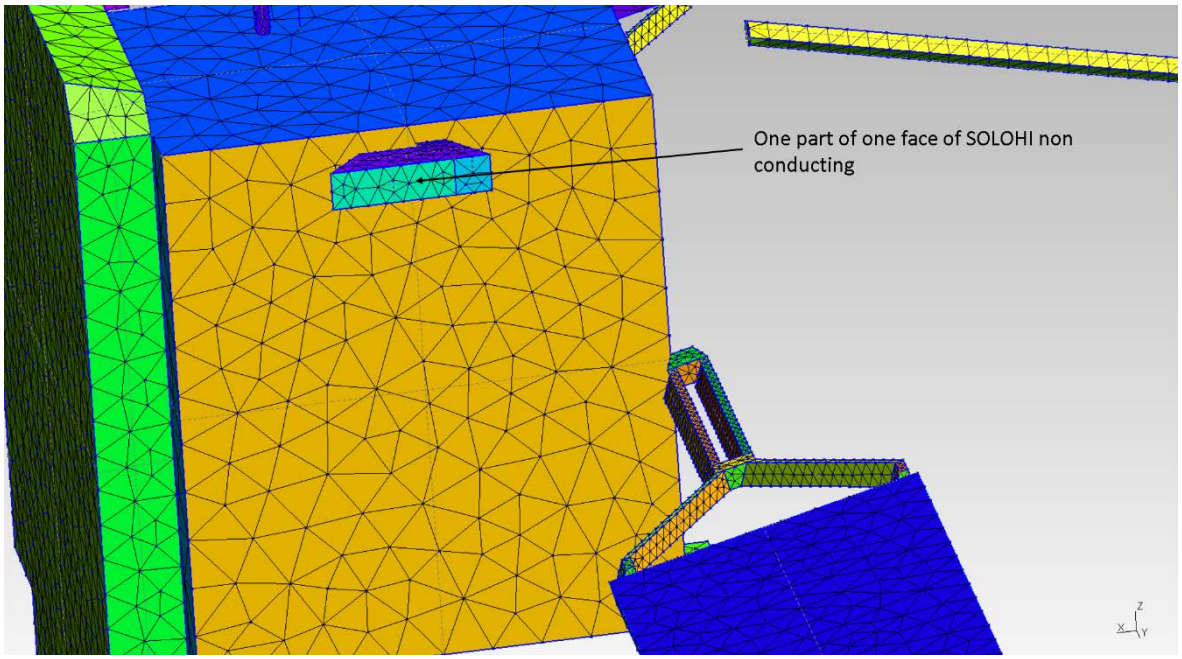

Figure 39 : Focus on SOLOHI instrument (+Y panel of SC body). Possible dielectric face is pointed by an arrow

The SWA-EAS instrument will be implemented in the next future.

6.2. Material updates

Other materials on SolO have been updated. Following table sums up the new configuration. Materials written in green are conducting, red ones are dielectric. Note that for electrical nodes 11 to 15 two possibilities of covering materials are offered, as it is not completely certain that chosen substances

will be conducting or not. Some tests will be performed in the following, while investigations are still ongoing at ESA. Solar array yokes in particular might present dielectric elements on their underneath faces, in shadow. RPW system is still considering the previously created materials: Elgiloy for the stacers and Niobium for their sunshields.

ElecNode	Name	ID	Localization	Material
0	SC BODY	117	“Center”	BK2K
0	SA1 rear	120	"-Y"	CFRP
0	SA2 rear	122	"+Y"	CFRP
0	SA1 side	124	"-Y"	CFRP
0	SA2 side	125	"+Y"	CFRP
0	HGA mast	197	"-Z"	BK2K
0	HGA	198	"-Z"	BK2K
0	BOOM	199	"-X"	CFRP
0	YOKE2 cond	1201	"+Y"	BK2K
0	YOKE1 cond	1203	"-Y"	BK2K
0	RPW1 shield	1702	"+Z"	NIOB
0	RPW2 shield	1706	"-Y"	NIOB
0	RPW3 shield	1710	"+Y"	NIOB
0	SC Shield	14156	"+X"	STEE
0	HIS cond	17072	"+Z"	BK2K
0	SOLOHI cond	18041	"+Y"	BK2K
0	PAS cond	19301	"-Z"	BK2K
0	RPW1 boom	1704	"+Z"	CFRP
0	RPW2 boom	1708	"-Y"	CFRP
0	RPW3 boom	1712	"+Y"	CFRP
1	RPW1	1703	"+Z"	ELGI
2	RPW2	1707	"-Y"	ELGI
3	RPW3	1711	"+Y"	ELGI
4	RPW1 preamp	1701	"+Z"	CFRP
5	RPW2 preamp	1705	"-Y"	CFRP
6	RPW3 preamp	1709	"+Y"	CFRP
7	SA1 front	119	"-Y"	CERS
8	SA2 front	121	"+Y"	CERS
9	YOKE1 diel	1202	"-Y"	OSR2K
10	YOKE2 diel	1200	"+Y"	OSR2K
11	HIS diel	17073	"+Z"	NP2K/BK2K
12	SOLOHI diel	18040	"+Y"	NP2K/BK2K
13	PAS diel	19300	"-Z"	NP2K/BK2K
14	YOKE2 diel in shadow	1204	"+Y"	KAPT/BK2K
15	YOKE1 diel in shadow	1205	"-Y"	KAPT/BK2K

6.3. Simulations

In the following, several simulation of Solar Orbiter in its latest and most up-to-date configuration, as described in the previous Section, will be presented. The environment considered is still the one at the satellite perihelion, but the RPW system will now provide biasing currents to the RPW stacers. Indeed, as explained at the beginning of this document, RPW system allows injection of biasing current in the antennas, in order to bring stacer potentials as close as possible to local plasma potential. Those I_{bias} currents can vary independently between +/- 70 µA, with 1024 possible steps, and are injected with a precision inferior to 0.15 µA. Electric potential of any antenna with respect to the SC ground should be measured with an accuracy of 2 mV. It is thus possible to generate I_{bias}-V_{RPW} curves, characterizing antenna's response to the total current balance. This parametric study is going to be presented in the following, with a main focus on satellite various potentials, instead of plasma distribution.

It first starts with a simple reference case without any magnetic field (*i.e.* without any induced electric field), without biasing current and without any dielectric surface in the sun shadow. According to document RPW-SYS-SRD-00040-LES_Iss02rev01(Science_Requirements) and considering the Parker spiral at 0.28 AU, we determined that for a 0.28 AU case with realistic fields: we might consider a magnetic field *B* of 124.4 nT oriented in the *X*-*Y* plane with components of $By = 36.3\times10^{-9}$ T and $Bx = -119.7\times10^{-9}$ T (this makes an angle of ~17° with the -*X* direction). Note that this *B* field is considered in order to generate the expected electric field *E*, which should then be *Ez* = +7.38 mV/m, fully vertical. Spacecraft velocity in the plasma reference frame is +400 km/s along *X* (to simulate the bulk velocity of particles) and -60 km/s along *Y* (to simulate Solar Orbiter motion normal to Sun direction at perihelion). Other plasma parameters such as particle densities and temperature remain unchanged regarding perihelion environment used and described in the previous Sections, but are reminded hereafter:

- Ions: H+, PIC with Maxwellian distribution and drift,
- Electrons: PIC with Maxwellian velocity distribution function,
- Photoelectrons: PIC with Maxwellian velocity distribution function and with a characteristic temperature k_BT_{ph} = 3 eV,
- Secondary Electrons under Electron impact (SEEE): PIC with Maxwellian velocity distribution function and with a characteristic temperature k_BT SEEE = 2 eV, backscattered electrons with 2/3 of their initial energy,
- Secondary Electrons under Proton impact (SEEP): PIC with Maxwellian velocity distribution function and with a characteristic temperature k_BT SEEP = 2 eV,
- External boundary conditions: Fourier, $1/R^2$ decrease of potential

Environment parameters	Values at 0.28 AU from the Sun
Sun flux (# 1 AU)	12.76
Electron and Proton density (m^{-3})	1.04×10^8
Electron temperature (eV)	21
Proton temperature (eV)	27
Spacecraft velocity in X direction (m/s)	400000.0
Proton bulk velocity in Y direction (m/s)	-60000.0

Then the same case but with dielectric elements in shadow will be compared to the reference, in order to estimate biases induced by the above mentioned "possibly" not entirely conducting paint on parts of the instruments SWA-PAS, SWA-HIS and SOLOHI. This worst case also considers non-

conducting Kapton elements on the shadowed areas of the solar array yokes, but rear faces of solar arrays remain conducting. This second simulation with dielectrics in shadow does not include any magnetic field as the simulation is extremely long to run (necessary charging time for non-conducting surfaces, not submitted to UV light), and might also stop before ending (see next Section). But it will however give an estimation for disturbances generated on RPW antennas.

Finally, the reference CAD model without dielectric in shadow will be immersed in a magnetized plasma (same *B* value for all simulations), and be submitted to several biasing currents into its antennas, in order to give a first drawing of I_{bias}-V_{RPW} curve for this specific environment.

6.4. Important caution

This concerning the present particular study and all SPIS simulators whom impose magnetic fields.

The solver used by SPIS in the presence of a magnetic field is not the same that the one used without *B*. Sometimes, simulations with *B* block, without any information appearing in the SPIS console, and do not evolve or progress anymore. They have to be manually stopped and results need to be extracted, if they have advanced enough to produce any. If the blocking happens before the simulation reached its equilibrium, or the desired duration, it must be restarted from the beginning.

According to SPIS-NUM developers, this situation is generated by at least one super-particle which remains “blocked” or “stuck” between two tetrahedra. It is a problem that sometimes appears, and more particularly when there is a magnetic field imposed over the computational volume. The origin is “simply” a numerical precision problem. In this case, only few computer processors will continue working (among the number of threads asked to be used in the simulation process) and with much lower activity. Processors will keep computing indefinitely, as in an infinite loop. This precision problem is an old issue affecting all the plasma codes using a grid: when one wants to know in which mesh element is the particle (to interact with the fields defined on the grid) he can always find one that is actually nowhere, because of the limited number of bits to encode floating numbers. The problem is worse on an unstructured mesh as in SPIS, especially since some tetrahedra are far from the “ideal tetrahedron shape”. The particle movement of gyration due to *B* even increases the number of host tetrahedra changes, and therefore the probability that this problem arises. This issue seems to be for now inevitable. Some ideas exist to overcome this phenomenon, however they apparently require a redesign of SPIS numerical core, and this project (carried on the magnetic field) it is not for right away.

During this project, the only solution available was to act to try to decrease the probability that blocked particles occur. As it risks to happen more frequently if the mesh used is of “poor quality”, with distorted tetrahedra in some regions of the volume, special attention has been paid on the mesh quality. Even if a same mesh can be used unsuccessfully for a simulation that suddenly freezes, and then re-used without trouble for the exact same simulation that has been re-launched without changes, in our cases, blockings happened on 90% of simulations. This is why meshing parameters in this current CAD model have been considerably enhanced in order to improve computational grid aspect and reduce as much as possible risks of blocking situations. It has been managed to reduce occurrences of blockings, even though they still happen on 50% of our cases. For the Solar Orbiter configuration, with complex geometries of both small and large elements, thin wires, small spaces between elements and of courses magnetic fields: this was a harsh task. Especially with the new spacecraft elements added (yokes, HIS, PAS, SOLOHI) and the degree of precision required around RPW antennas. Note that with GMSH (embedded SPIS CAD modeller), users don’t have entire control of meshing. As explained in the first part of this report, user define mesh size on SC elements, on volume boundary and on every point he wishes to create. But 2D and 3D meshing is made automatically. One possibility exists of generating well-structured meshes with GMSH, but it remains much longer to set and practically unfeasible with this complex satellite and instrument geometries. So in our case, problematic mesh elements cannot be avoided.

These are the reasons why this study has been significantly slowed down, and why, in the following, some simulations seem to be stopped before that a visible steady-state equilibrium of SC potentials has been reached. Those results are the most advanced reached by the software.

6.5. Reference case: no *B*, no I_{bias}, no Dielectrics in shadow

Time evolution of spacecraft potentials is displayed on Figure 40. Average potential values has been averaged over the time period: *t(s)* = 3.5 s → 6 s, which represents here 418 time steps and the same number of measurement points, and are presented in the next table.

We now distinguish the standard deviation σ(V) and the error $\Delta\Phi(V) \sim \sigma\ (\sqrt{2})/3\ (\sqrt{N})^{-1}$.

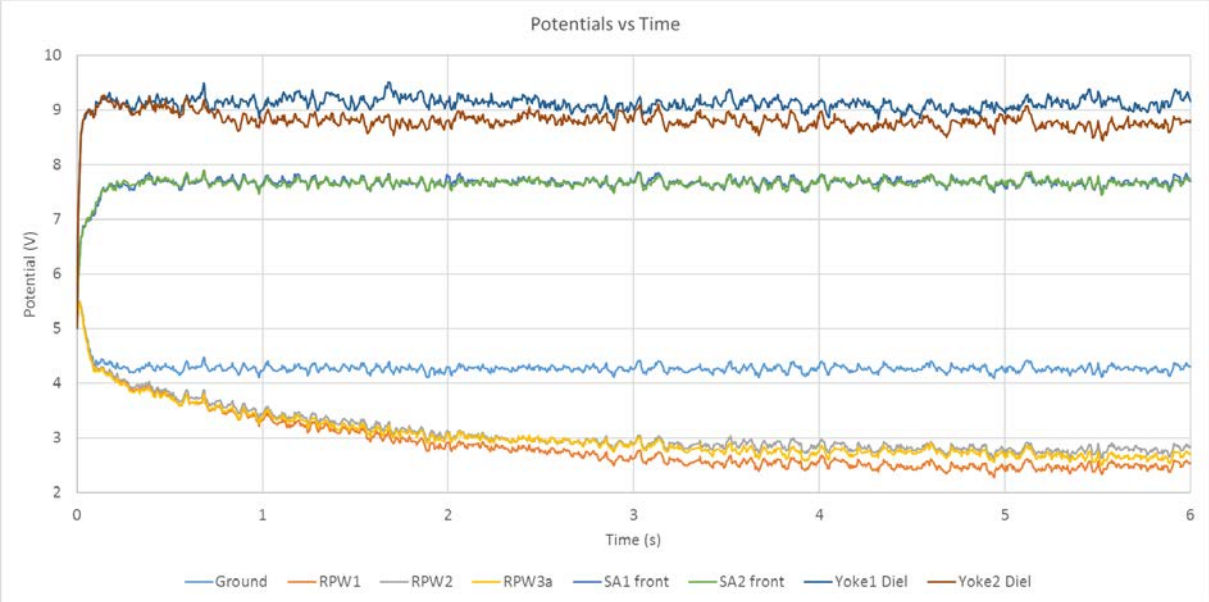

Figure 40 : Reference Case - Time evolution of SC potentials

	Ground	RPW1	RPW2	RPW3	SA1 front	SA2 front	Yoke1 Diel	Yoke2 Diel
Φ (V)	4.264	2.492	2.812	2.712	7.678	7.667	9.094	8.748
σ (V)	0.060	0.069	0.072	0.074	0.067	0.071	0.104	0.099
ΔΦ (V)	0.001	0.002	0.002	0.002	0.002	0.002	0.002	0.002

It can be noticed on the above table that even with absence of induced electric field over the computational volume, RPW1 is slightly less positive than the lower RPW2 and 3 stacers, of about 0.3 V. Indeed, those last stacers are closer to each other (an angle of 110° while between 1 and 2 or 1 and 3 it equals 125°). Furthermore, RPW experiment geometry generates this discrepancy. Indeed, the positive faces of solar arrays and yokes are oriented towards RPW1, and their charging levels (between +7 and +9V) attract efficiently incoming thermal electrons and other spacecraft emitted particles. RPW1 is also normal to the satellite body upper panel, while RPW2 and 3 are below the spacecraft, linked to the corners of Solar Orbiter body, and the HGA is between them, behind their plane. Actually, this discrepancy has already been observed with the previous CAD model of Solar Orbiter in a simulation case without any imposed electric field (see Section 4.1).

This 0.3 V of difference between upper and lower stacers can be considered as a “natural” offset, which should be compensated using biasing currents.

6.6. Worst case: no *B*, no I_{bias}, but with Dielectrics in shadow

The worst case is configured such as all materials written in red in the previous table of Section 6.2 are activated. So, for the following table rows, we do have the red-written dielectric materials, even in shadow. We thus expect negative electrostatic potentials on several surfaces, in the vicinity of RPW.

ElecNode	Name	ID	Localization	Material
7	SA1 front	119	"-Y"	CERS
8	SA2 front	121	"+Y"	CERS
9	YOKE1 diel	1202	"-Y"	OSR2K
10	YOKE2 diel	1200	"+Y"	OSR2K
11	HIS diel	17073	"+Z"	NP2K/BK2K
12	SOLOHI diel	18040	"+Y"	NP2K/BK2K
13	PAS diel	19300	"-Z"	NP2K/BK2K
14	YOKE2 diel in shadow	1204	"+Y"	KAPT/BK2K
15	YOKE1 diel in shadow	1205	"-Y"	KAPT/BK2K

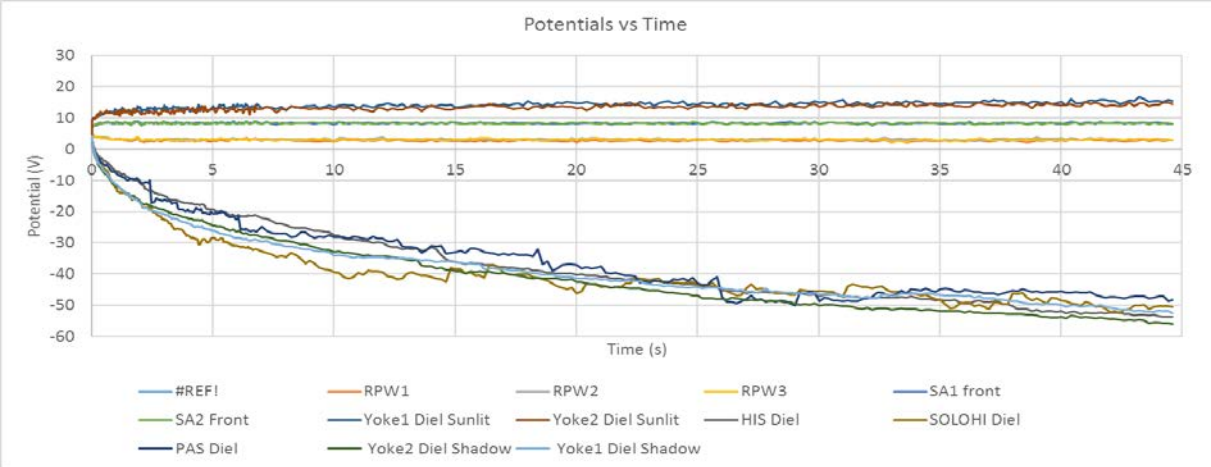

Figure 41 : Worst Case - Time evolution of SC potentials

For the rest: Spacecraft other materials, configuration and environment remain unchanged with respect to the previous reference case. Time evolution of spacecraft potentials is displayed on Figure 41.

Despite the fact that simulation stopped before reaching stable state, potentials seem to be almost at equilibrium. Averaged values computed after t = 35 s are summarized in the following table, where previous reference case and present worst one are compared. As equilibrium potentials were not totally reached over this late period, σ and ΔΦ for dielectrics in shadow are higher than for other surfaces, and their potentials visibly tend towards -50 to -60 V.

SC Element \ Value	REF Φ (V)	σ (V)	ΔΦ (V)	Worst Φ (V)	σ (V)	ΔΦ (V)	Diff Worst#REF (%)
Ground	**4.264**	0.060	0.001	**4.176**	0.131	0.009	**2.1**
RPW1	**2.492**	0.069	0.002	**2.723**	0.222	0.015	**9.3**
RPW2	**2.812**	0.072	0.002	**3.136**	0.244	0.016	**11.6**
RPW3	**2.712**	0.074	0.002	**2.987**	0.209	0.014	**10.2**
SA1 front	**7.678**	0.067	0.002	**8.301**	0.204	0.014	**8.1**
SA2 front	**7.667**	0.071	0.002	**8.226**	0.180	0.012	**7.3**

Yoke1 Diel Sun	**9.094**	0.104	0.002	**15.133**	0.512	0.034	**66.4**
Yoke2 Diel Sun	**8.748**	0.099	0.002	**14.200**	0.435	0.029	**62.3**
HIS Cond/Diel	**4.264**	0.060	0.001	**-51.326**	1.779	0.120	**1303.7**
SOLOHI Cond/Diel	**4.264**	0.060	0.001	**-49.611**	1.448	0.098	**1263.5**
PAS Cond/Diel	**4.264**	0.060	0.001	**-46.259**	0.991	0.067	**1184.9**
Yoke2 Cond/Diel Shadow	**4.264**	0.060	0.001	**-53.597**	1.201	0.081	**1357.0**
Yoke1 Cond/Diel Shadow	**4.264**	0.060	0.001	**-49.605**	1.759	0.118	**1263.3**

It is remarkable in the above table that the presence of various non-conducting surfaces in shadow and in the vicinity of RPW antennas affect the potentials of the stacers by around 10%. The corresponding effective lengths will thus also be modified by this percentage, even though here the L_{eff} computation is irrelevant as no electric field is applied over the simulation volume.

We also notice the important discrepancy between potentials on sunlit dielectric surfaces of yokes with conducting/not conducting sun-shaded faces of yokes. In the worst case: strong negative potentials in the back of the yokes generate an important compensation in the front, with more positive charging. Finally: the worst case configuration involves for SPIS stronger SC potential fluctuations. On average, even when considering only the conducting and sunlit dielectric elements, σ (V) for the worst case is 3.5 times higher than for the reference, and ΔΦ (V) 10 times higher.

Stacer potential discrepancies of "only" 10% between those two cases seems weak, as in the worst case situation we have strong negative potentials (~ -50 V) in the vicinity of the RPW experiment. Explanation lies in the fact that firstly, conducting SC elements remain positively charged, including antennas, so local negative potentials on small areas do not affect intrinsic level of charging of Elgiloy wires. Secondly, strong local densities of photoelectron and secondaries are lowering Debye length and reducing expansion of negative potential « bubbles ». This appears on the next Figure 42 presenting plasma potential in RPW plane, and negative volumes generated by dielectric elements which do not really disturb local potential close to the antennas. Only SoloHI charge interferes with field lines of Φ between RPW1 and 3. Referring to Section 5.4, we notice that the single rear yoke faces covered with non-conducting material do not dislocate the electrostatic pattern below the spacecraft as the non-conducting rear solar array faces did. The much smaller surface considered here explains this phenomenon.

However, the above mentioned local negative potentials still repulse electrons (ambient and spacecraft-generated ones) which are redistributed around RPW antennas and modify the collected/emitted currents on them. This modification contributes in varying steady Φ_{RPW}, and thus corresponding L_{eff} by 10% on average.

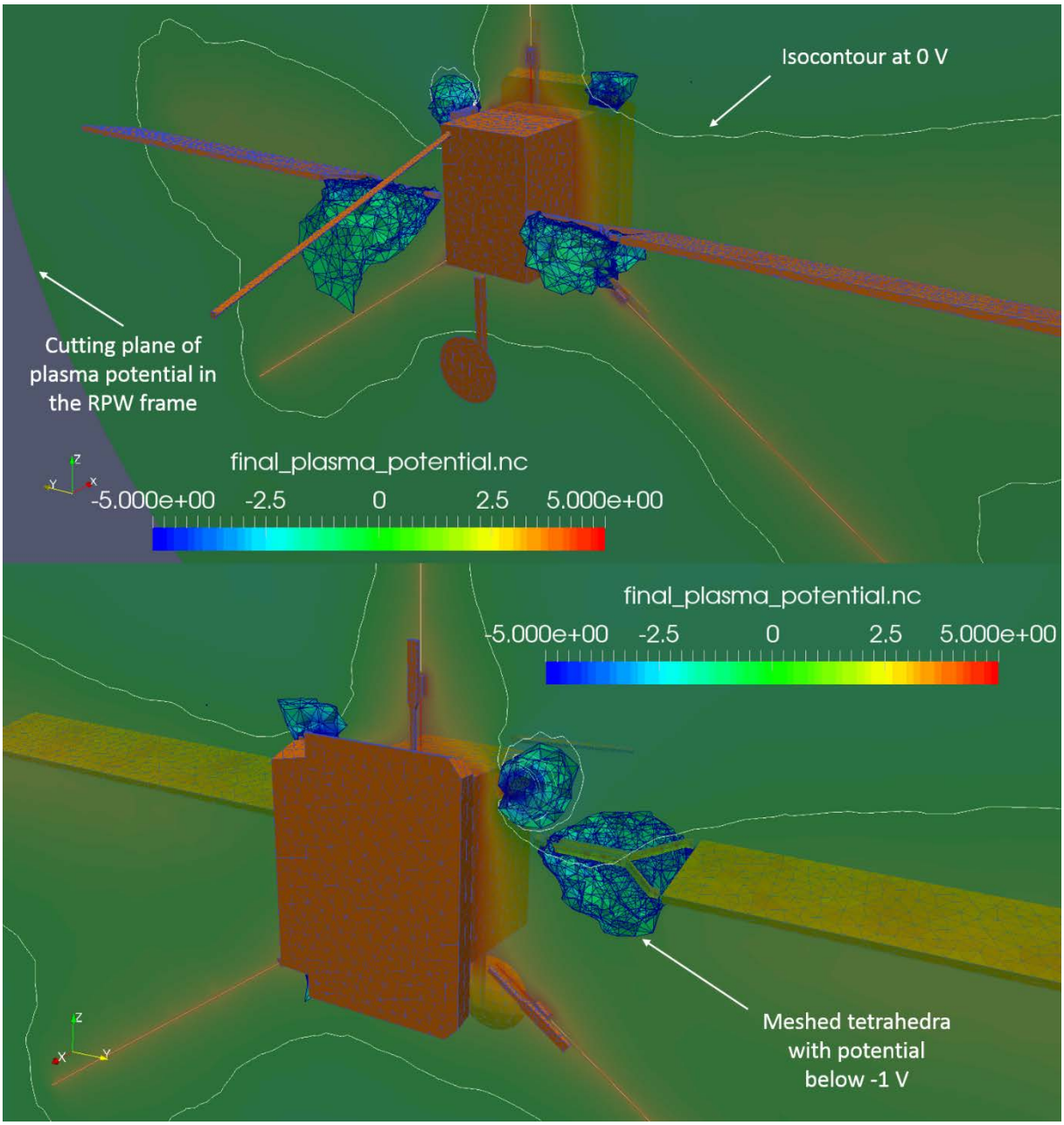

Figure 42 : Worst Case – Solar Orbiter and plasma potential in RPW plane viewed from behind (top) and front (bottom) of the SC. The isocontour line at 0 V is traced in white. 3D meshed tetrahedra represent plasma elements which electrostatic potential is below –1 V.

6.7. Other cases: B, no Dielectrics in shadow, but making I_{biais} vary

The following series of simulations is based on the reference case, but this time adding the magnetic field *B* of 124.4 nT oriented in the *X-Y* plane with components of $By = 36.3\times10^{-9}$ T and $Bx = -119.7\times10^{-9}$ T (this makes an angle of ~17° with the -X direction). This B field is considered in order to generate the expected electric field *E* (Section 6.3) *Ez* = +7.38 mV/m, fully vertical. The aim is now to inject a varying biasing current into the RPW wires, and observe the corresponding evolution of potentials on them. Note that with SPIS it is not possible to directly inject the desired I_{bias} (A) into wires but only a current per meters square on elements (A/m^2). Surface of one wire is on the CAD model provided (GMSH) S_{RPW} = 0.520285 m^2 and on for preamp S_p = 0.101989 m^2 (to close the current loop).

This allows the conversion of user input I_{bias} (A/m^2) into the expected current in Amperes. Finally, the biasing current will vary as follow: -5, -3.75, -2.5, 0, 5 µA. Due to SPIS limitations concerning simulations with imposed magnetic field (see Section 6.4), we could not perform as many simulations as expected, due to schedule constraints, but the here-presented set of cases gives a good overview of the RPW system behavior when submitted to biasing currents. And it can also be completed in the next future by other teams involved in this project, thanks to provided simulation sets.

In the following, only steady potentials at equilibrium on various Spacecraft elements will be presented (if it that equilibrium could be reached before simulation stopped), as the main interest is to study RPW final potentials, depending on chosen I_{bias}. Results such as particle distribution in volume or plasma potential around Solar Orbiter will not be displayed. However, all other data remain available with simulation packages.

The following table sums up averaged potentials obtained on Solar Orbiter surfaces as a function of I_{bias}.

I_biais (µA)	RPW1 (V)	RPW2 (V)	RPW3 (V)	Ground (V)	SA1 front (V)	SA2 front (V)	Yoke1 Diel (V)	Yoke2 Diel (V)
-5.000	**-1.919**	**-1.684**	**-1.755**	**6.854**	**10.242**	**10.207**	**12.315**	**12.034**
σ (V)	*0.498*	*0.505*	*0.506*	*0.484*	*0.465*	*0.474*	*0.568*	*0.536*
-3.750	**0.779**	**1.192**	**0.935**	**5.729**	**9.146**	**9.144**	**10.590**	**10.267**
σ (V)	*0.215*	*0.216*	*0.218*	*0.217*	*0.245*	*0.276*	*0.233*	*0.250*
-2.500	**2.178**	**2.471**	**2.433**	**5.813**	**9.222**	**9.201**	**10.642**	**10.312**
σ (V)	*0.258*	*0.262*	*0.262*	*0.264*	*0.310*	*0.316*	*0.282*	*0.283*
0.000	**4.196**	**4.416**	**4.388**	**5.907**	**9.324**	**9.279**	**10.777**	**10.463**
σ (V)	*0.283*	*0.284*	*0.284*	*0.283*	*0.353*	*0.323*	*0.334*	*0.298*
5.000	**7.364**	**7.509**	**7.318**	**6.151**	**9.254**	**9.220**	**10.779**	**10.367**
σ (V)	*0.283*	*0.284*	*0.284*	*0.283*	*0.353*	*0.323*	*0.334*	*0.298*

The next plot on Figure 43 displays evolution of the 3 RPW potentials as a function of I_{bias}.

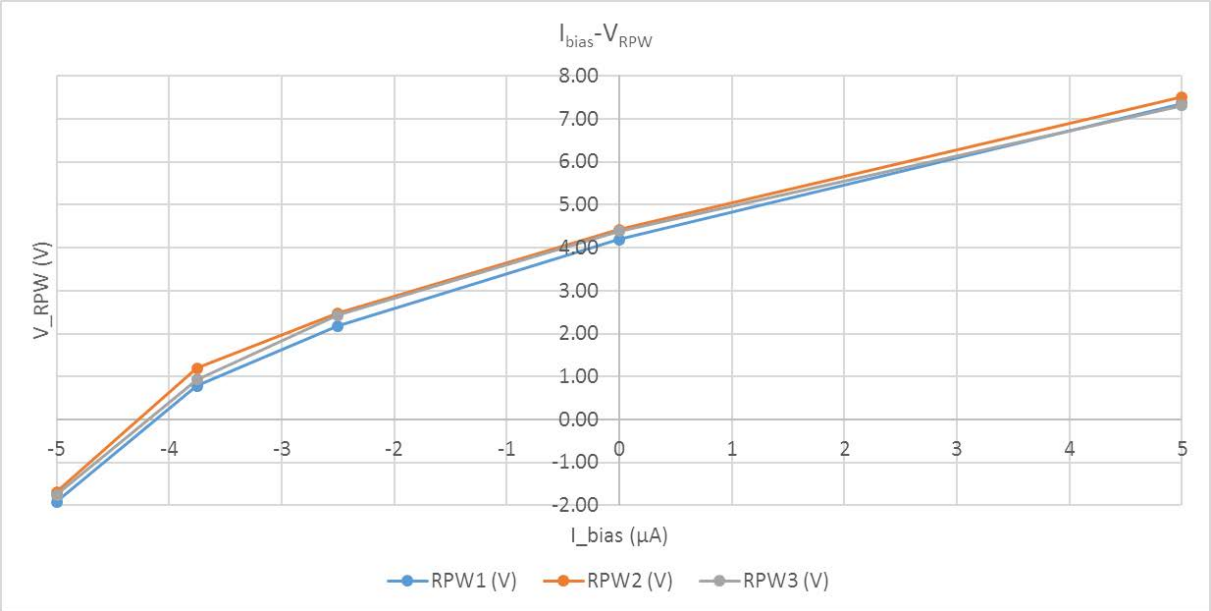

Figure 43 : I-V curve for the last SC configuration in the perihelion environment, at 0.28 AU, for a vertical electric field of 7.38 mV/m.

A better overview of RPW behavior as a function of the biasing current would have required more points below -5 µA et beyond 5 µA. Unfortunately, long simulation durations and sometimes necessity of re-launching the cases because of computation blockings prevented this study from going further. However, thanks to this actual scanned range it can be assessed that antennas reach neutral potential for an injected biasing current of -4.3 µA, for this Solar Orbiter perihelion environment.

With this sort of parametric study, varying I_{bias} without changing imposed electric field, it does not make sense to reason in terms of effective lengths. Indeed, the theoretical E field of 7.38 mV/m is much too weak compared to electrostatic pattern generated by the spacecraft and the antennas themselves. Indeed, considering the maximum geometrical length from one RPW tip to another (~15 m), the expected maximum variation of potential over the RPW area should be ~ 0.1 V. But for each case here, the actual differences of potentials between stacers are too important to recover the theoretical effective length. Potential fluctuations and standard deviations (see above Table) are beyond the precision needed at this level of background electric field. Satellite charged surfaces dominate local fields and prevent numerical antennas to clearly detect the signal we want to observe. Using the above mentioned formulas $E = -\partial\Phi_{ij} / L_{ij}$ and $\Delta L_{ij} = L_{ij} ((\Delta\Phi i + \Delta\Phi j) / (\Phi i - \Phi j))$ we find effective lengths values greater than 40 m, with ΔL even larger. It is explainable by the fact that σ is here greater than potential gaps between stacers. Previous simulations presented in Section 4.3 were based on much stronger $V \times B$ fields, which dominated plasma around the Solar Orbiter structure and were than much more visible thanks to Φ_{RPW} discrepancies.

In order to evaluate more precisely effective lengths, stronger magnetic fields should be applied on the computational volume.

7. Overview of the results concerning L_{eff}

We can compile former results dealing with effective lengths computation, obtained before Section 6, in order to present L_{eff} magnitudes depending on spacecraft various geometries. The following diagram illustrates through various sketches the considered cases (from 1 to 6). For all those simulations a $V \times B$ induced electric field was applied, with various values.

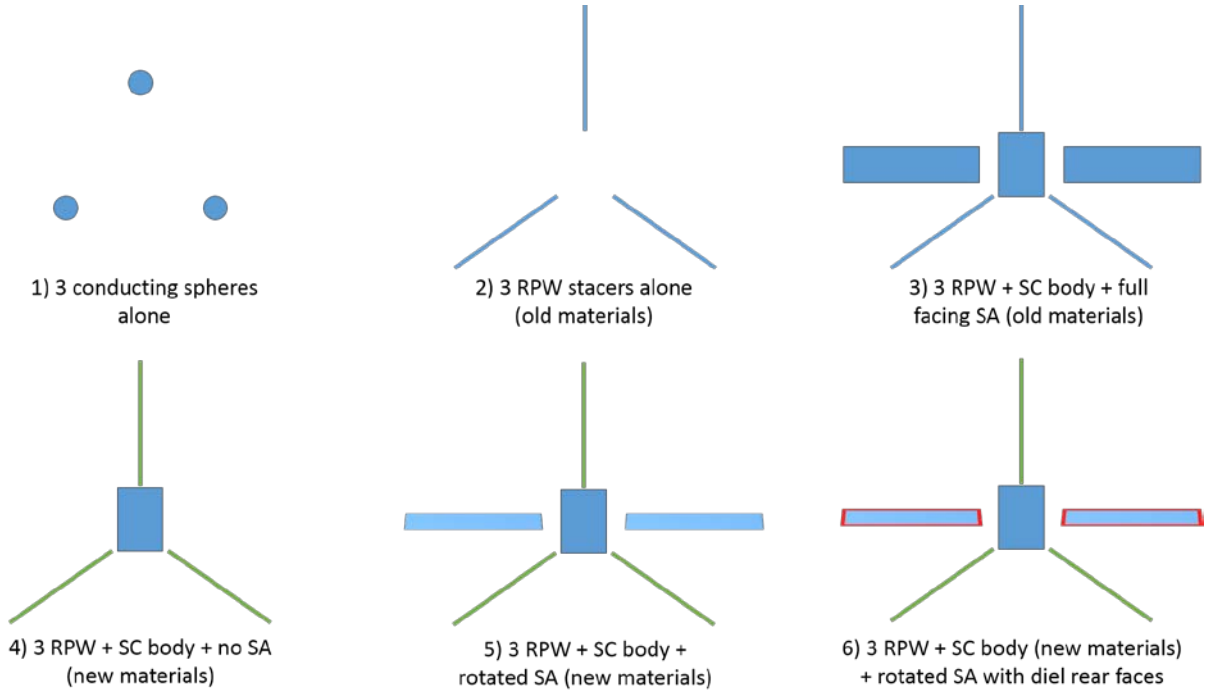

Configuration	1	2	3	4	5	6
ΦRPW1 (V)	13.15	Range	Range	5.04	3.58	1.69
ΦRPW2 (V)	15.93	Range	Range	7.53	6.37	1.82
ΦRPW3 (V)	22.35	Range	Range	8.81	6.69	4.01
Leff 1-2 (m)	**6.80**	**5.83**	**4.83**	**6.28**	**7.05**	**0.33**
Leff 1-3 (m)	**6.80**	**5.83**	**4.83**	**9.51**	**7.86**	**5.88**
Leff 2-3 (m)	**6.40**	**0.00**	**0.00**	***3.23***	**0.82**	**5.55**
Lgeo_min 1-2 (m)	7.59	4.12	4.12	4.12	4.12	4.12
Lgeo_max 1-2 (m)	7.59	15.65	15.65	15.65	15.65	15.65
Lgeo_min 2-3 (m)	7.01	3.50	3.50	3.50	3.50	3.50
Lgeo_max 2-3 (m)	7.01	14.15	14.15	14.15	14.15	14.15

In the above Table "*Lgeo*" stands for the real geometric distance between elements (spheres or wires). It sums up previous observations made during corresponding simulation analysis earlier in this report.

8. Conclusion on RPW study

As detailed in the following section, this project achieved to comply to *almost* all RPW requirements for SPIS modelling.

Despite numerical issues of precision inherent to any PIC code when considering magnetic fields applied over the computational volume, which generate sometimes unstable simulations and require re-launches of runs, this study provided answers to many questions raised from the RPW experiment. An adequate Solar Orbiter model including the desired RPW system and other modular elements (HGA, solar arrays, yokes, instruments and rear boom) was conceived and updated all along the project. This model is fully parametrized and easily modifiable, even though it is updated with latest information available concerning materials and dimensions of the satellite. New materials have also been generated for SPIS to simulate the relevant Elgiloy and Niobium surfaces. Note that Elgiloy requires updated data on its photoemission properties (ONERA) but they were not available by the end of this project.

Effective lengths estimation studies were performed with up-to-date materials on RPW but without spacecraft elements such as solar array yokes or SWA and SoloHI instruments. It should be completed with latest spacecraft model. This one however provided the required I-V curves for antennas in a typical perihelion environment at 0.28 AU from the Sun.

All required and necessary models and datasets were provided to LESIA in order to continue analysis of the spacecraft environment and its effect on the RPW measurements throughout the pre- and post-launch period.

9. RPW requirements for SPIS modelling: compliance table

Requirement Number	Requirement	Descriptive Explanation	**Project Achievements**
	Spacecraft Model Requirements		
RPW-SPIS-0010	The project shall provide a spacecraft model suitable for use in the SPIS toolkit and which appropriately supports the needs to assess the satellite perturbations on the RPW		**Done**. Spacecraft model provided to LESIA and ESA.
RPW-SPIS-0020	The model shall include all spacecraft surfaces which will provide, or potentially may provide, a significant perturbation of RPW DC measurements.	HGA, Solar panels	**Done**. All concerned surfaces included in the model provided to LESIA and ESA.
RPW-SPIS-0030	The model shall be updated to include any significant design modifications communicated to the modelling team during the contract.		**Done**. Model frequently updated during the project. Latest relevant model provided. Elgilloy material requires updated data on photoemission properties (ONERA).
RPW-SPIS-0040	The model geometry shall be parameterized to include flexibility to model potentially relevant future changes.	Further changes may be required if, for example, the Prime introduces a series of baffles to the spacecraft design in order to address presently unresolved contamination issues.	**Done**. Provided model is entirely Modularized and parameterized with corresponding descriptions included in all geo files.
RPW-SPIS-0050	The spacecraft model shall provide the ability to assess the effect of movable sub-units (e.g. the HGA and the Solar Arrays) on the measurements of RPW.	It is anticipated that the orientation of these surfaces will continue to vary during the mission.	**Done**. Parameters allowing HGA and Solar Arrays rotations are available in the geo files.

RPW modelling Requirements			
RPW -SPIS-0060	An adequate SPIS model of the RPW antennas need to be constructed so that a representative assessment of the impact of the spacecraft environment on the RWP measurements can be made.	May need to discuss the level of detail that needs to be included to achieve the representative results?	**Done**. Model discussed and configured with an optimum compromise between geo detail levels and numerical performances.
RPW -SPIS-0070	The modelling work shall provide the (I_{bias}, Φ) curves for a typical RPW antenna, in the case of no external electric field imposed in the simulation box and no spacecraft body.	I_{bias} is the typical biasing current which will be applied by RPW during its operations. . $I_{bias} = 0$ corresponds to floating antenna (BIAS off). The outcome will constitute the undisturbed (I_{bias}, Φ) curves.	**Disused**. RPW simulations without SC body completely change antennas charging levels and numerical stability. Stacer materials were also outdated. Results would have been totally unrealistic and irrelevant for this study.
RPW -SPIS-0080	The modelling work shall provide the (I_{bias}, Φ_i) curves for all three RPW antennas mounted on the actual Solar Orbiter spacecraft body.	I_{bias} is the typical biasing current which will be applied by RPW during its operations. The outcome will be compared to the undisturbed curves.	**Done** and presented in this report for the typical Solar Orbiter perihelion environment.
RPW -SPIS-090	The modelling work shall provide the 3D spatial distributions of the photoelectron density and electrostatic potential around the actual Solar Orbiter spacecraft body and the three RPW antennas and antennas boom.		**Done**. Some results of particle distributions and potential around RPW presented here. Other data available within the simulation packages provided.

RPW-SPIS-0100	The modelling work shall provide the ($\delta\Phi_{i12,23}$, I_{bias}) curves for all three RPW antenna, in the case of an external electric field imposed in the simulation box.	These (I_{bias} , Φ_i) curves shall allow determining the effective lengths vectors $\overrightarrow{L^*_{effij}}$ modified by the spacecraft electrostatic environment.	**Done** and presented in this report for the typical Solar Orbiter perihelion environment. But stronger E fields missing and necessary to determine more precisely L_{eff} for latest model
RPW-SPIS-0110	The modelling work shall allow to evaluate the effects on the RPW DC/LF measurements of the S/C body, high gain antenna & solar panels if the RPW antennas are tilted by 30° in the anti-sunward direction		**Disused** by ESA.
Model Run Requirements			
RPW-SPIS-0120	The models and their runs shall be saved in a commonly agreed format and presented in a commonly agreed way so that they can be re-used by the RPW instrument team at LESIA laboratory (France) and by the RPW science		**Done**. Models and runs saved, provided and presented to LESIA. Simulations already running on LESIA computers.
RPW-SPIS-0130	The RPW instrument team in LESIA shall have the complete set of model runs which would allow continued analysis of the spacecraft environment and its effect on the RPW measurements throughout the post-launch period.	This is to allow the RPW instrument team to assess the effect of any unanticipated environment and/or evolution of the properties of problem surfaces throughout the mission.	**Done**. Model runs provided to LESIA, ready to be updated for other analysis. Examples of new environment configurations also provided (Kappa distributions).

10. SWA-EAS aspects

10.1. Introduction

The Electron Analyzer System (EAS) is a part of the Solar Wind plasma Analyzer (SWA), displayed on Figure 44. EAS measures the electron bulk properties (including density *N*, velocity *V*, and temperature *T*) of the solar wind, between 0.28 and 0.8 AU heliocentric distance. It is made of a pair of top-hat electrostatic analyzers (Figure 45) with aperture deflection plates mounted in the shadow of the spacecraft at the end of the instrument boom. The two sensors provide an almost full 4π sr field of view (FOV) subject only to "minor" blockage by the spacecraft and its appendages. The sensors measure electron fluxes in the 1 eV to 5 keV energy range with 10−12% precision and 10 degrees' angular resolution. Moments of the electron velocity distribution at 4s time resolution will be routinely returned to ground even though the sensors can sample full 3D distributions at a higher rate and 2D electron pitch angle distributions at 0.125 s rate during short periods of burst mode. More technical properties of this instrument are displayed on Figure 46.

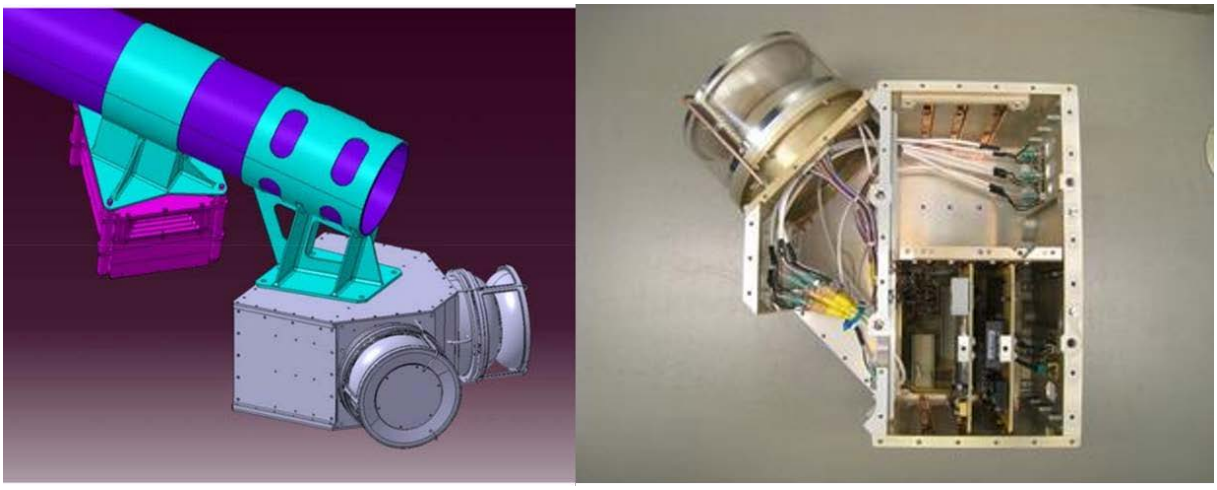

Figure 44: CAD model of the SWA-EAS sensors (left) and inside view of EAS (right). Image credit: UCL.

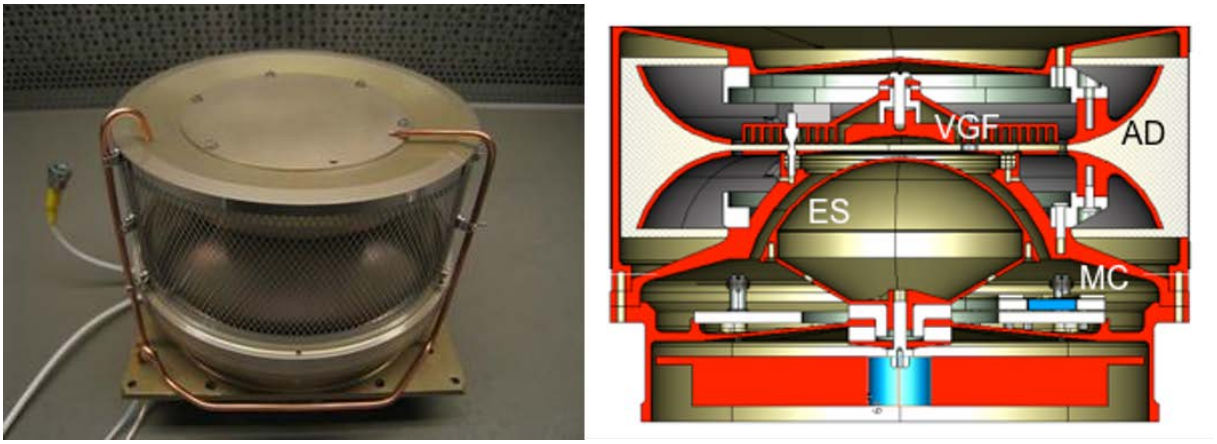

Figure 45: Focus on one EAS top-hat electron analyzer (left) and corresponding schematic cut (right).

At Solar Orbiter perihelion (0.28 AU) the solar radiation flux is about 10 times stronger than at 1AU and the solar wind is also significantly denser and hotter. The EAS detector may be contaminated by important fluxes of low energy secondary and photoelectrons, emitted by the spacecraft itself, and deflected towards the detectors by the local structures of the plasma and spacecraft potentials. The local

plasma potential is indeed modified by various spacecraft induced effects such as the charging of covering materials, the presence of an ion wake and high secondary electron / photoelectron densities, which in turn affect the measured thermal electrons Energy Distribution Functions (EDF). Compared with theoretical undisturbed EDF, simulations and former experiences show that EAS may measure density excess of more than 130% at perihelion with the largest discrepancy in the electron flow direction.

The tasks required here include providing a detailed and adaptable model of the Solar Orbiter spacecraft together with the definition of the characteristics of those surfaces which will be exposed to the space environment and that will have, or may possibly have, an effect on the electron population (*e.g.* modification of trajectories of electrons entering the instrument) to be measured by the SWA-EAS instrument. Model runs should be performed using realistic parameters representing the environments to be sampled by Solar Orbiter (*i.e.* over distances of 0.28 to 1.4 AU), in order that the major perturbations to the environment, and their effects on the SWA-EAS measurements can be identified and quantified. Moreover, capacity should be built in order to provide the means, in the post-launch period, to run the models for specific environments encountered and/or to assess the impact of a varying (or previously unanticipated) perturbation to the ambient plasma environment. The presence of an eventual baffle set behind EAS instrument will also be investigated, concerning its effects on EAS outputs, especially regarding the secondary electron pollution on measurements.

Parameter	Range/resolution	**EAS**	**PAS**	**HIS**
Sensors		2 x EA	1 x EA	1 x EA, 1 x TOF-SSD
Mass	Species	Electrons	H, He	^{3}He – Fe
	Resolution ($m/\Delta m$)	-	-	5
Energy	Range	1 eV – 5 keV	0.2 – 20 keV/q	0.5 – 100 keV/q (Az) 0.5 – 16 keV/q (El)
	Resolution ($\Delta E/E$)	12%	5% for 1.5-D, 7.5% for 3-D VDF	5.6%
	Analyzer constant (eV/V)	7	10.1	15.2
Angle	Range (AZ)	360°	-17.5 - +47.5° - EA	-33° - +63°
	Range (EL)	±45°	±22.5° - EA	± 18°
	Range scan (EL)	16 steps	9 steps	6 steps
	Angular Resolution (AZ × EL)	11.25° x 3° - 8°	< 2°	< 2°
	Pixel Field of view	11.25° x 3° - 8°	5° x 5°	6° x 6°
Temporal	Resolution – Normal mode	3s / 10 s	3 s	5 min
	Burst mode	0.125 s	1/10 s	30 s (heavy ions) 3 s (alphas)
Sensitivity	Per pixel (cm^2 sr eV/eV)	Variable, < 2.6 x 10^{-4}	4 x10^{-5}	Variable, <2 x 10^{-5}

Figure 46: Summary of the performances of the 3 SWA sensors.

10.2. EAS modelling in SPIS

Numerical simulations are the only mean to make a realistic and accurate quantitative model of the satellite induced perturbations on instrument measurements. Older SPIS developments have enabled the user to add scientific instruments (Langmuir probes, particle detectors, …) in the simulation domain as to mimic expected measurements.

EAS geometry and technical properties have been previously introduced. Its GMSH model used for SPIS simulations is presented in the following. It is based on a CAD model from Airbus comprising just the EAS sensor, the end of the boom and the boom-mounted baffle. This geometry has been adapted

to fit properly with our spacecraft configuration (inclusion of those new elements in the simulation volume, extension of the boom, mesh adaptation...).

For this type of detector, with particle entrance for each EAS sensor as a circular ring, it is necessary to consider each sensor entrance as the sum of several surfaces, in order to limit the curvature of each surface detector. Indeed, each of these surfaces is considered in SPIS model as a particle detector with a unique local detector basis (X_D, Y_D, Z_D) defined so as the Z_D axis is pointing into the detector, normal to the surface. This definition allows defining properly the acceptance angles for incoming particles in this basis. This is why each particle detector has to remain relatively "flat". The EAS instrument is thus composed in this model of 16 flat particle detector surfaces (8 by sensor), each one providing its own output dataset which will have to be combined to others for a global overview of EAS results. GMSH model of instrument generated for those simulation is presented on Figure 47, with acceptance angles illustrated for one particle detector. The following lines are extracted from the SPIS user manual to describe the configuration of general particle detectors, and especially the acceptance angles definition, before presenting our own configuration of EAS set of detectors.

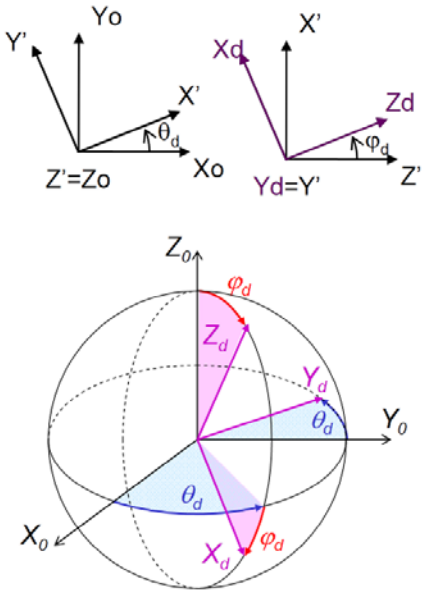

Figure 11 - Definition of the particle detector orientation

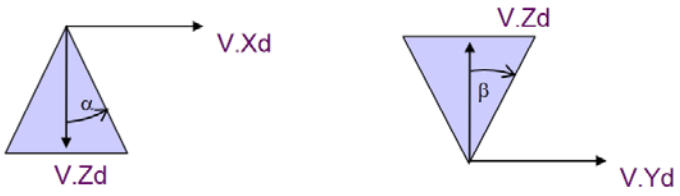

Figure 12 - Definition of acceptance angles

The main difficulty in using particle detectors is the correct definition of reference basis. Three basis are used:

- Gmsh SPIS natural basis (X, Y, Z) defining the spacecraft geometry coordinates.
- First particle detector basis (X_0, Y_0, Z_0) used to plot the results. This is useful to calculate the results of particle detectors in a reference frame adapted to the instrument, possibly different from the natural basis of SPIS, and possibly different from one instrument to another. The vector coordinates are defined in the GMSH basis used by SPIS for the CAD models.
  - *V1* is used as X_0
  - *V2* as Y_0
  - Z_0 is deduced from X_0 and Y_0 to form an orthogonal direct basis.
- A second particle detector basis used to define the orientation of the detector and the acceptance angles. This is useful to describe the aperture angles of instruments surfaces. Of course, instruments with different normal needs to define different basis when users want to define acceptance angles. The orientation of the detector (X_D, Y_D, Z_D) is defined by rotation in the (X_0, Y_0, Z_0) basis.
  - Rotation of θ_D around Z_0 to obtain the intermediary basis (X', Y', $Z' = Z_0$)
  - Rotation of φ_D around Y' to obtain the final basis (X_D, $Y_D = Y'$, Z_D)
  - The detector acceptance angles are defined in the local detector basis (X_D, Y_D, Z_D). The user defines two angles of acceptance $\pm\alpha$ and $\pm\beta$. Particles arriving within those limits are counted, others are discarded. Z_D is pointing inside the particle detector surface.

- $\pm\alpha$ around Z_D in the plane (X_D, Z_D)
- $\pm\beta$ around Z_D in the plane (Y_D, Z_D)

	Detector A (+Y)								Detector B (-Y)							
Det number	1//17//33	2//18//34	3//19//35	4//20//36	5//21//37	6//22//38	7//23//39	8//24//40	9//25//41	10//26//42	11//27//43	12//28//44	13//29//45	14//30//46	15//31//47	16//32//48
Alpha	0.392699082	0.392699082	0.392699082	0.392699082	0.392699082	0.392699082	0.392699082	0.392699082	0.392699082	0.392699082	0.392699082	0.392699082	0.392699082	0.392699082	0.392699082	0.392699082
Beta	0.785398163	0.785398163	0.785398163	0.785398163	0.785398163	0.785398163	0.785398163	0.785398163	0.785398163	0.785398163	0.785398163	0.785398163	0.785398163	0.785398163	0.785398163	0.785398163
Energy Slice	21//3//2	21//3//2	21//3//2	21//3//2	21//3//2	21//3//2	21//3//2	21//3//2	21//3//2	21//3//2	21//3//2	21//3//2	21//3//2	21//3//2	21//3//2	21//3//2
Phi	0.392699082	-0.392699082	-1.178097245	-1.963495408	-2.748893572	-3.534291735	-4.319689899	-5.105088062	0.392699082	-0.392699082	-1.178097245	-1.963495408	-2.748893572	-3.534291735	-4.319689899	-5.105088062
Theta	0.785398163	0.785398163	0.785398163	0.785398163	0.785398163	0.785398163	0.785398163	0.785398163	-0.785398163	-0.785398163	-0.785398163	-0.785398163	-0.785398163	-0.785398163	-0.785398163	-0.785398163
Mode	0	0	0	0	0	0	0	0	0	0	0	0	0	0	0	0
Octree	10000	10000	10000	10000	10000	10000	10000	10000	10000	10000	10000	10000	10000	10000	10000	10000
Nb_part	100000	100000	100000	100000	100000	100000	100000	100000	100000	100000	100000	100000	100000	100000	100000	100000
Origin X	-7.2919	-7.2919	-7.2919	-7.2919	-7.2919	-7.2919	-7.2919	-7.2919	-7.2919	-7.2919	-7.2919	-7.2919	-7.2919	-7.2919	-7.2919	-7.2919
Origin Y	0	0	0	0	0	0	0	0	0	0	0	0	0	0	0	0
Origin Z	0	0	0	0	0	0	0	0	0	0	0	0	0	0	0	0
Vect1 X	0	0	0	0	0	0	0	0	0	0	0	0	0	0	0	0
Vect1 Y	-1	-1	-1	-1	-1	-1	-1	-1	-1	-1	-1	-1	-1	-1	-1	-1
Vect1 Z	0	0	0	0	0	0	0	0	0	0	0	0	0	0	0	0
Vect2 X	-1	-1	-1	-1	-1	-1	-1	-1	-1	-1	-1	-1	-1	-1	-1	-1
Vect2 Y	0	0	0	0	0	0	0	0	0	0	0	0	0	0	0	0
Vect2 Z	0	0	0	0	0	0	0	0	0	0	0	0	0	0	0	0
Interac mode	0	0	0	0	0	0	0	0	0	0	0	0	0	0	0	0
E interv	200//300//300	200//300//300	200//300//300	200//300//300	200//300//300	200//300//300	200//300//300	200//300//300	200//300//300	200//300//300	200//300//300	200//300//300	200//300//300	200//300//300	200//300//300	200//300//300
Emax	200//30//30	200//30//30	200//30//30	200//30//30	200//30//30	200//30//30	200//30//30	200//30//30	200//30//30	200//30//30	200//30//30	200//30//30	200//30//30	200//30//30	200//30//30	200//30//30
Emin	0	0	0	0	0	0	0	0	0	0	0	0	0	0	0	0
Out level	1	1	1	1	1	1	1	1	1	1	1	1	1	1	1	1
Pop	ThE//PH//SEE	ThE//PH//SEE	ThE//PH//SEE	ThE//PH//SEE	ThE//PH//SEE	ThE//PH//SEE	ThE//PH//SEE	ThE//PH//SEE	ThE//PH//SEE	ThE//PH//SEE	ThE//PH//SEE	ThE//PH//SEE	ThE//PH//SEE	ThE//PH//SEE	ThE//PH//SEE	ThE//PH//SEE
Sample Per	1.00E-04	1.00E-04	1.00E-04	1.00E-04	1.00E-04	1.00E-04	1.00E-04	1.00E-04	1.00E-04	1.00E-04	1.00E-04	1.00E-04	1.00E-04	1.00E-04	1.00E-04	1.00E-04
Support ID	1	2	3	4	5	6	7	8	9	10	11	12	13	14	15	16
Traj Nb	20	20	20	20	20	20	20	20	20	20	20	20	20	20	20	20

The previous table details how the various numerical detectors composing EAS for SPIS have been configured. It required 48 files: 3 populations (thermal electrons, photoelectrons and SEE) times 16 particle detectors (2 sets of 8 surfaces par sensor). Rotation angles to define local reference basis for each detector and acceptance angles are also enumerated in the table.

For all cases presented here, the acceptance angles of each of the 16 detector surfaces are $\alpha = \pm \pi/8$ and $\beta = \pm \pi/4$. This way: two adjacent surfaces do not have the same "cone" of detection, but the combined field of views of all detectors cover the 4π sr of the environment, as in reality.

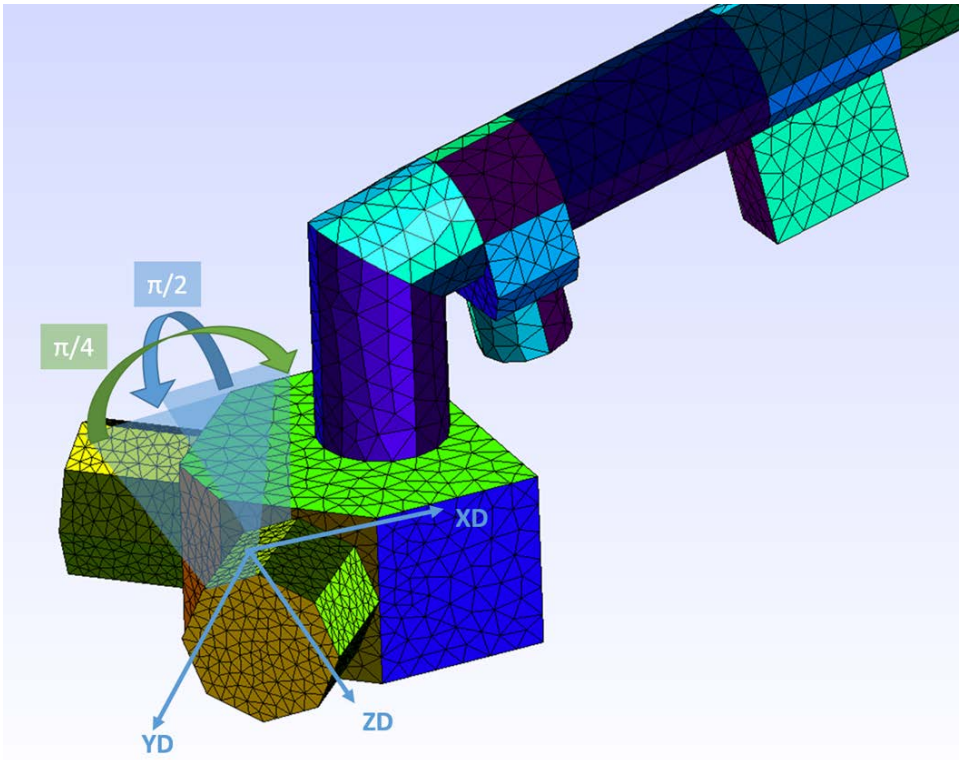

Figure 47: CAD model (made with GMSH software) of EAS instrument. Each of the two sensors is discretized into 8 flat surfaces, and corresponding acceptance angles are illustrated on this Figure.

As explained earlier, each of the 16 particle detectors will provide its own output files, which will have to be combined to other outputs in order to have a global understanding of EAS results: measured energy distribution function, incoming fluxes of particles, origin of spacecraft emitted particles detected…

10.3. Spacecraft configuration due to SPIS state

The Solar Orbiter model used for the following simulations is based on the previous recent geometry (as presented in Section 6.1), except that 3D modeling of RPW antennas has been necessary.

Indeed, this study allowed to discover a bug in the SPIS software, concerning particle detectors when a thin wire approximation is used in the SPIS-DUST branch of SPIS. The combination of both functionalities (particle detector and 1D wires) is responsible for this issue which is present since the beginning of development of SPIS-DUST functionalities and is only present in the DUST development branch. Even though it has no consequences on the use of particle detector when there is no wire (or on the wire collection without particle detectors), the present study using RPW antennas and EAS needed the combination of both functionalities. And when using a SPIS-DUST version or the last official SPIS version (where this branch is merged), it leads to a numerical core freeze at the first iteration. During

the expectation of the answer to this problematic discovery and the eventual bug correction we needed to go on with simulations and thus had no choice but using 3D modeling of antennas. This full 3D CAD model with its mandatory extremely refined meshing on the small radius antennas generates a much bigger amount of tetrahedra (more than 631000 elements instead of 309000 when considering 1D antennas), and thus much longer simulations. A patch has however been then delivered later on by ONERA but without verifications nor non-regression tests, and thus could not be safely used in that state for this ESA study.

However, as we are focused on EAS measurements, it is possible to apply a useful trick in order to gain CPU time of computation. Previous simulations on RPW charging were extremely long (few days of computation) as the objective was to determine the final electrostatic potentials on all spacecraft elements, especially on dielectric materials, which take longer time than conducting ones to reach equilibrium. Now, the aim is to know how EAS measurements will be affected by spacecraft generated fields, which we already estimated in the first part of this report for the RPW study. Thus, for the following simulations, potentials on all spacecraft surfaces can be set by user, according to earlier obtained values, and kept constant. As no circuit solver will be used during computations we obtain a gain of CPU time of simulation. Furthermore, there is no need now to compute plasma behavior for long durations. Few loops of calculations for particle generation and motion within the volume are enough to obtain stable plasma distributions and a well-established ion wake behind Solar Orbiter.

Unfortunately, particle backtracking for our 48 detectors remain heavy and time consuming. Even though potential computation on spacecraft is not necessary, simulations presented here lasted between 24 hours and 7 days (for the high-precision EAS measurement cases).

10.4. EAS Simulation configurations

Due to various difficulties encountered with the software when using magnetic fields applied over the computational volume, and the short schedule for providing complete EAS simulations which include particle measurements, it was necessary to dismiss cases with induced electric fields.

As the baffle option arose during this study, we performed three simulations, including for each case EAS measurements of thermal, secondary and photo-electrons. The first simulation named “EAS Reference case” represents the electrostatically neutral Solar Orbiter at 0.28 AU, without EAS baffle. It is the same latest satellite CAD model from the previous RPW cases presented in Section 6.5 (“RPW Reference case: no *B*, no I_{bias}, no Dielectrics in shadow”). But this time the CAD model includes 3D RPW antennas instead of thin wires, as explained in previous section. This “EAS Reference case” considers the same environment at 0.28 A.U. from the Sun, without any electromagnetic field applied over the volume. Every spacecraft surface element is here charged at 0V. EAS is thus supposed to observe an environment only disturbed by the physical presence of the satellite (which blocks the analyzer field of view when this one points towards directions around +*X* axis), and of course by local plasma density modifications such as the ones due to ion wake or SEE and photoelectrons over-densities.

The two other simulations are considering an electrostatically charged spacecraft, according to the charging level obtained with the RPW Reference case: “no *B*, no I_{bias}, no Dielectrics in shadow”, of Section 6.5. The second case is named “EAS no Baffle”, considering the same CAD model that “EAS Reference case”, and the third one, “EAS with Baffle”, logically includes this new EAS element. The environment used for all those three cases is described below:

- Ions: H+, PIC with Maxwellian distribution and drift,
- Electrons: PIC with Maxwellian velocity distribution function,
- Photoelectrons: PIC with Maxwellian velocity distribution function and with a characteristic temperature $k_B T_{ph}$ = 3 eV,
- Secondary Electrons under Electron impact (SEEE): PIC with Maxwellian velocity distribution function and with a characteristic temperature $k_B T$ SEEE = 2 eV, backscattered electrons with 2/3 of their initial energy,

- Secondary Electrons under Proton impact (SEEP): PIC with Maxwellian velocity distribution function and with a characteristic temperature k_BT SEEP = 2 eV,
- External boundary conditions: Fourier, 1/R2 decrease of potential

Environment parameters	Values at 0.28 AU from the Sun
Sun flux (# 1 AU)	12.76
Electron and Proton density (m^{-3})	1.04×10^8
Electron temperature (eV)	21
Proton temperature (eV)	27
Spacecraft velocity in X direction (m/s)	400000.0
Proton bulk velocity in Y direction (m/s)	-60000.0

11. EAS Reference case

Null potentials have been set on all spacecraft elements, including EAS surfaces, and kept constant in order to avoid too long simulations (see previous section 10.3).

11.1. EAS Reference Case: plasma state around the spacecraft

Plasma potential obtained for EAS Reference case is displayed on the following Figure 48.

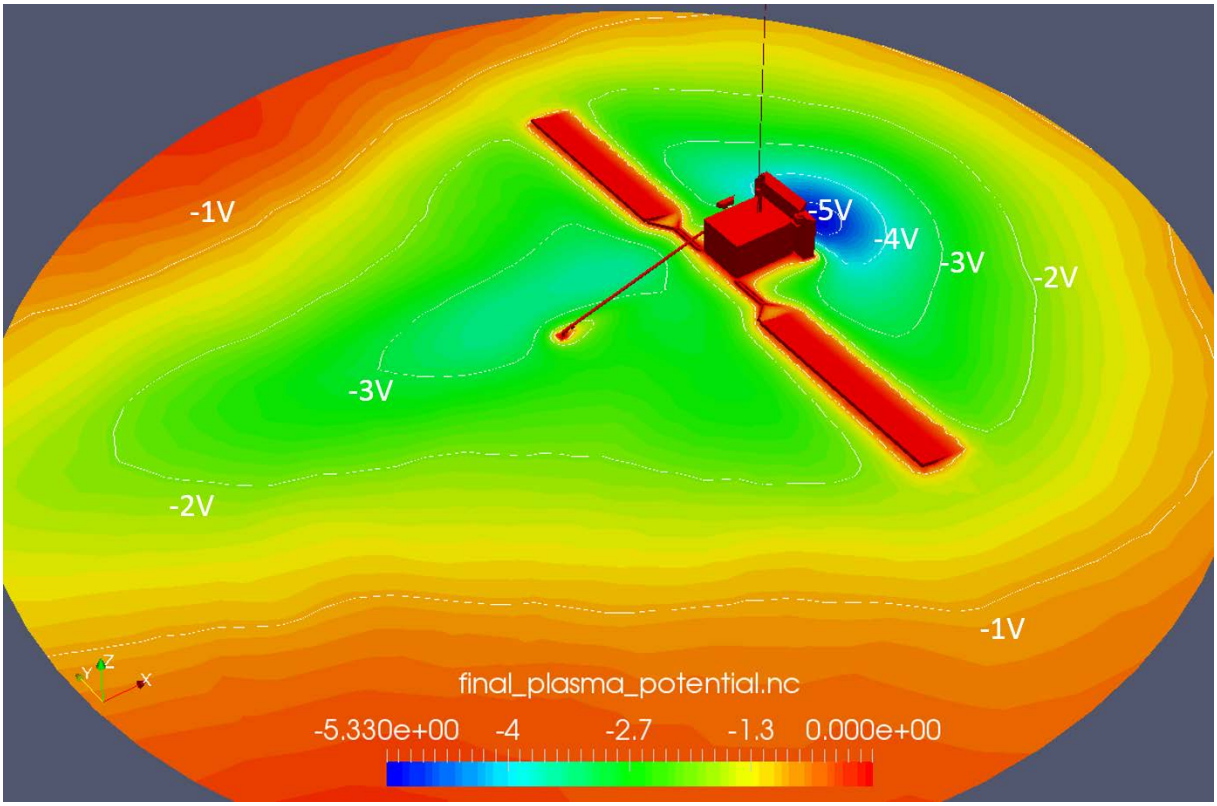

Figure 48: EAS Reference case - Plasma potential (V) around Solar Orbiter in the X-Y plane.

As for older cases, a negative potential region appears behind the spacecraft, due to the ion wake (as it is shown on Figure 49) and high densities of SEE (Figure 50). This region corresponds to a repulsive potential barrier for spacecraft emitted particles The same negative potential region appears in the ram, because of local high densities of secondary and photoelectrons (see Figure 50). What is

worrying is that those particles are well present around our electron instrument, at the end of the rear boom, and will definitely be recorded in the output data. But in what proportions?

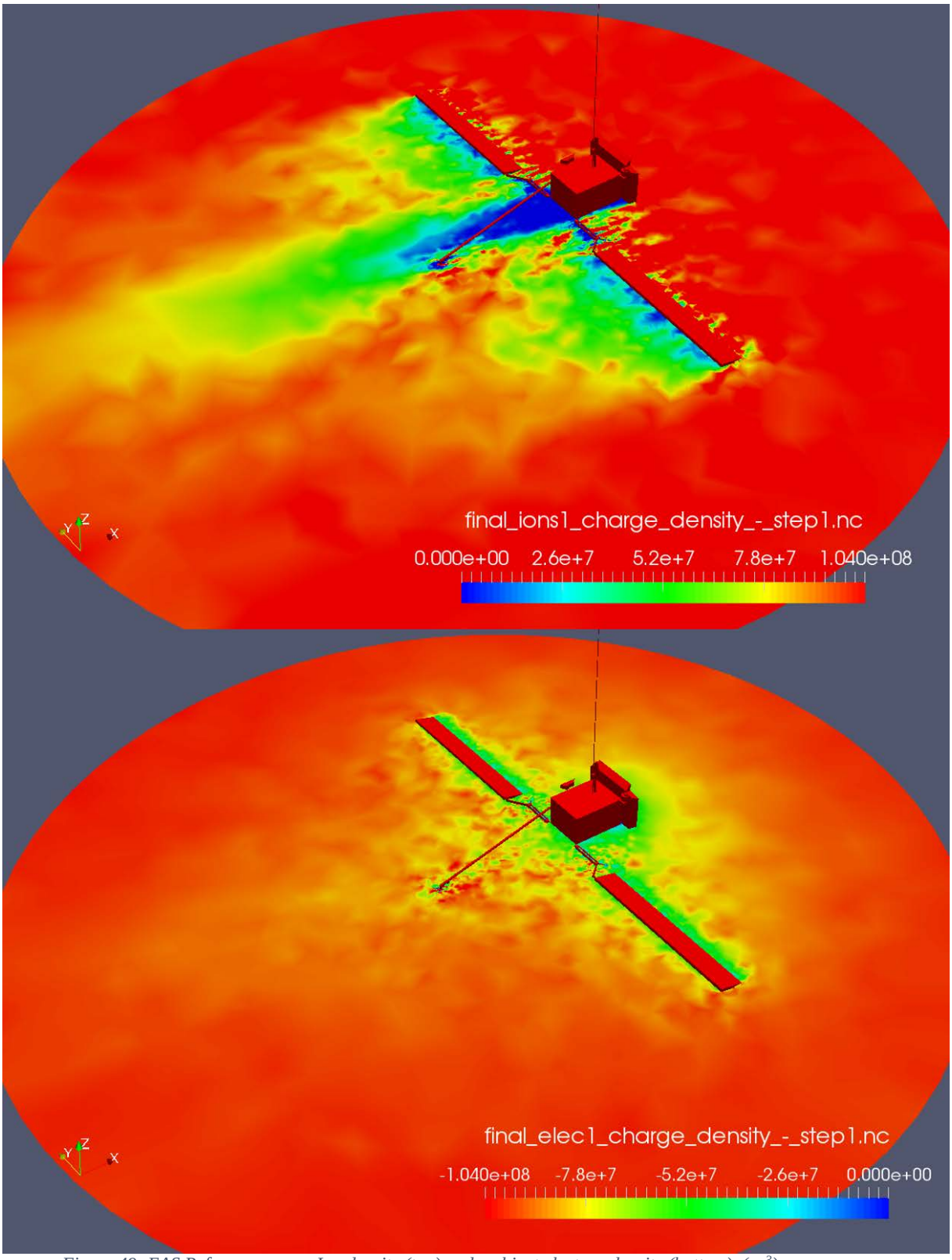

Figure 49: EAS Reference case – Ion density (top) and ambient electron density (bottom), (m^{-3}).

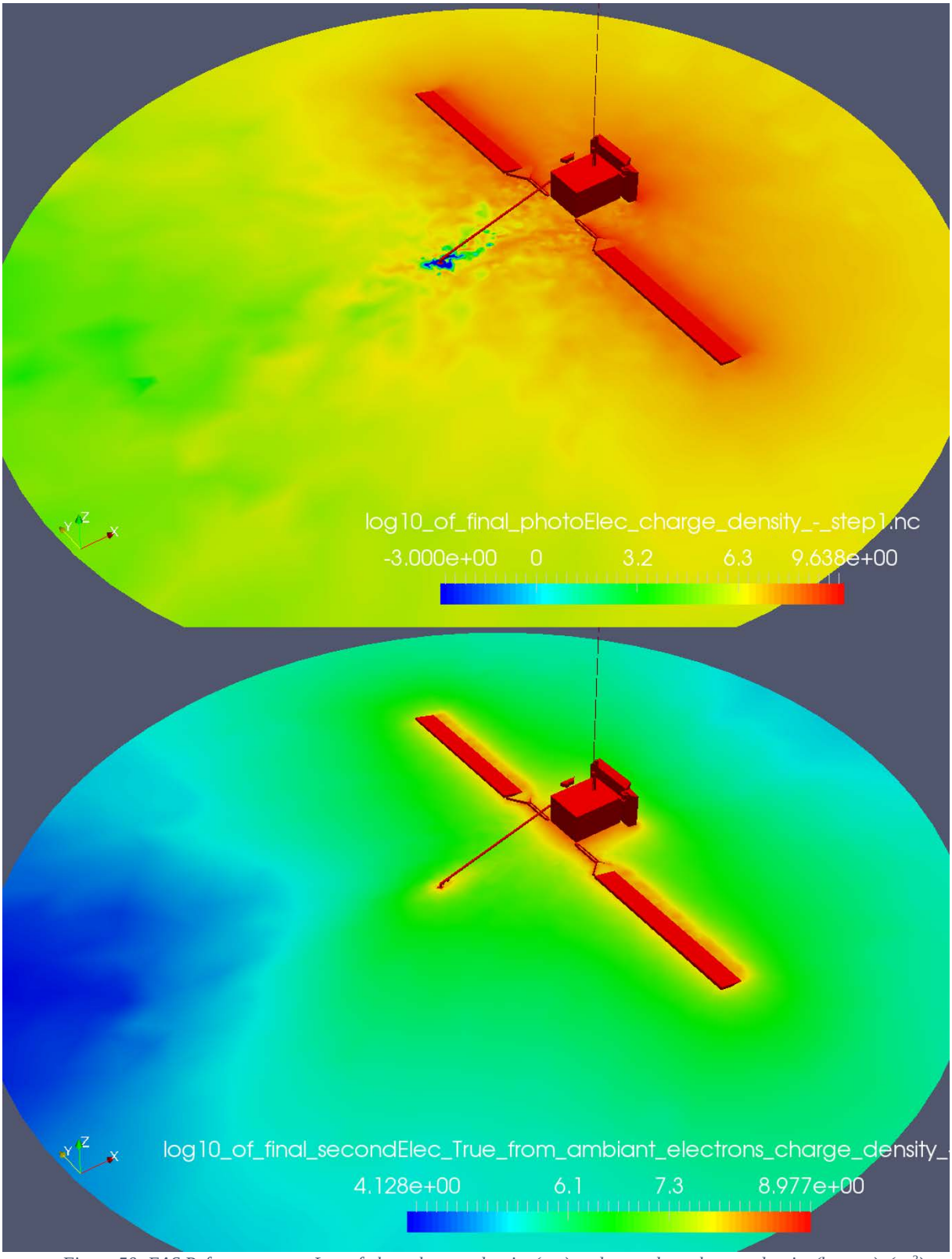

Figure 50: EAS Reference case - Log of photoelectron density (top) and secondary electron density (bottom), (m^{-3}).

11.2. EAS Reference Case: energy distribution functions measured by EAS

Most important outputs provided by particle detectors in general, and most revealing ones are the distribution functions of the scanned particles. In this situation with consideration of isotropic ambient electrons, the Maxwellian Energy Distribution Function $f_E(E)$ (or EDF) of particles arriving on detector D (charged at potential φ_D) is defined as:

$$f_E(E) = \frac{4\pi V_D}{m} f_D(V_D) = \frac{4\pi V_D}{m} n_0 \left(\frac{m}{2\pi kT}\right)^{3/2} exp\left(\frac{-m{V_D}^2}{2kT}\right) exp\left(\frac{-q\varphi_D}{kT}\right)$$

In this equation for the considered particle population: $f_D(D)$ is the velocity distribution function, V_D the velocity, k the Boltzmann constant, T the characteristic temperature, m the mass and q the charge.

The $f_E(E)$ files are directly provided by SPIS for each particle detector. We thus obtain 16 files for each electron population (ambient, SEE and photoelectrons). For each particle type, those 16 files have to be "assembled" in order to rediscover the entire EAS vision of its environment. But, the simple addition of the EDF obtained by the 16 detecting surfaces would be a mistake, as explained in the following.

➢ EAS Field of view

Considering the two sensors configuration, some regions of the 4π sr of the environment are scanned by only one single analyzer (the $+Y$ or $-Y$ sensor), while other regions are looked by both analyzers ($+Y$ and $-Y$ sensor).

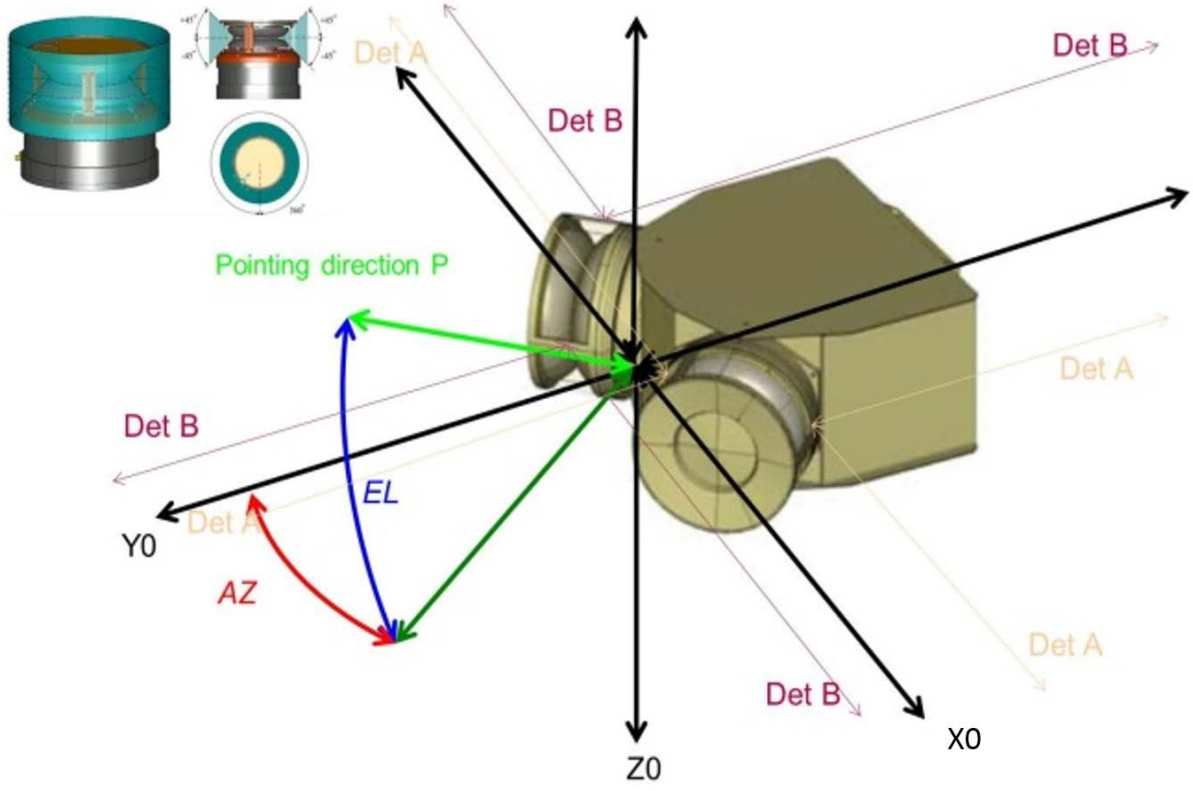

Figure 51: EAS outputs reference basis (X_0, Y_0, Z_0): description of Azimuth (AZ) and Elevation (EL) angles.

To illustrate this phenomena, we need to take into account the EAS field of view regarding its surrounding environment. Let's thus go back to Section 10.2, where the instrument reference frame (X_0, Y_0, Z_0) for SPIS has been introduced. In our cases, and for easier reference frame rotations - necessary to define local particle frames (X_D, Y_D, Z_D) – we chose to set $X_0 = -Y$, $Y_0 = -X$ and $Z_0 = -Z$, where (X, Y, Z) is the GMSH frame. Starting from this new reference frame we can define our own EAS field of view thanks to two specific angles: Azimuth (AZ) and Elevation (EL) in degrees, which allow to define a pointing direction of EAS, as illustrated on Figure 51. This way: AZ is defined between 0° and 360°, EL between -90° and +90°. For instance:

- EL = AZ = 0: Wake direction
- EL = 0, AZ = 180: rear SC direction
- EL = +90: +Z direction
- EL = -90: -Z direction

This pointing direction can also be seen as the opposite of the arrival direction of a detected electron, seen by EAS. According to the sensor annular ring discretization necessary for particle detector modelling (see Section 10.2), and the acceptance angles defined for each particle detector (angles α and β, also in that Section), we can have a closer look to each EAS sensor field of view (FOV). Next Figure 52 illustrates particle detectors FOV layout only for the four upper collecting surfaces, but they are simply rotated for the rest of them.

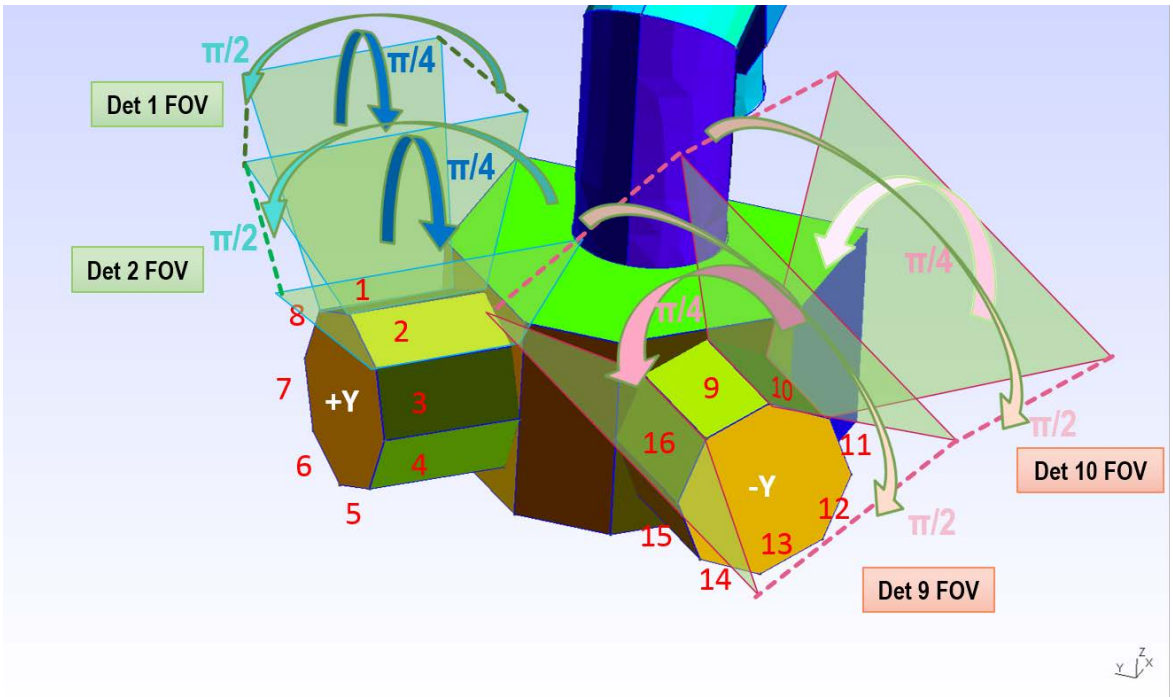

Figure 52: EAS sensors discretization into 16 particle detectors (red number identification), and FOV for detectors 1, 2, 9 and 10, corresponding to α and β angles. Those FOV have not been represented for all 16 detectors to avoid an unreadable Figure.

By "FOV", we mean that any electron arriving on a particle detector, and having its velocity vector enclosed in the cone of sight of this detector surface (cone defined by α and β), will be counted by this surface and measured as a valid detection. This reasoning introduced by previous Figure 52 can be extended to farther distances in order to reach the external boundary of the plasma computational volume (which is a sphere in this study). As SPIS particle detectors collect electrons through

backtracking processes, they are emitted from those instrument surfaces and then propagated into the volume. If electrons reach the external boundary, they are considered as valid and thus acquired by EAS. Here each of the 16 particle detector sees one specific area of the external boundary. The field of view of each sensor (±*Y*), for each particle detector, has to be projected over the spherical boundary of the computational volume. This situation is illustrated on the following Figure 53, where the right sketch shows the combined projected FOV of EAS on the boundary (EAS is at the center of this sphere). Each FOV projection logically looks like a curved rectangle. Note that Figures presented since Figure 53 are illustrative sketches and remain approximations. Indeed, in our SPIS used GMSH model, EAS is not exactly at the middle of the spherical volume, but ~1.3 m behind in the -*X* direction: it means that FOV projected areas on the -*X* side of the boundary should be a little bit smaller than the ones projected on the +*X* side, which does not appear on those Figures. Time was missing for finding out a proper way of projecting all FOV on a shifted sphere with GMSH. However, we estimate that this difference remains small and negligible. Furthermore, for better visibility we also neglected on those illustrations the ~20 cm gap between the two sensors (±*Y*). A test, not presented in this report, showed that the discrepancy of FOV configuration linked to this small distance gap is almost invisible.

Referring to the previous nomenclature for our AZ and EL angles, Figure 53 shows that for the entire AZ range (from 0 to 360°) and EL included between +45 and -45°: sensors +*Y* and -*Y* have "practically" distinct pointed regions that can thus be added all together to recover this "central strip" of the simulation boundary. This concerns FOV of detectors 3, 4, 7 and 8 of sensor +*Y*, and 11, 12, 15, 16 of sensor -*Y*. We indicated "practically", as borders of pointed regions do slightly overlap when changing the sensor source of observation. This appears more clearly on Figure 54, with a focus on zero Elevation area on the left sketch, when the observer is looking towards the +*X* axis (or the -Y_0 axis). But the common areas of visibility remain small. Here it can be approximated that, for simplification reasons, those detectors (3, 4, 7, 8, 11, 12, 15, 16) have distinct sights and consequently that the fluxes of particles collected by them can be simply added. Corresponding Energy Distribution Functions measured by those detectors can thus also be added, in order to cover that strip of view (AZ = 0 – 360 ° for EL = -45 - +45°).

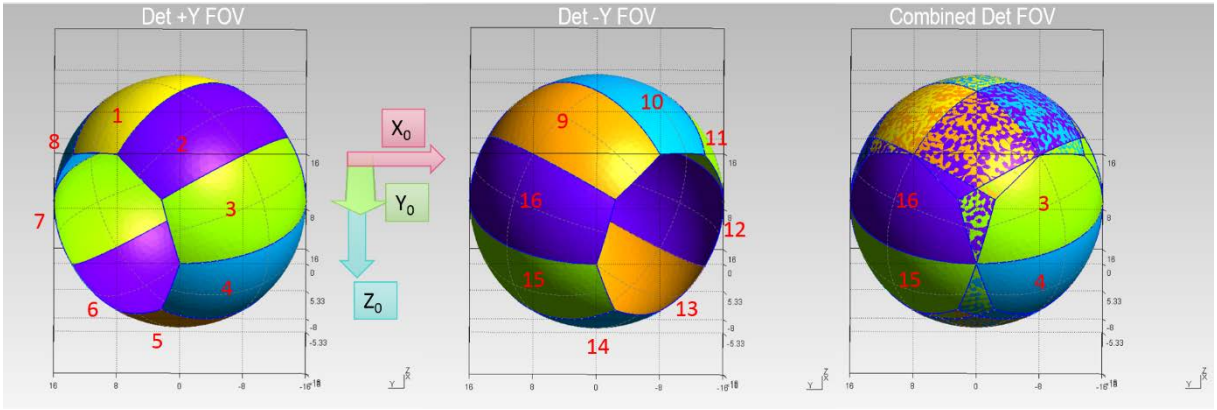

Figure 53: EAS FOV per sensors with same camera orientation for all sketches. FOV are projected over the spherical boundary of the computational volume. Red numbers identify the corresponding detector number to its field of view. The right sketch shows the combination of Sensor +Y (left) and -Y (center).

Now, it also appears on Figures 53 and 54 that for pointing directions with elevations between 45 and 90°, as for those with EL between -45 and -90°, this scenario cannot be applied. Indeed, each pole of the spherical simulation volume (which are for any AZ: EL > 45°, and EL < -45°) is covered by both sensors. More specifically detectors 1,2 (from +*Y* sensor) and 9, 10 (from -*Y*), point towards a curved square which normal is +*Z* direction (or -Z_0): the equivalent of the "north" pole area. In the same way: 5,6 (+*Y*) and 13, 14 (-*Y*) do see the "south pole". This configuration also means that adjacent detectors 1 and 2 from +*Y* sensor "perfectly" cover the combined FOV also seen by the coupled detectors 9 and 10 from the -*Y* sensor. Unlike the previous case we here assume that this overlapping is total, despite

small isolated covered areas as they appear on right sketches of Figures 53 and 54, inherent to EAS modelling. Finally, for the pole regions (any value of AZ, EL > 45°, and EL < -45°) the detected fluxes of electrons have to be averaged. This concerns detectors 1 and 2, which summed EDF has to be averaged with the EDF sum of detectors 9 and 10, and in the same manner the sum of EDF from 5 and 6 has to be averaged with 13 and 14.

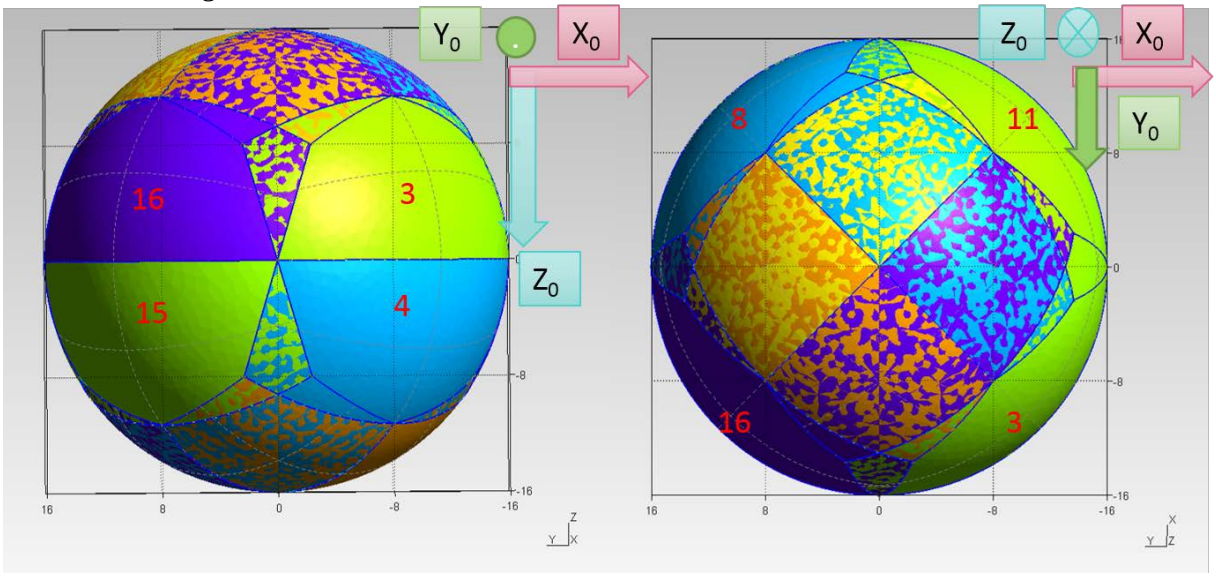

Figure 54: EAS combined FOV projected over the simulation spherical boundary. Focus on the zero EL region (looking towards the +X axis) on the left, and on the high elevation region at +90° on the right (looking towards -Z axis).

An example of the "north" pole situation is given on Figure 55, showing the good overlapping of FOV curved rectangles from sets of detectors (1,2) and (9,10). Those rectangles (from +*Y* sensor) are simply rotated by π/2 with respect to others (from -*Y* sensor). The cumulated density of current for those four detectors is displayed on Figure 56, and the corresponding values of the current density at its boundary origin show that the simple addition of those fluxes is erroneous: it would lead to an artificially doubled flow of particle current coming from the pole regions. EDF corresponding to those pointing directions (around +/- *Z* direction) have to be processed with this consideration.

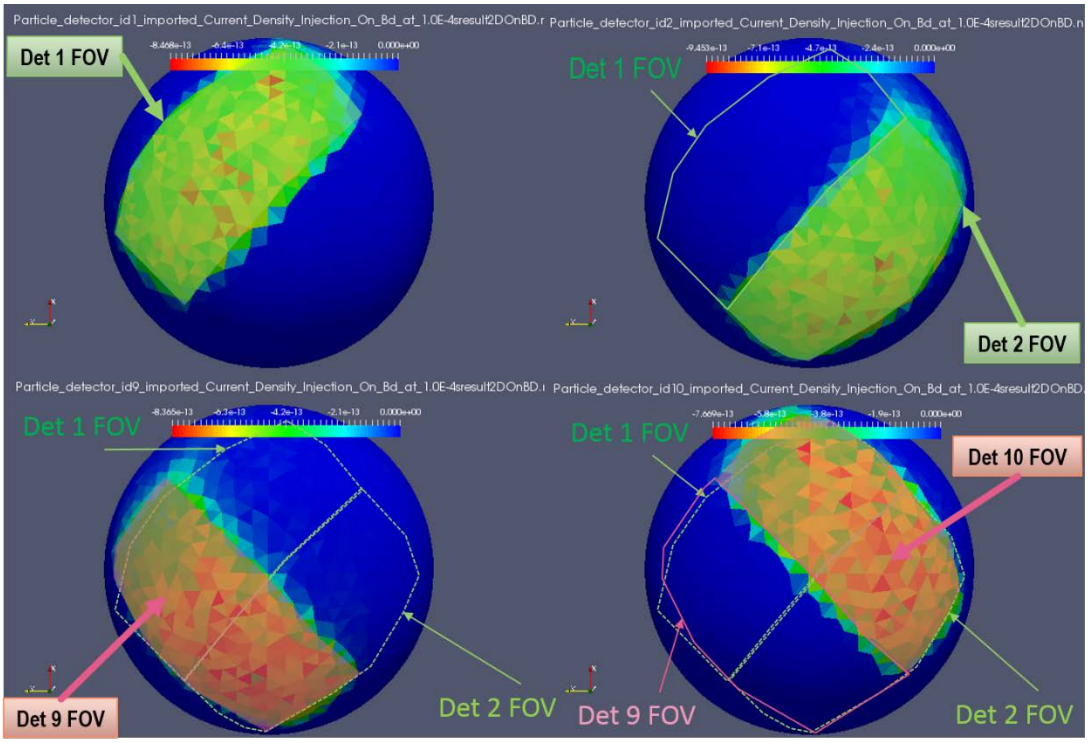

Figure 55: Example of the "north pole" visibility by particle detectors 1, 2, 9, 10. The color scale indicates the current density of ambient electrons detected by each particle detector, at its origin on the boundary of the computational volume.

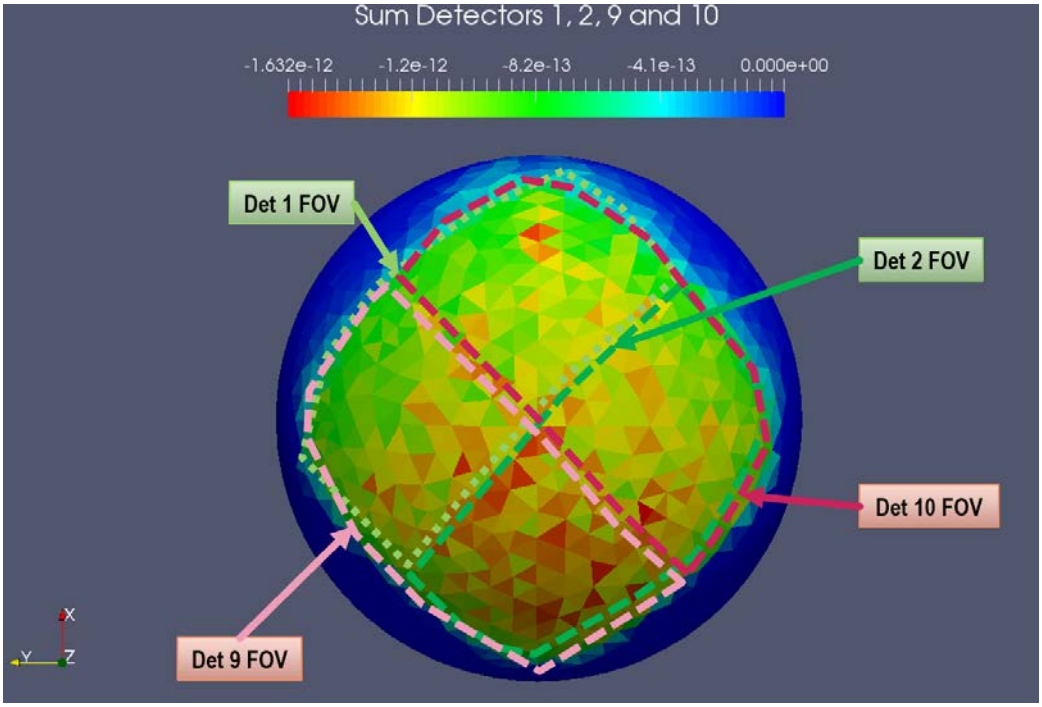

Figure 56: Example of the "north pole" visibility by particle detectors 1, 2, 9, 10. The color scale indicates the sum of current density of ambient electrons detected by those detectors, at their origin on the boundary of the computational volume.

➢ EAS Reference Case: measured EDF

According to the previous reasoning from Section above, we can obtain the global EDF of EAS measured electrons by cumulating all detector EDF per population as follow:

$$f_E(E)_{Total} = f_E(E)_3 + f_E(E)_4 + f_E(E)_7 + f_E(E)_8 + f_E(E)_{11} + f_E(E)_{12} + f_E(E)_{15} + f_E(E)_{16} + {}^1/_2\,(f_E(E)_1 + f_E(E)_2 + f_E(E)_9 + f_E(E)_{10}) + {}^1/_2\,(f_E(E)_5 + f_E(E)_6 + f_E(E)_{13} + f_E(E)_{14})$$

The corresponding result for ambient electrons EDF is plotted on the following Figure 57. On this Figure, the gray curve represents the analytical distribution function actually injected by SPIS into the computational volume. It is the undisturbed pure population that scientist would like to directly measure if there weren't any biases on and around the instrument, due to the various spacecraft/plasma interactions. The orange curve stands for the ambient electron population that EAS should have theoretically measured, considering only its potential φ_D, and the instrument alone in the volume, according to Liouville's theorem (see Section 11.2). As here it is a null surface potential: this curve effectively corresponds to the gray one. Finally, the blue curve is the desired EDF of ambient electrons reconstructed thanks to EAS measurements, using the previous equation of EDF combination.

We notice the reduction of this function regarding the others. Indeed, even though the spacecraft and its instrument are maintained at 0V, the surrounding plasma presents negative potential regions (see Figure 48), which represent electrostatic blockades for incoming electrons. Furthermore, spacecraft body itself remains a physical obstacle to particle detection towards some pointing regions.

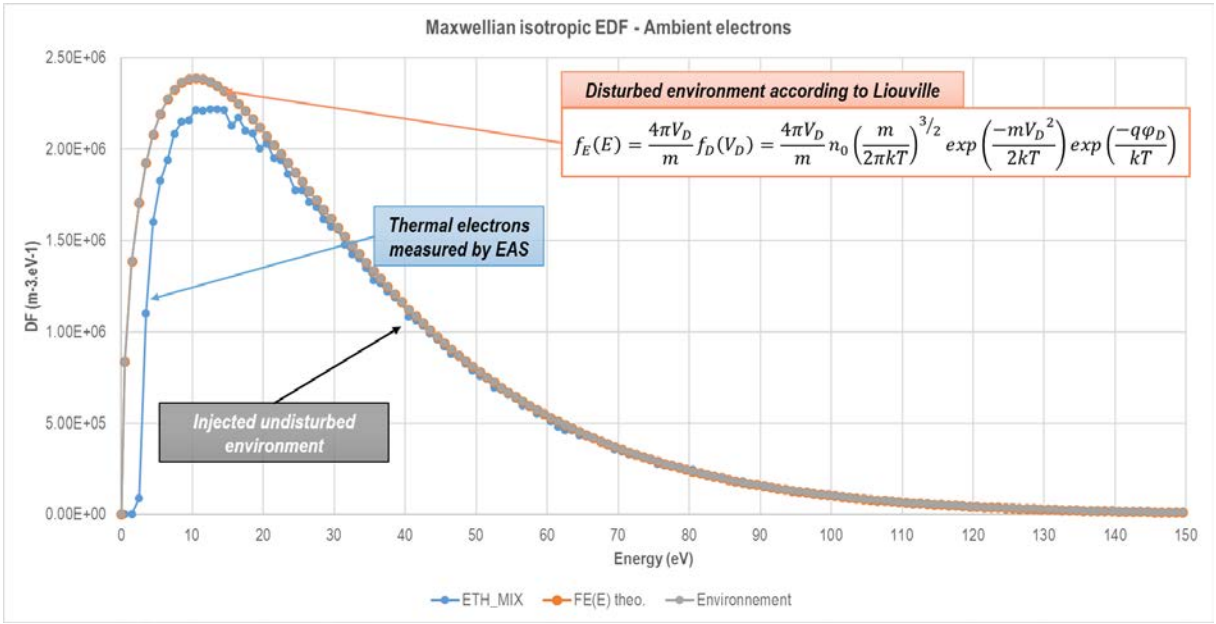

Figure 57: EAS Reference case -EDF of thermal electrons. Gray curve: analytical distribution function injected by SPIS into the computational volume, orange: ambient electron population theoretically measured, considering only the potential φ_D of the detector alone in the volume, blue: effective EDF of ambient electrons measured by EAS (taking into account the previous equation for EDF reconstruction).

In practice, Electron Analyzer System collects all electrons, whatever their origin. Thus output data present a mix of ambient, secondary and photoelectrons, even though scientists know that high fluxes of low energy electrons appearing in the detected spectrum can be usually identified as spacecraft emitted electrons. Thanks to SPIS it is possible to distinguish any detected electron as every particle

type is followed by the software as an independent population. Thus, it can provide EDF for secondary and photoelectrons independently, as illustrated on Figure 58.

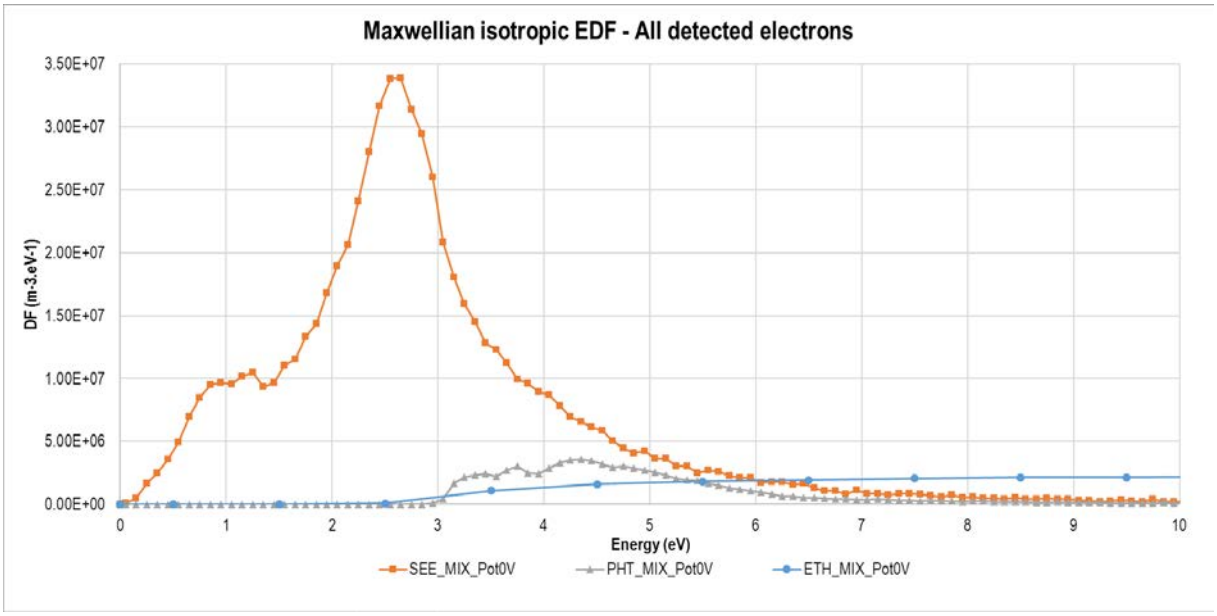

Figure 58: EAS Reference case -EDF of all electrons, detected by EAS. Blue curve represents ambient electrons, gray curve the photoelectrons and the orange one the SEE.

This Figure shows how low energy ranges, below 6 eV, are highly polluted by secondary electrons, especially around 2.7 eV with a higher EDF value. This energy level corresponds to the surrounding plasma potential area (from ~ -3 to -2 V) in the vicinity of the instrument, where secondary electrons are repelled after their emission and might thus be redirected towards the sensors.

Integrating those EDF allow to recover the respective measured densities. For this EAS reference case we thus obtain:

- $N_0 = N_{theo} = 1.04\times10^8$ m^{-3}, injected environment of ambient electrons and expected density measurement for EAS alone in the plasma and charged at 0 V,
- $N_{ThE\_meas} = 9.44\times10^7$ m^{-3}, actual measurement of ambient electron density in these simulation conditions,
- $N_{SEE} = 6.96\times10^7$ m^{-3}, secondary electron density measured by EAS,
- $N_{Ph} = 8.48\times10^6$ m^{-3}, photoelectron density measured by EAS.

Finally, the ambient electron density measured in those conditions (N_{ThE_meas}) is 8.55 % inferior to the expected one, because of negative plasma potential regions around the instrument and SC body obstacle to particle detection. If we include parasite electrons to this calculation: the total electron density measured reaches 1.73×10^8 m^{-3}, which is an increase of 67.1 % regarding the undisturbed environment. This excess of detection is a usual phenomenon encountered when dealing with low energy plasma measurements by onboard detectors. However, thanks to SPIS simulations and as demonstrated here, it is possible to clearly identify the necessary low-energy cut-off limit for EDF curve integration, in order to compute the various “cleaned” moments related to EAS data. Note that it is also possible to recover the measured average kinetic energy of all detected electrons, but that was not performed in this study because of time limitations.

11.3. EAS Reference Case: advanced post-processed outputs provided by EAS numerical instrument

As EAS is modeled as a combination of several particle detector surfaces, the user interest is to get the global interpretation of this instrument data, combining all FOV and outputs to recover the expected measurement of the environment. In the following we will try to place ourselves at EAS location, with its own point of view and vision of the surrounding plasma. In this perspective: it is required to use our own reference frame, already described on Figure 51, considering each pointing direction of the instrument by defining the AZ and EL angles. The question is: what does EAS see when it looks towards various pointing directions?

SPIS can provide, per particle detector, sorts of 2D maps, plotting slices of velocity (or flux) distribution functions, at one user-defined energy level and in spherical coordinates. Each map has to be asked by user before or during the simulation process. It means that post-processing analysis might be limited if users did not anticipate their needs before the end of simulation. Furthermore, those maps are provided per particle detector and cannot be easily cumulated or mixed in order to get the total view of our EAS instrument.

However, SPIS provides an extremely useful and complete output file named "*spis.Util.Instrument.ParticleDetectorY_Particle_List_at_t=XXXXs.txt*" (*Y* is the particle detector ID and *X* the time of measurement, those parameters depend of course of each simulation). It is the list of all detected particles (of one population) by each detector in the output frame (X_0, Y_0, Z_0). There is one line per particle with successively the position on the detector (x_D, y_D, z_D), the velocity on the detector (vx_D, vy_D, vz_D), the flux weight of the particle on the detector (wF_D), the position on the particle source (x_E, y_E, z_E), the velocity on the particle source (vx_E, vy_E, vz_E), the flux weight of the particle on the particle source (wF_E) and the statistical weight of the particle in volume (w) which is conserved in Liouville's theorem. Therefore, those files can be post-processed at user convenience: for instance, in our case, it is possible to convert the Cartesian coordinates of each incoming particle on the detector (vx_D, vy_D, vz_D) into an incoming energy and direction (AZ, EL). Particles detected can thus also be filtered depending on their energy, weight, origin region, deflection angle (*i.e.* angle made by velocity vector at injection on the boundary of the computational volume with this vector at detection on one particle detector surface), *etc*.

Those post-processed outputs provide key information regarding the instrument field of view and help answer questions such as: where are the physical or electrostatic obstacles to electron detection and what are the consecutive impacts on measurements? From which direction does come the highest/lowest particle flux? What are the sources of secondary and/or photoelectron pollution? And many others.

As explained above, the present EAS configuration is made of 16 collecting sections so the results for all detectors have to be cumulated into one single map and with the same reference basis, in order to allow the global understanding of measurements. In this perspective an extended post-processing method of those *Particle List* output files, including a local basis transformation, have been generated to compute the hereafter presented results. This work is performed outside the SPIS framework, using a computation routine made with the *Scilab* software and providing the desired 2D data tables. This method can also be applied to all types of particles.

➢ EAS Reference Case: Pointing maps

As explained in the previous Section, it is possible thanks to our post-processing routine to present 2D maps of EAS field of view itself. Those maps can display, depending on any pointing direction of the instrument (defined by AZ and EL angles, see illustration below) a specific parameter related to a specific plasma population scanned by the sensors. An example is provided below on Figure 59, with here: the *flux* of *ambient electrons* (with *energies* at *detection between 10 and 20 eV*), cumulated by solid angle of *5°×5°* in (AZ, EL), and only for *one* particle detector(s). Note that all *italic* parameters in

the previous sentence can be changed by user if necessary: for instance, representing the *deflection* of incoming *secondary electrons* from *0* to *5* eV, as seen by *all* particle detectors, with a *2°×2°* angular resolution…

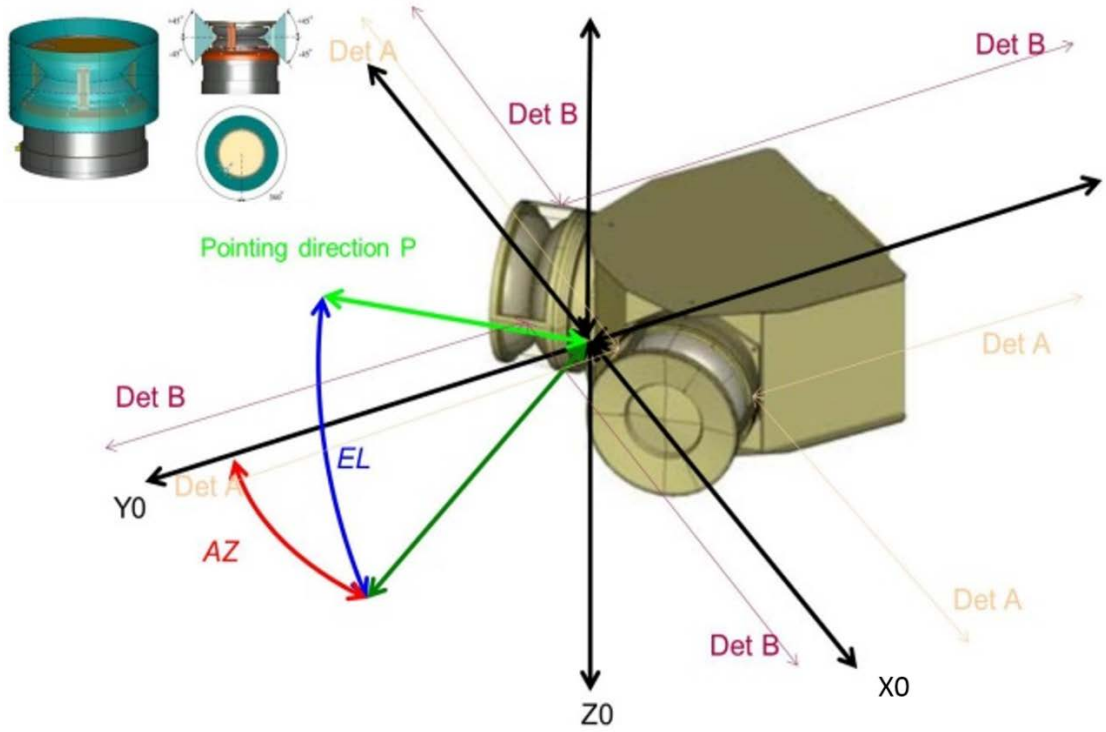

Illustrative sketch of pointing direction definition for EAS, with Azimuth (AZ) and Elevation (EL) angles: AZ from 0 to 360° and EL between -90 and +90°.

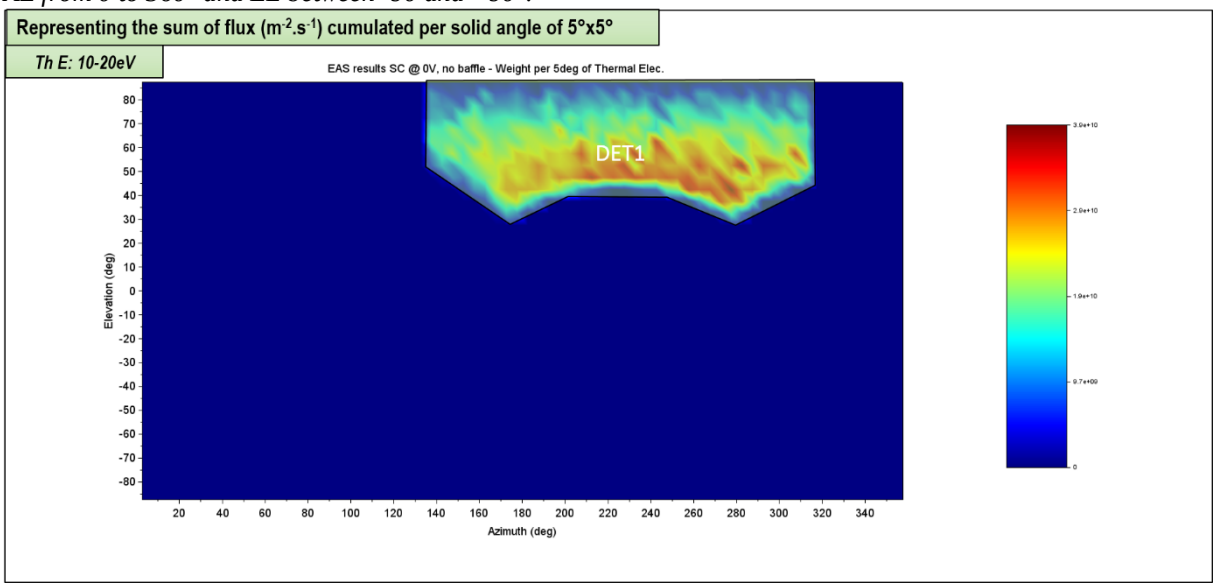

Figure 59: EAS Reference case – Pointing map of EAS for ambient electrons flux, FOV of single Particle Detector 1.

Figure 59 above displays in EAS FOV the part of incoming thermal electrons (from 10 to 20 eV), observed only by the 1st particle detector forming the instrument sight. This has been computed asking our routine to process only the 1st file *Particle List* provided by this specific surface. It allows to delimit

the FOV of this specific particle detector, and confirms our previous estimations represented on Figure 52, 53 and 54. We overprinted on this flux trace the corresponding FOV for this detector with the transparent green shape. Note that depending on detected particle trajectories, which might be more or less curved, the limit pointing directions can be over- (or under-) estimated. This specific energy range (from 10 to 20 eV) has been selected according to the previous total EDF result (Figure 57), which showed that this eV array contained the most numerous particle detections. Other ranges can obviously be chosen, or narrower…

Using the same method, we can run our script for every other particle detector alone and thus overprint all corresponding FOV shapes. The cumulated results have been regrouped on the same map below in order to compare and identify each sensor sight and the already detailed overlapping regions.

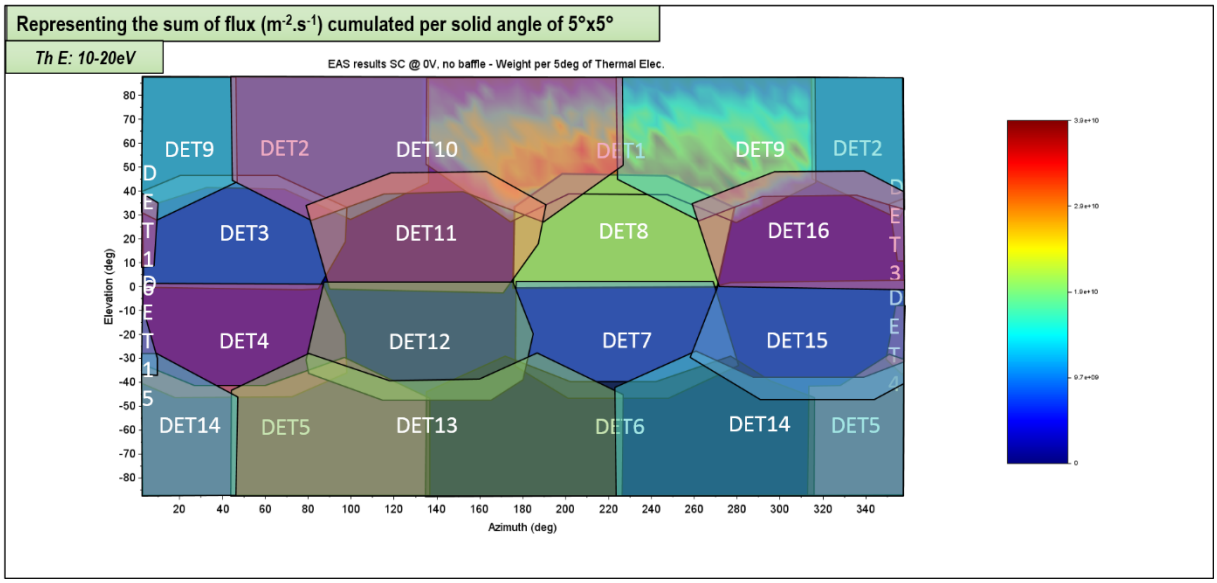

Figure 60: EAS Reference case – Pointing map of EAS for ambient electrons flux, FOV of all Particle Detectors.

This above map shows how difficult it will be to process the results in order to: add the fluxes when FOV are complementary, and average them for the limited and specific common pointing regions. Previously (Section 11.2), we simplified this problem stating that for Elevations between -45° and +45° results of measured EDF can be added and above those limits, averaged. But here in the context of fluxes, deflections… we prefer to present raw data outputs: as those particles are really seen by the EAS instrument. The two previous maps help keeping in mind that various artefacts can appear from some specific pointed regions, as flux increases for instance, and that those artificial effects are simply due to common FOV between several detectors.

The final results for this category of ambient electrons is displayed on the following Figure 61, cumulating the outputs of all the 16 particle detectors. We notice several important facts on this Figure:

- the artificial flux increases towards the specific common pointing regions: the flux is nearly doubled,
- the decreasing flux at high Elevation levels (±80 to 90°): due to our reference frame configuration. Indeed, when pointing to high absolute values of EZ, whatever the AZ value: EAS points practically towards the same single direction, and sees through a narrow cone around the +*Z* axis. This is why the flux is there limited,
- the Solar Orbiter body trace is clearly visible on the map, so as the solar arrays and HGA effects on flux losses. Those physical elements are direct physical obstacles to electron detections towards those directions, as those particles cannot get through its structure. Few electrons which seem to arrive from those pointing directions have in reality been

deflected by electrostatically charged regions in the vicinity of EAS. The estimated spacecraft body limits have been represented with white drawing on the map,

- the two spots of flux losses at null EL value and AZ = 90 and 270° are simply the consequence of each EAS sensor pointing towards the other. Practically no ambient electron had the sufficient trajectory to ingratiate itself in those small cones of sight, with those specific orientations of velocity vectors.

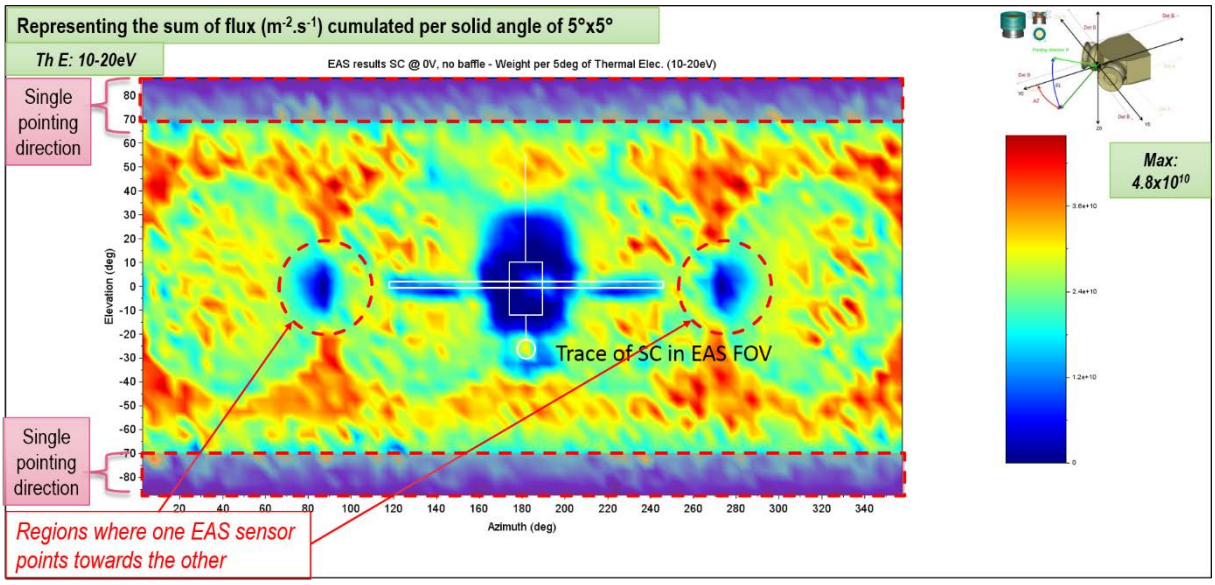

Figure 61: EAS Reference case – Pointing map of EAS for ambient electrons flux, cumulated for all Particle Detectors.

Let's focus now on another possible parameter that our computation method allows to represent on this kind of maps: the deflection angle (*i.e.* angle made by velocity vectors at injection on the boundary of the computational volume with this vector at detection on one particle detector surface). High angles of deflection mean that incoming particles have been importantly curved during their path from external boundary until their detection on one EAS collecting surface. This output map is averaged by FOV bins of $5°\times5°$ in (AZ, EL), taking into account the weight (wF_D) of each particle.

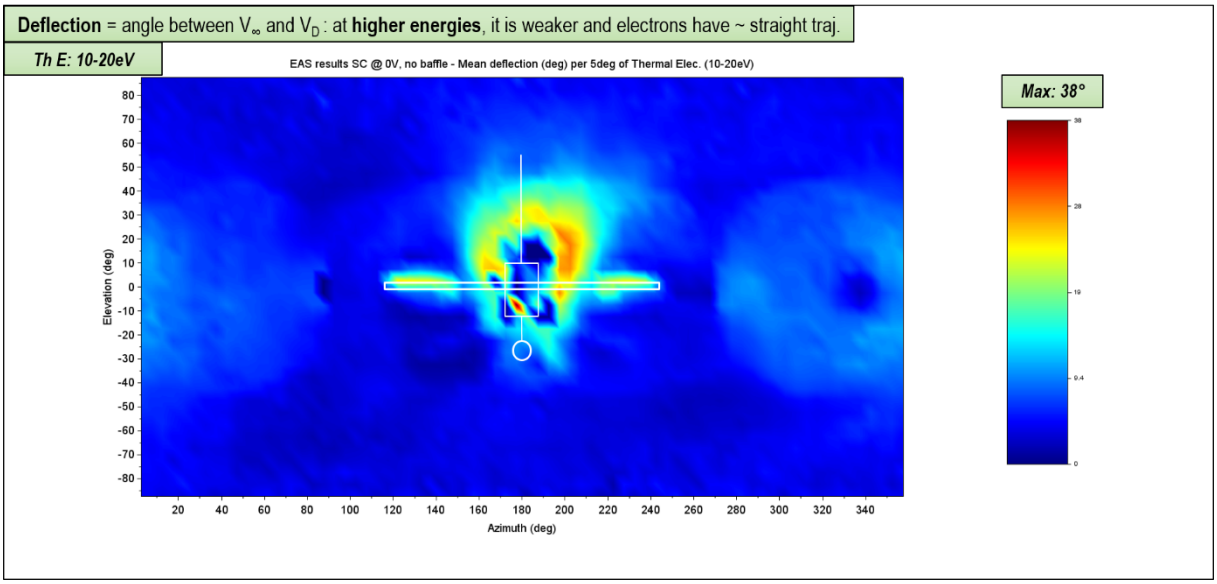

Figure 62: EAS Reference case – Pointing map of EAS for ambient electrons deflection angle.

Above Figure 62 conveys the fact that particles which seem to come directly from the spacecraft body have actually been deflected (we did not represent outputs for spacecraft emitted particles yet). We remind the absence of electrostatic effects directly attributable to Solar Orbiter charging as in this reference case all SC elements are set to a constant 0 V level. But, as it appears on previous Figures 48 and 50, plasma behavior (ion depletion in the wake and strong local densities of secondary and photoelectrons) did modify electrostatic levels around the satellite and thus inflected electron trajectories. This also appears when pointing towards null Elevations and Azimuth between (0 to 90°) and (270 to 360°): the negative potential region surrounding the instrument (see Figure 48) impacts local electron paths, especially at this low energy considered (10-20 eV).

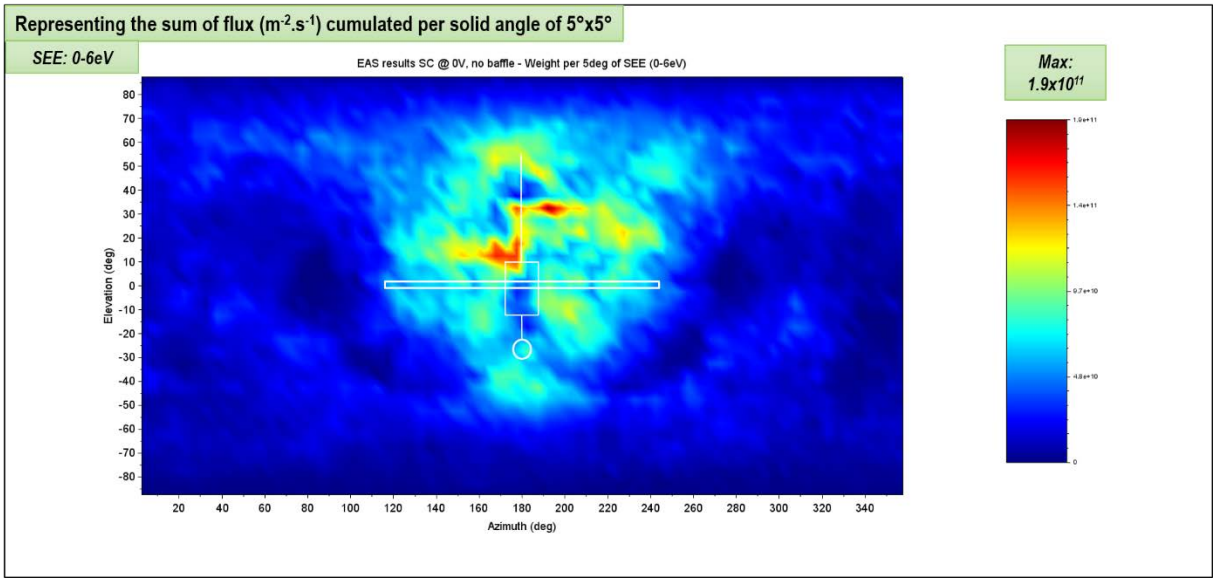

Figure 63: EAS Reference case – Pointing map of EAS for SEE flux.

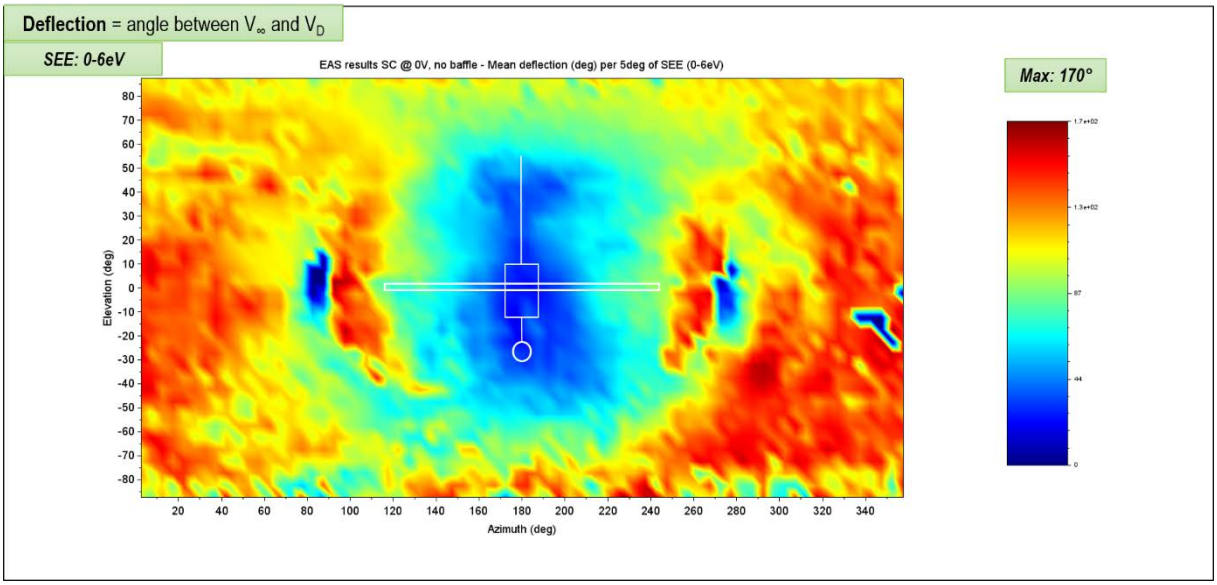

Figure 64: EAS Reference case – Pointing map of EAS for SEE deflection angles

Finally, when representing those 2D Pointing maps, we can use other particle populations for inputs, such as the secondary electrons. Their flux and deflection maps are displayed above, and according to their EDF presented on Figure 58, we chose to process particles with energies between 0 and 6 eV, as it is within this range that they are highly dominating the ambient ones.

The SEE flux displayed on Figure 63 shows the main direction of their incoming flux. Logically, those spacecraft emitted particles do come from regions located between AZ from 120 to 240° and EL = -45 to +60°, *i.e.* Solar Orbiter direction. However, low fluxes of secondaries seem to come from the wake region, or far from the satellite. But, as it appears on the following Figure 64: SEE arriving along those "empty" pointing directions have been highly deflected, with almost 180° bending levels which might be considered as "U-turns". This is why the combination of several parameters on those maps remain crucial to avoid any misleading in results interpretation, such as wrong origin of particle fluxes in EAS data.

➢ EAS Reference Case: trajectories and origins of detected particles

SPIS can plot particle trajectories from a detector if a sufficient number of particles are backtracked. It will provide output files of trajectories from the particles of the most important weight. So if the number of backtracked particles is not sufficient (and this number is user-defined before or during the simulation run), the information given by the set of trajectories might not be sufficient to provide clear conclusions. SPIS can of course provide trajectories of all types of scanned particles. That will be illustrated in the next simulation case. For this EAS Reference Case, an example of SEE paths is given on the following Figure 65.

It shows that most numerous secondary electrons directly come from the close vicinity of the instrument: from EAS itself and the near-by part of the rear boom. In the following it will be shown that EAS does collect SEE coming from other parts of the spacecraft, but with less important weights. Trajectories are quite useful to evaluate local potential disturbances effects on particle paths, explaining for instance some eventual increased SEE fluxes along few incoming directions. Or, on the contrary, lack of particle fluxes along the rear wake pointed region (also visible on Figure 63).

But, Figure 65 also demonstrates that the previous Figure 64 displaying deflection angles of detected secondary electrons has to be considered carefully. Indeed, the plotted trajectories show here that some particles performed several loops around the boom before reaching the sensors. Thus the

deflection angles estimated between injection and detection become sometimes irrelevant, as this parameter does not consider the intermediate paths that are visibly twisted. This is why another way of studying particle origins is definitely necessary.

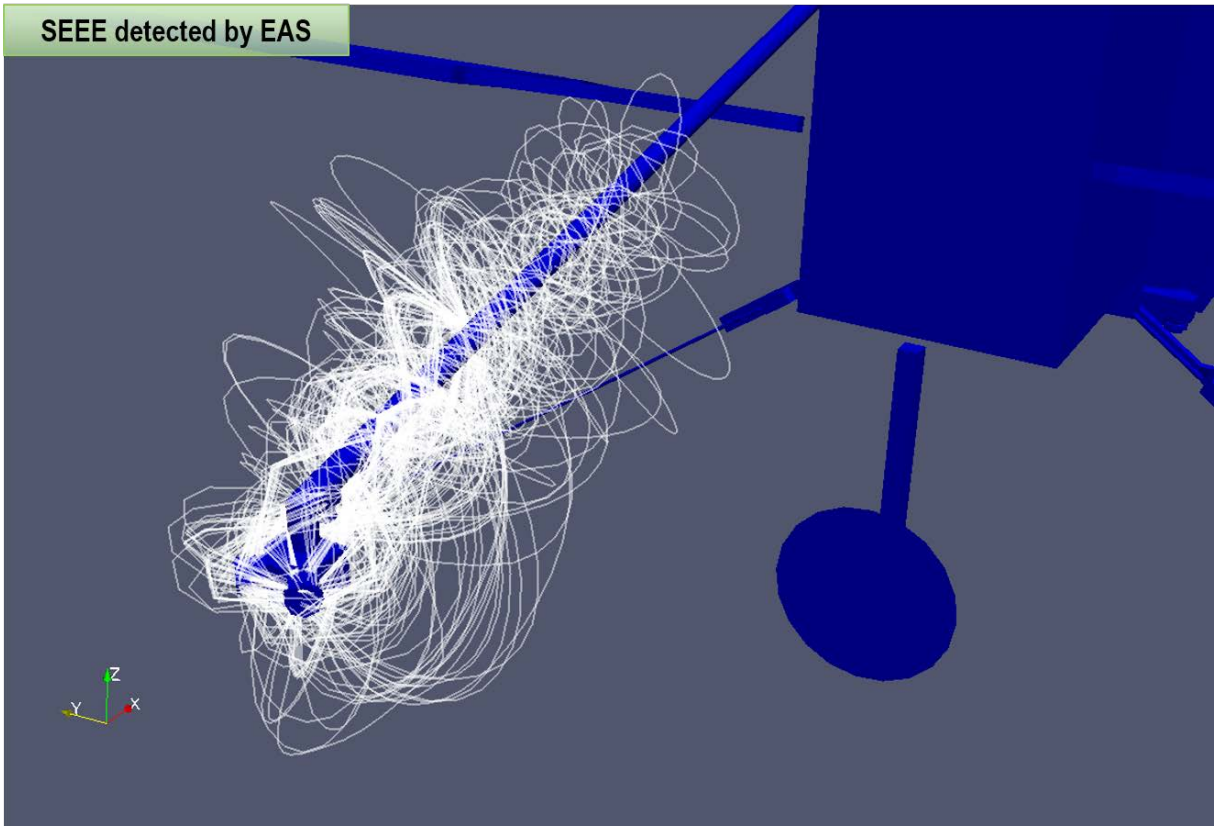

Figure 65: EAS Reference case –Trajectories of SEE with most important weight detected by EAS.

Other instrument SPIS provided output files permit to identify the 2D surfaces which are sources of currents detected by an instrument. For instance, concerning secondary electrons, each particle detector provides a file presenting the detected current value at its originating surface on the spacecraft (for example in this case to identify which part of the satellite surface contributes most to contaminating electrons to EAS). On the other side those outputs are also provided for thermal electrons (or others, if required), allowing to determine which region of the simulation box boundary contributes the most/less to thermal electron current collection on a particle detector surface.

A SPIS-external post-processing method (feasible with the *Paraview* software) consists of adding the same outputs (for all 16 particle detector surfaces which together constitute the instrument) to have a global view on the sources of currents for the entire EAS (and not for each particle detector separately). For instance, to represent the field of view of EAS concerning thermal electrons we add the *vtk* files of thermal electron currents at origin for each particle detector constituting the EAS instrument, using the *PythonCalculator* filter (a tool embedded in *Paraview* allowing to manipulate *vtk* files). SPIS output files have to be cumulated, as for the previous EAS pointing maps representation. In the following Figure 66, this post-processing method is used to show the sources of SEE current detected by EAS. It demonstrates how the rear part of Solar Orbiter body is responsible for SEE collection by EAS, especially on the +*Z* panel and the -*X* panel, in the vicinity of the boom mounted extremity. We also notice a lower rate of SEE coming from the rear SC faces located under the *Z* = 0 plane.

However, even though this post-processing method is useful to identify main detected current origins of detected particles, those SPIS output files do not allow data filtering. Another post-processing method, more powerful and efficient, is necessary, and will be presented in the following.

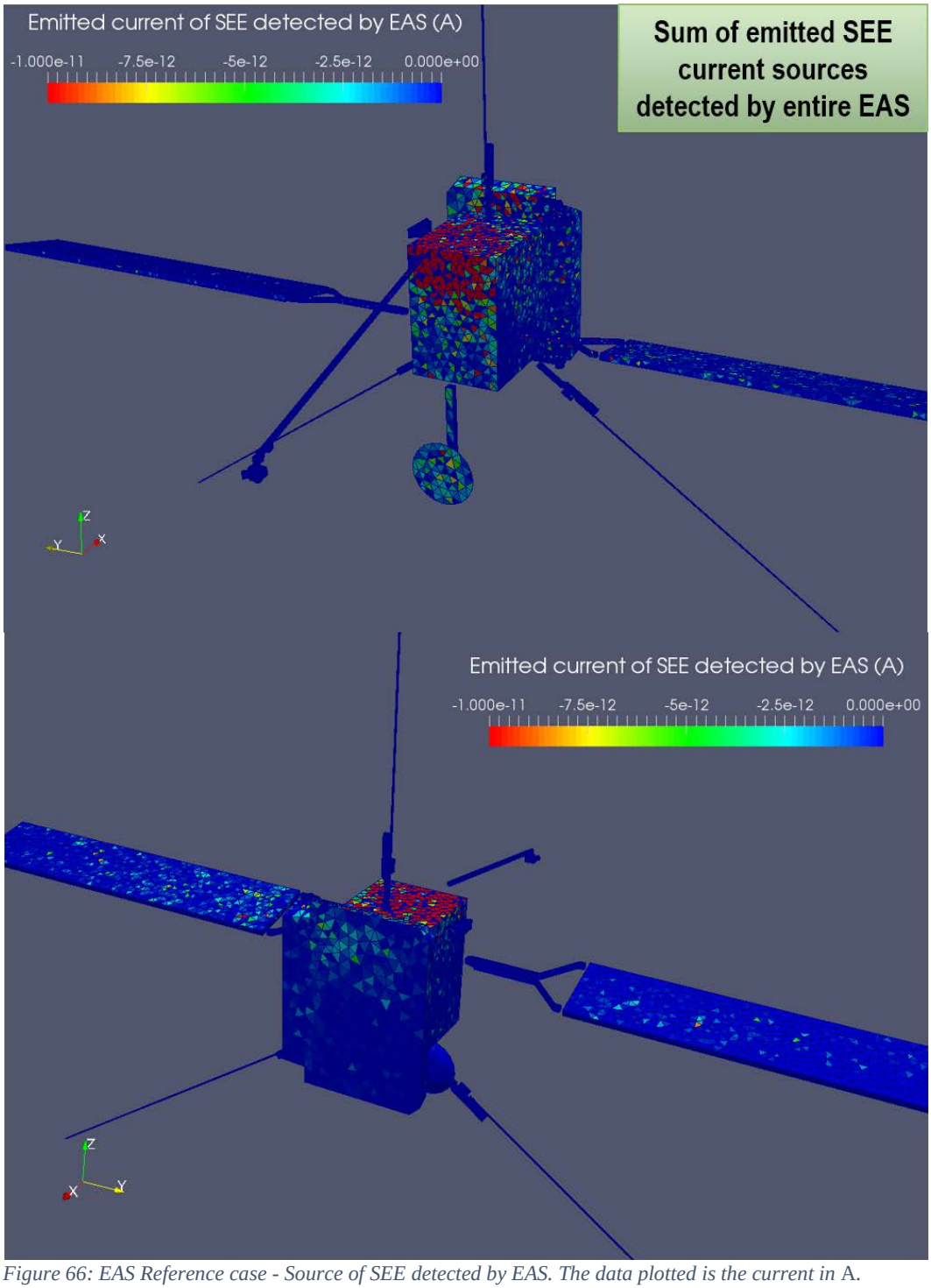

Figure 66: EAS Reference case - Source of SEE detected by EAS. The data plotted is the current in A.

The Scilab routine developed in order to generate the previous EAS pointing maps has been enhanced to provide data tables, regrouping for all detectors the measured particles origin coordinates

together with several key corresponding parameters: weight, flux, energy at injection and detection, including AZ, EL and deflection values at measurement. This allows user to filter particle locations at origin through various parameters, in order to estimate sources of data pollution under numerous conditions. It is an extension of the above-mentioned *vtk* post-processing *Paraview* method.

The following Figure 67, for example, presents origin points on spacecraft of each SEE detected by entire EAS. The color scale of the points represents the flux intensity of the corresponding particles at their arrival on the instrument. The lack of SEE coming from spacecraft regions below $Z = 0$ and from the $+Y$ areas seems here blatant. But other parameters values can be displayed on this type of Figures.

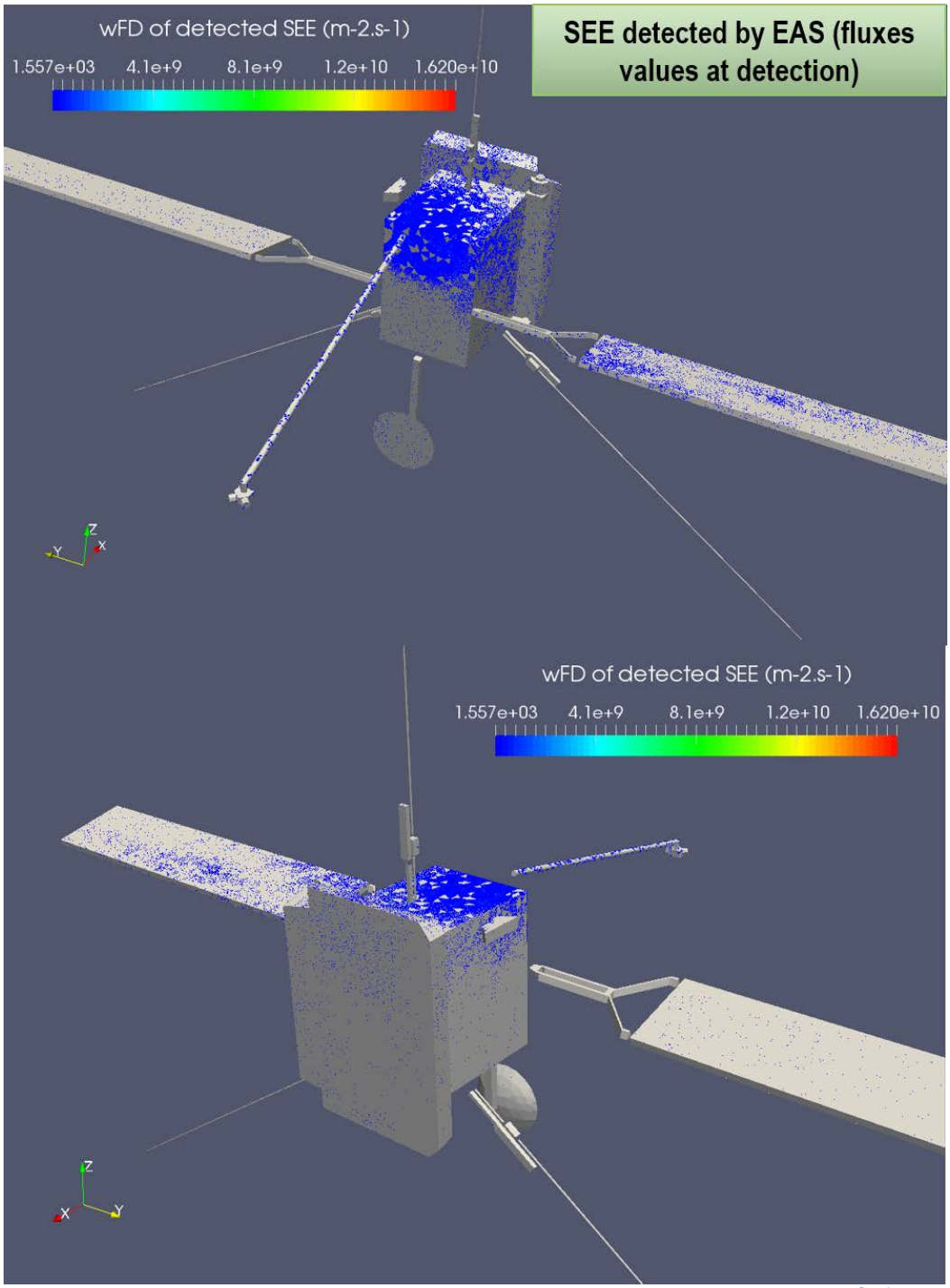

Figure 67: EAS Reference case -Origin of SEE detected by EAS, color-scaled by flux intensity -$m^{-2}.s^{-1}$) at detection.

On the next Figure 68 the color scale stands for the energy of detected SEE at detection by EAS. It shows that some of those particles do come from spacecraft surfaces below $Z = 0$ and from the $+Y$ areas, even though fluxes are lower (see Figure 67) but have higher energies (beyond 4 eV). This can be explained thanks to various Figures combination, as in the next Figure 69, where the isocontour of potential region at -3 V has been added to the illustration.

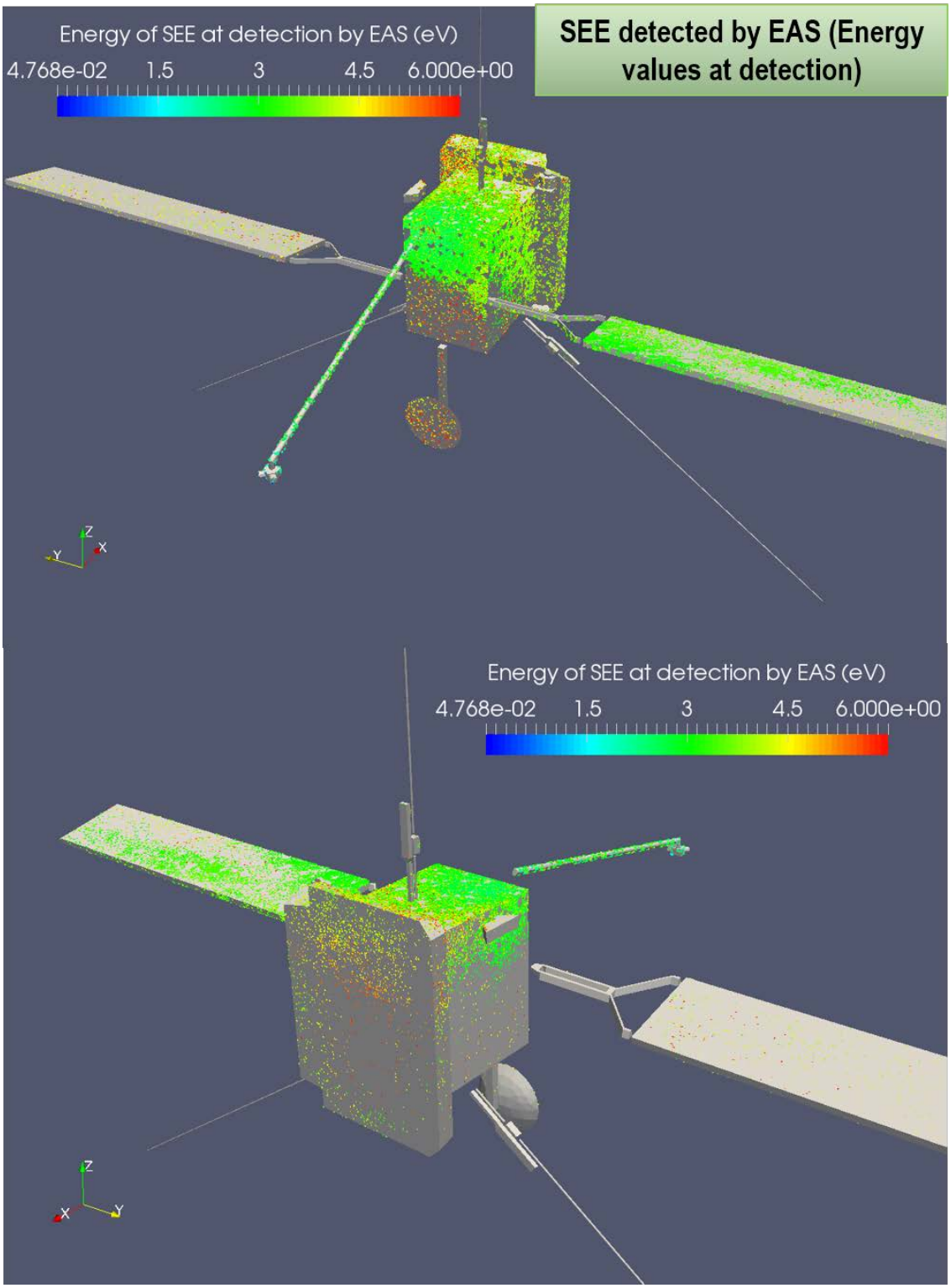

Figure 68: EAS Reference case -Origin of SEE detected by EAS, color-scaled by energy (eV) at detection

This electrostatic bubble, due to ion depletion and secondary density excess combined with satellite velocity along *Y* axis, is shifted towards the -*Z* and +*Y* frame of the computational volume,

behind Solar Orbiter. It thus constitutes an electrostatic blockade to lowest energy SEE trajectories. Only particles with higher energies (> 3 eV) can cross this region and reach EAS.

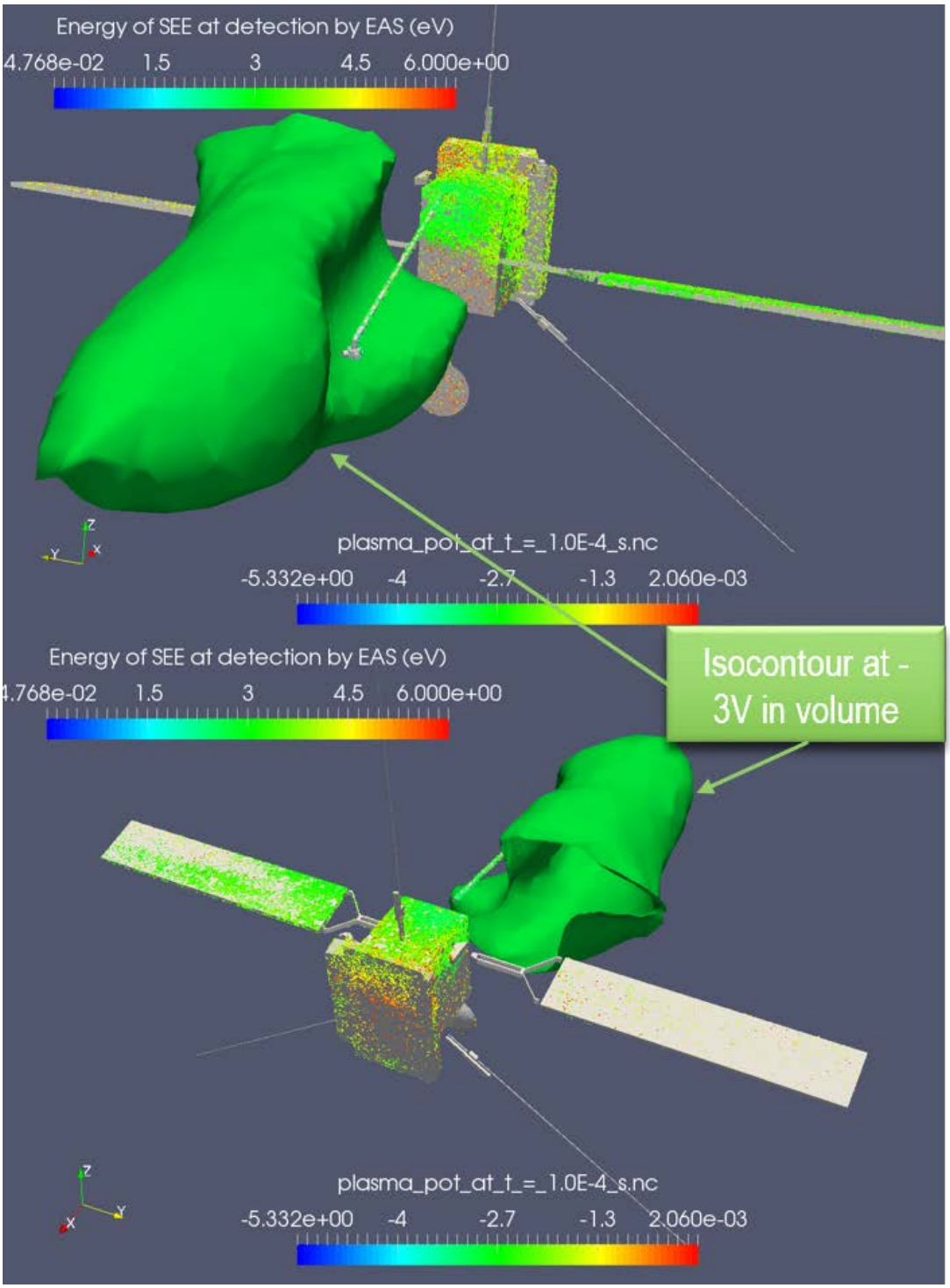

Figure 69: EAS Reference case -Origin of SEE detected by EAS, color-scaled by energy (eV) at detection, and potential volume isocontour at -3 V in the wake.

Finally, the combination of various SPIS provided output data and post-processing tools developed in the frame of this study allows to extend the usual simulation analysis and go into EAS

measurements in depth. The previous *Scilab* routine can also be used to identify particles origin for each particle detector, thanks to their identification number (from 1 to 16). But user can also color scale this previous representation by AZ or EL, density… This will be also detailed within the next simulation cases studies.

12. EAS no Baffle case

Following potentials have been set on the various spacecraft elements, and kept constant. Those potentials correspond to those obtained with the RPW Reference case: no *B*, no I_{bias}, no Dielectrics in shadow, of Section 6.5. All spacecraft elements not cited in the following table are grounded (Φ = 4.2V).

SC element	Potential (V)
Ground	4.2
RPW1	2.5
RPW2 and RPW3	2.8
SA1 and SA2 sunlit	7.7
Yoke1 and Yoke2 sunlit	9
EAS box	4.2
EAS sensors	4.2

12.1. EAS no Baffle Case: plasma state around the spacecraft

Plasma behaviour and potential remain perfectly faithful to previous observations made during the RPW Reference case study, as it is illustrated on Figure 70 below.

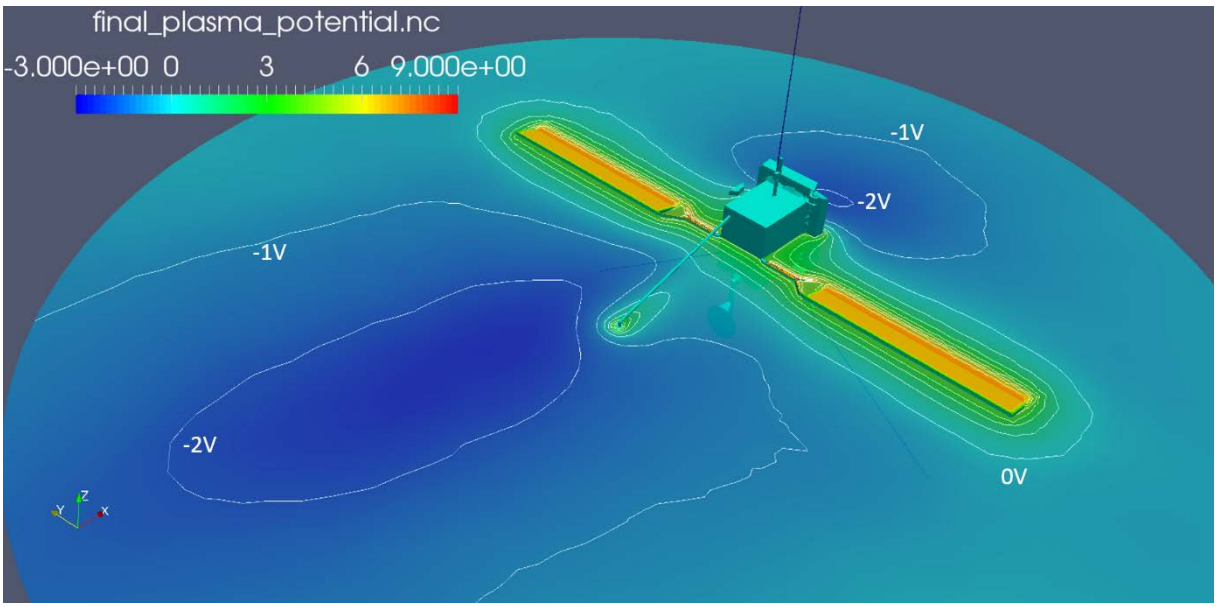

Figure 70: EAS no Baffle - Plasma potential (V) around Solar Orbiter in the X-Y plane.

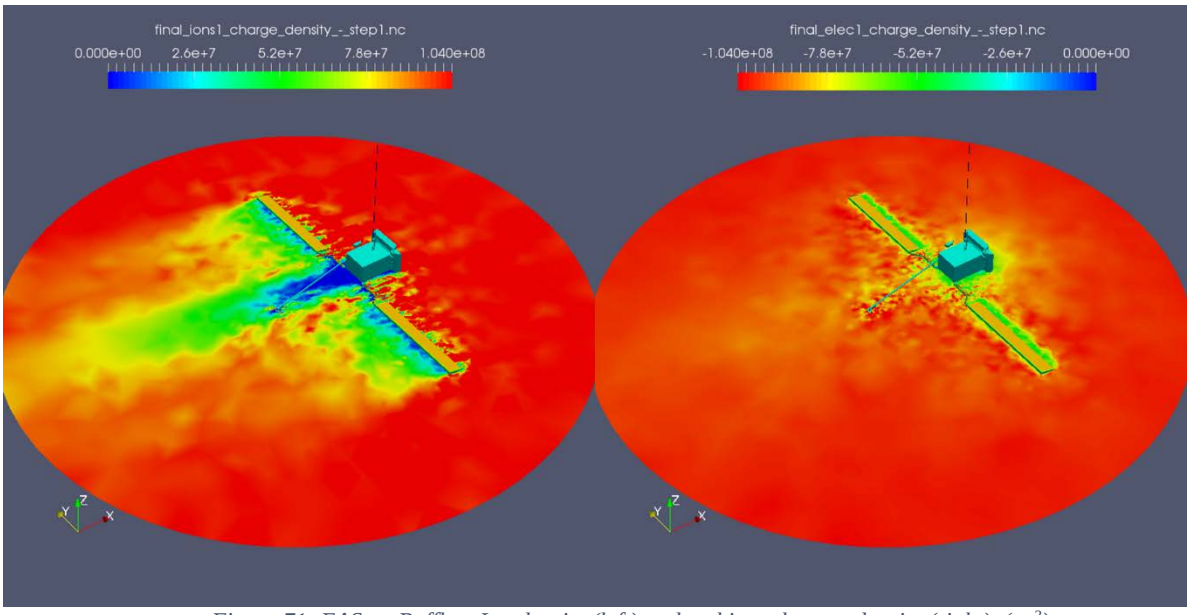

Figure 71: EAS no Baffle – Ion density (left) and ambient electron density (right), (m^{-3}).

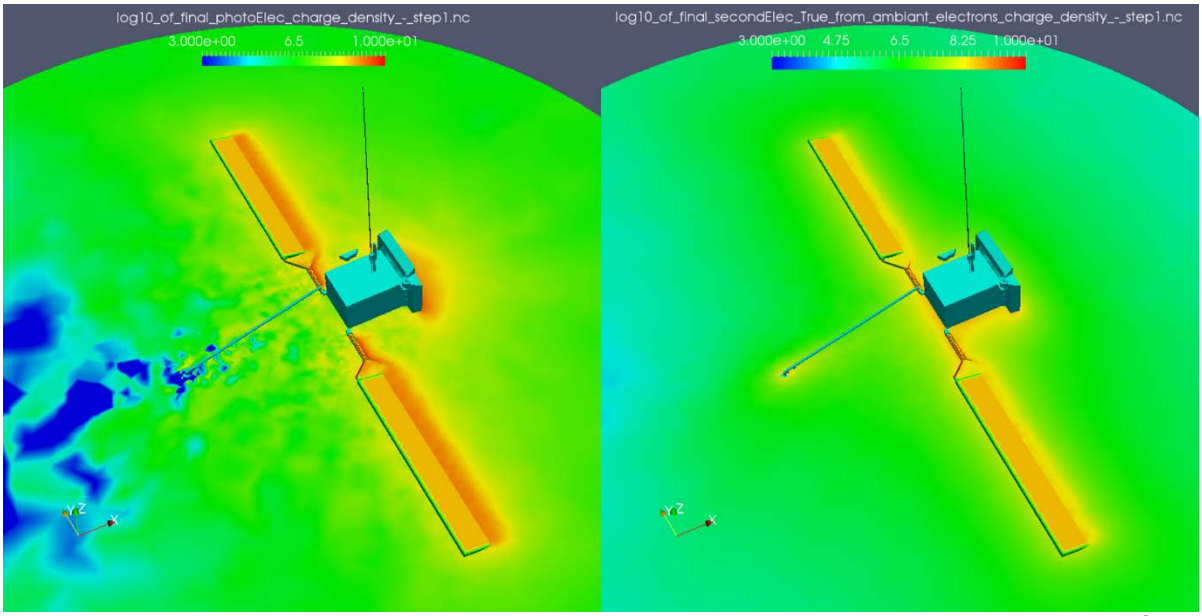

Figure 72: EAS no Baffle – Log of photoelectron density (left) and secondary electron density (right), (m^{-3}).

12.2. EAS no Baffle Case: energy distribution functions measured by EAS

As explained in Section 11.2, we can obtain the global EDF of EAS measured electrons by cumulating all detector EDF per population as follow:

$$f_E(E)_{Total} = f_E(E)_3 + f_E(E)_4 + f_E(E)_7 + f_E(E)_8 + f_E(E)_{11} + f_E(E)_{12} + f_E(E)_{15} + f_E(E)_{16} + {}^1\!/_2\,(f_E(E)_1 + f_E(E)_2 + f_E(E)_9 + f_E(E)_{10}) + {}^1\!/_2\,(f_E(E)_5 + f_E(E)_6 + f_E(E)_{13} + f_E(E)_{14})$$

The corresponding result for ambient electrons EDF is plotted on the following Figure 73. Blue curve corresponds to the sum and average of the 16 particle detectors in charge of collecting thermal

electrons. On this Figure, the gray curve represents the analytical distribution function actually injected by SPIS into the computational volume. The orange curve represents the ambient electron population that EAS should have theoretically measured, considering only its attracting potential of +4.2 V on its surface, and if this instrument was a simple sphere alone in the studied plasma. This latest function is thus a transformation of the grey one: shifted by the energy of 4.2 eV (minimum energy of particles arriving on the detector surface) and increased because of the attracting potential on the surfaces. Finally, the real measured EDF is an intermediate EDF between the two previous ones, because of the attracting potential of the EAS instrument, combined with electrostatic and physical blockades to particle detection (spacecraft body + wake potential decrease). The yellow curve is the older ambient electrons EDF measured during the previous EAS Reference Case at 0 V, for comparison. This Figure 73 shows that below Solar Orbiter and EAS potential (4.2 V): no ambient electrons can be measured.

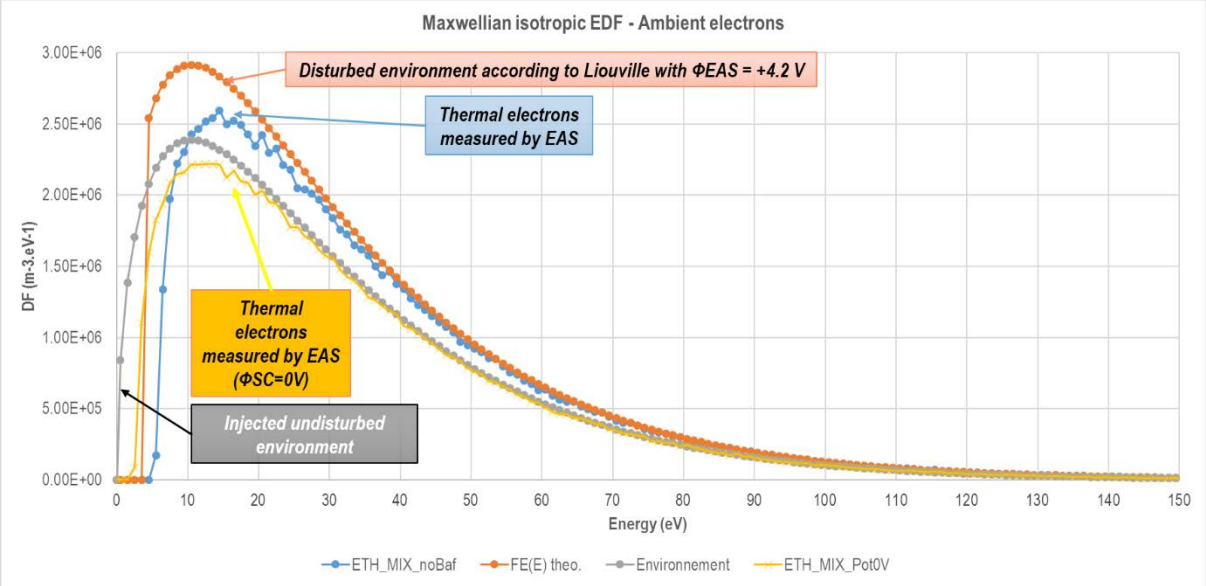

Figure 73: EAS no Baffle - EDF of ambient electrons measured by EAS.

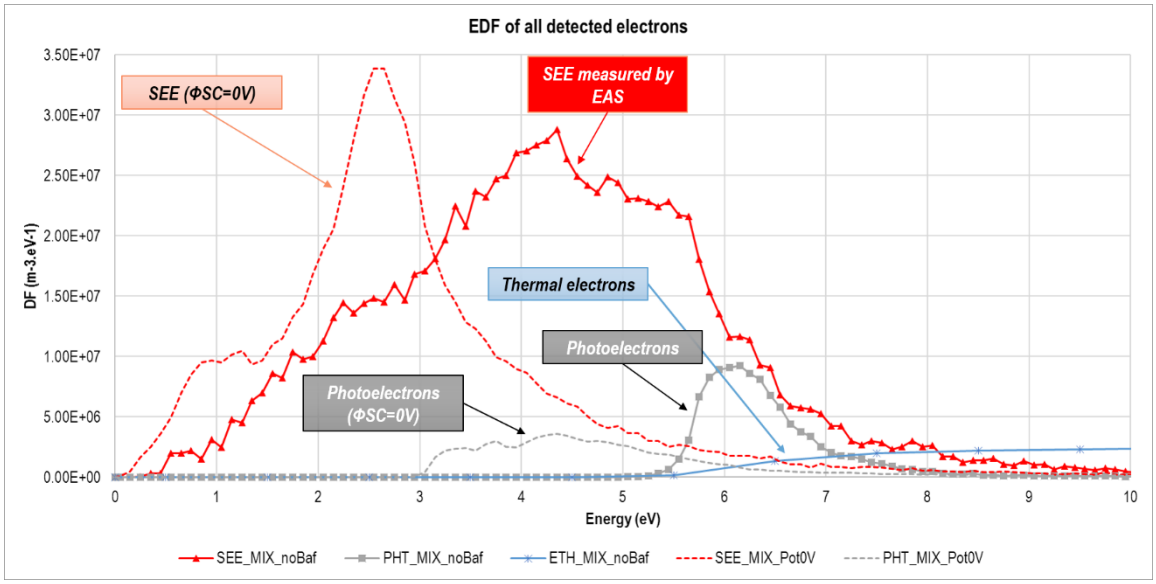

Figure 74: EAS no Baffle - -EDF of all electrons, detected by EAS. Blue curve represents ambient electrons, gray curve the photoelectrons and the red one the SEE. Dashed curves correspond to older EDF collected in the previous case.

Below 8 eV, electron measurements are highly polluted by secondary electrons, especially around 4.3 eV with a higher EDF value. Integrating those EDF allows to recover the respective measured densities. For this EAS no Baffle case with spacecraft and EAS held at +4.2 V we obtain:

- N_0 = 1.04×10^8 m^{-3}, injected environment of ambient electrons
- N_{theo} = 1.19×10^8 m^{-3}, expected density measurement for EAS alone in the plasma and charged at +4.2 V,
- N_{ThE_meas} = 1.05×10^8 m^{-3}, actual measurement of ambient electron density in this simulation conditions,
- N_{SEE} = 1.06×10^8 m^{-3}, secondary electron density measured by EAS,
- N_{Ph} = 1.08×10^7 m^{-3}, photoelectron density measured by EAS.

Finally, the ambient electron density measured by EAS in those conditions (N_{ThE_meas}) is 1.59 % superior to the undisturbed one, because of negative plasma potential regions around the instrument and EAS + SC body attracting potential. If we include parasite electrons to this calculation: the total electron density measured reaches 2.26×10^8 m^{-3}, which is an increase of 114.6 % regarding the undisturbed environment.

Comparing those results to the Reference Case: N_{ThE_meas} is increased by 11.1% (because of the attracting surface potential here), N_{SEE} by 52.1%, N_{Ph} by 27.2%, for the same reasons.

12.3. EAS no Baffle Case: advanced post-processed outputs provided by EAS numerical instrument

As already performed in Section 11.3 for the EAS Reference Case, we can combine EAS specific outputs to obtain the global vision of EAS for those simulation conditions.

➢ EAS no Baffle Case: Pointing maps

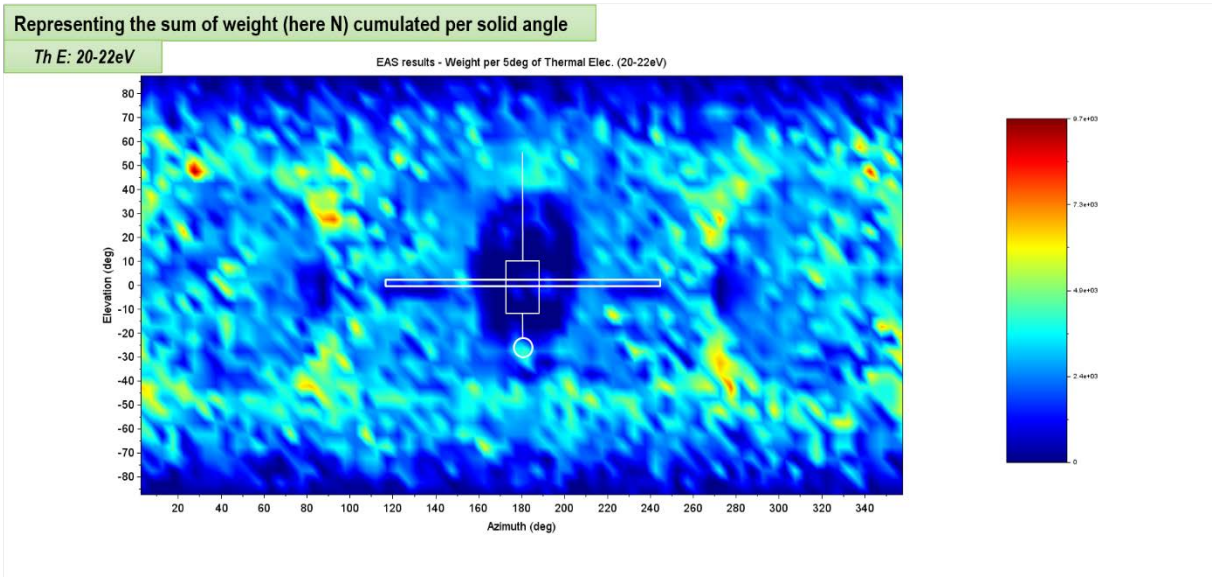

Figure 75: EAS no Baffle case – Pointing map of EAS for ambient electrons flux at 21 eV (m^{-3}).

We first present on Figure 75 the cumulated flux of ambient electrons detected by EAS. The weight is here expressed as a related density (m^{-3}). Regarding the previous Reference case where the flux displayed concerned ambient electrons within 10 to 20 eV energy range, the results are here focused around 21 eV (so between 20 and 22 eV), as it is the mean kinetic energy of the injected undisturbed

electrons in the computational volume. This reduction of energy span does lower number of filtered particles and consequently the statistics. But note that user can configure its *Scilab* routine as he wants and cover any energy range if necessary.

Same effects that for Figure 61 appear for this simulation with spacecraft and EAS charged at +4.2 V.

- the artificial flux increase on the specific common pointing regions: the flux is nearly doubled,
- the decreasing flux at high Elevation levels (±80 to 90°): due to the reference frame configuration (when pointing to high absolute values of EZ, whatever the AZ value: EAS points practically towards the same single direction),
- the Solar Orbiter body trace is clearly visible on the map, with effects on flux losses. The physical elements are direct physical obstacles to electron detection towards those directions, as those particles cannot get through its structure,
- furthermore: electrostatic effects directly due to spacecraft charging that bent electron trajectories (even at this higher energy level of 21 eV), and enlarge SC trace (and the flux reduction area) on this flux map,
- finally: the two spots of flux losses at null EL and AZ = 90 and 270°, still the consequence of each EAS sensor pointing towards the other.

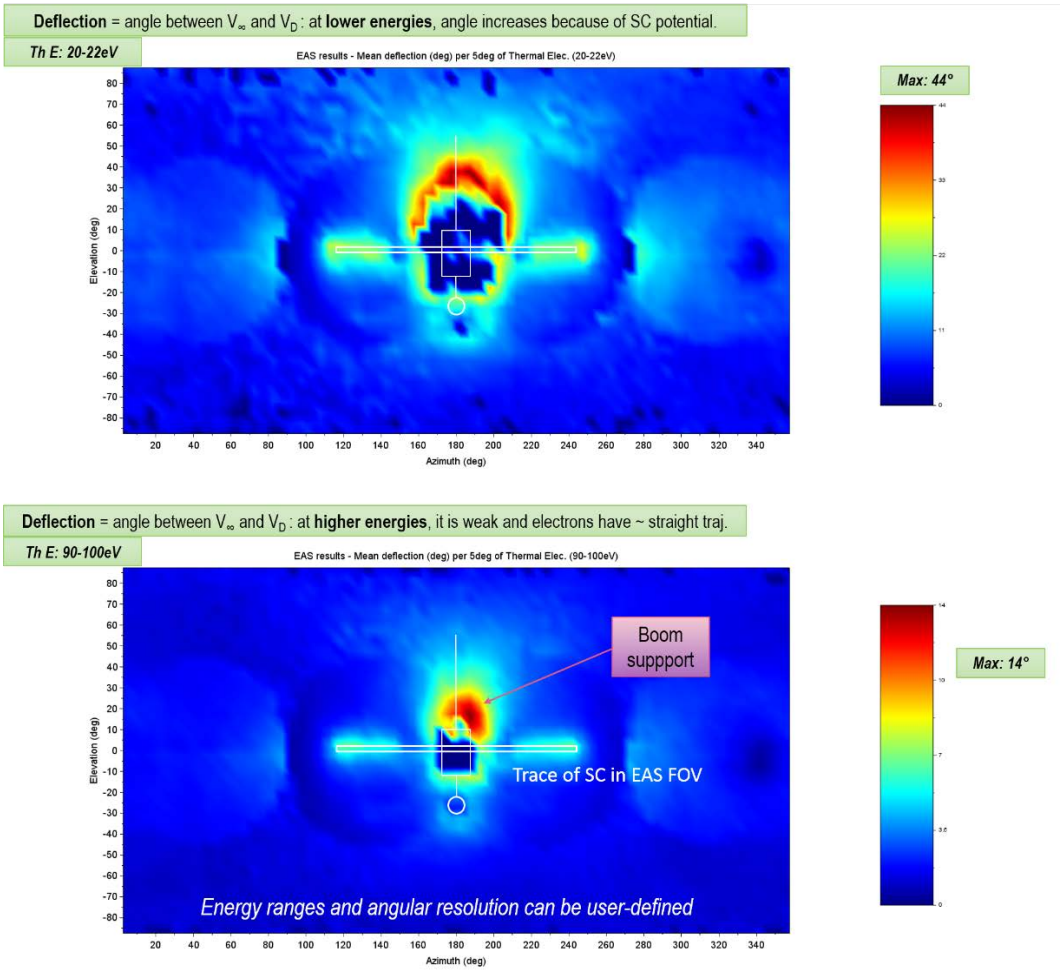

Figure 76: EAS no Baffle Case - Pointing maps of EAS for ambient electrons deflection angle. 20-22 eV range (top) and 90-100 eV (bottom).

Concerning deflection angles for those ambient electrons: pointing maps are displayed on Figure 76, with a 21 eV array on top, and a comparison with higher energies (90-100 eV) below. It shows the sensitivity of lower energy electrons to even small level of satellite charging (+9 V maximum on yokes), and the path bending of detected elements. Compared to high energy ranges (Figure 76, bottom): those particles have practically rectilinear paths and the maximum bending angle reaches 14° (44° at 21 eV). This last map allows to figure out quasi-perfectly the Solar Orbiter design viewed from EAS location. The rear boom, supporting the instrument along a certain direction, clearly appears here: incoming electrons which paths are aligned with this boom axis direction have been more deflected than others, because of the long charged surface influencing the negative charges during their venue to EAS sensor.

- EAS no Baffle Case: trajectories and origins of detected particles

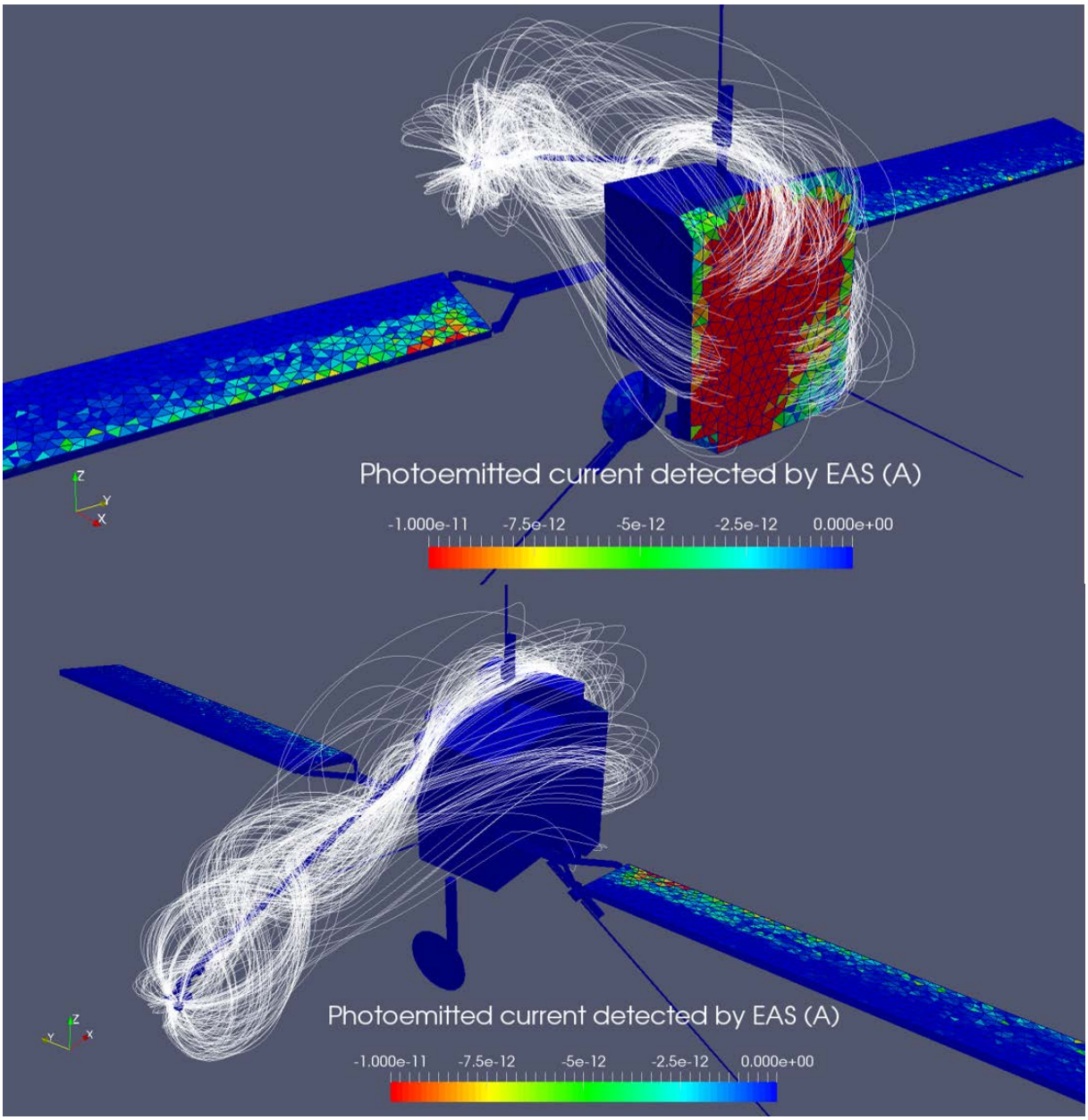

Figure 77: EAS no Baffle Case - Trajectories of Photoelectrons with most important weight detected by EAS, combined to sources of those particles (in A)

In the previous Reference Case at 0 V, we plotted some secondary electron trajectories detected by the instrument, directly provided by SPIS. For this present case: we plot here (Figure 77) the photoelectron ones, combined to the 2D surfaces which are sources of photo-current detected by EAS. It appears that most of detected photoelectrons come from the heat shield, which is the largest spacecraft surface exposed to the UV flux. Some particles arrived on EAS with a different origin (coming from the rotated solar arrays for instance), but in a lower proportion. As before, particles sometimes performed several loops in the volume, especially around the boom, before being captured by the sensors.

The *Scilab* routine allows the plotting of many information for those detected photoelectrons. An example is given here below (Figure 78), with the plot of their origin, detailed with their energy at detection. It shows that most positively charged faces recollect the majority of photoelectrons (solar

arrays and supporting yokes). Surprisingly, even though the RPW antennas are very thin compared with other spacecraft elements, they are still sources of photoelectrons that can reach EAS.

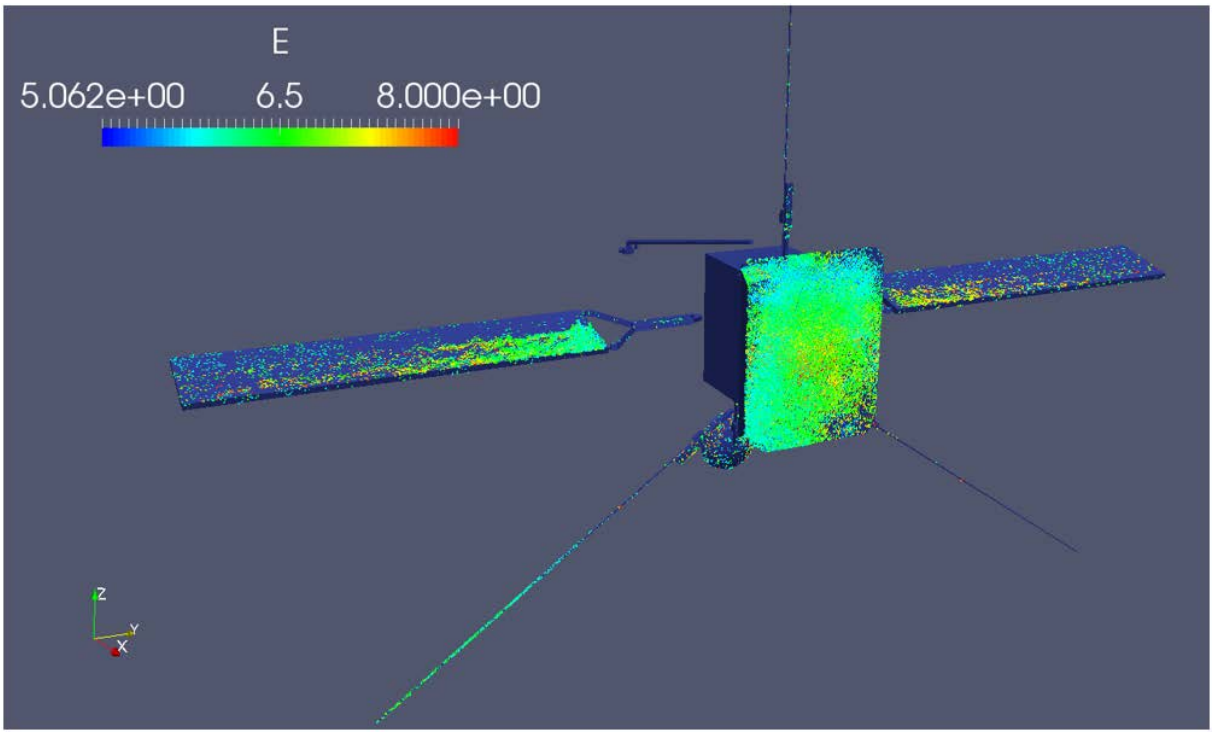

Figure 78: EAS no Baffle Case --Origin of Photoelectrons detected by EAS, color-scaled by energy (eV) at detection.

13. EAS Baffle case

This simulation configuration is extremely similar to the previous EAS no Baffle Case, except that now the EAS baffle has been added to the CAD model, as illustrated on the following Figure 79. This baffle has been declared here as covered with black Kapton, as for the boom.

Concerning potentials, same values that for the previous no Baffle Case have been considered (and kept constant), and the baffle surface has been set to the same potential that EAS and spacecraft ground: +4.2 V. Those chosen values correspond to those obtained with the RPW Reference case: no *B*, no I_{bias}, no Dielectrics in shadow, of Section 6.5. All spacecraft elements not cited in the following table are grounded (Φ = 4.2V).

Note that, as for the previous simulation, this one is configured to provide main CPU efforts on the Particle Detector backtracking processes. First steps of simulation (particle pushing and Poisson Solver computation) are quite quickly performed in order to reach plasma stability, before intense computation of particle backtracking measurements.

SC element	Potential (V)
Ground	4.2
RPW1	2.5
RPW2 and RPW3	2.8
SA1 and SA2 sunlit	7.7

Yoke1 and Yoke2 sunlit	9
EAS box	4.2
EAS sensors	4.2
EAS Baffle	4.2

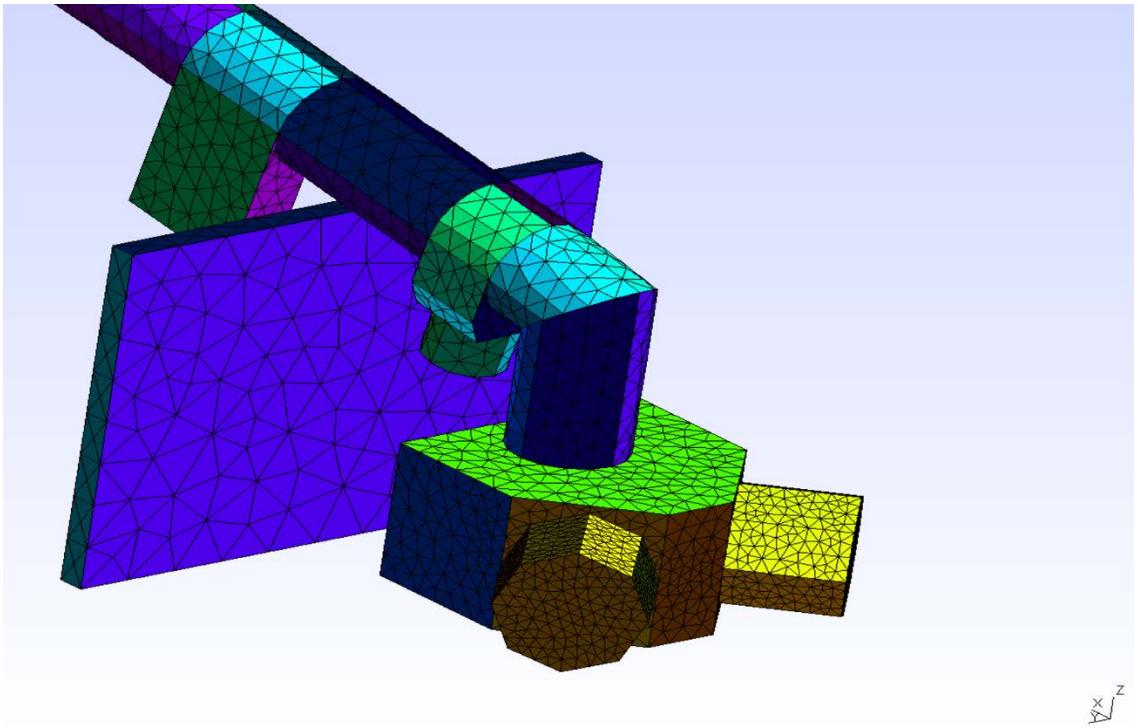

Figure 79: EAS Baffle Case – CAD model of EAS including the baffle.

13.1. EAS Baffle Case: plasma state around the spacecraft

With this simulation: plasma behaviour and potential remain perfectly faithful to previous observations made during RPW no Baffle case, as the difference between the two cases rely in a small CAD model change, already located in the ion wake, and in the Sun shadow. Study on *vtk* files with focuses on the baffle region did not show major changes regarding the former CAD situation, except of course concerning the secondary electron density in the vicinity of EAS. The baffle SEE emission increases this population density around the instrument and foretell a light overflow of SEE in EAS measurements. Secondary electron density around EAS is displayed on the following Figure 80.

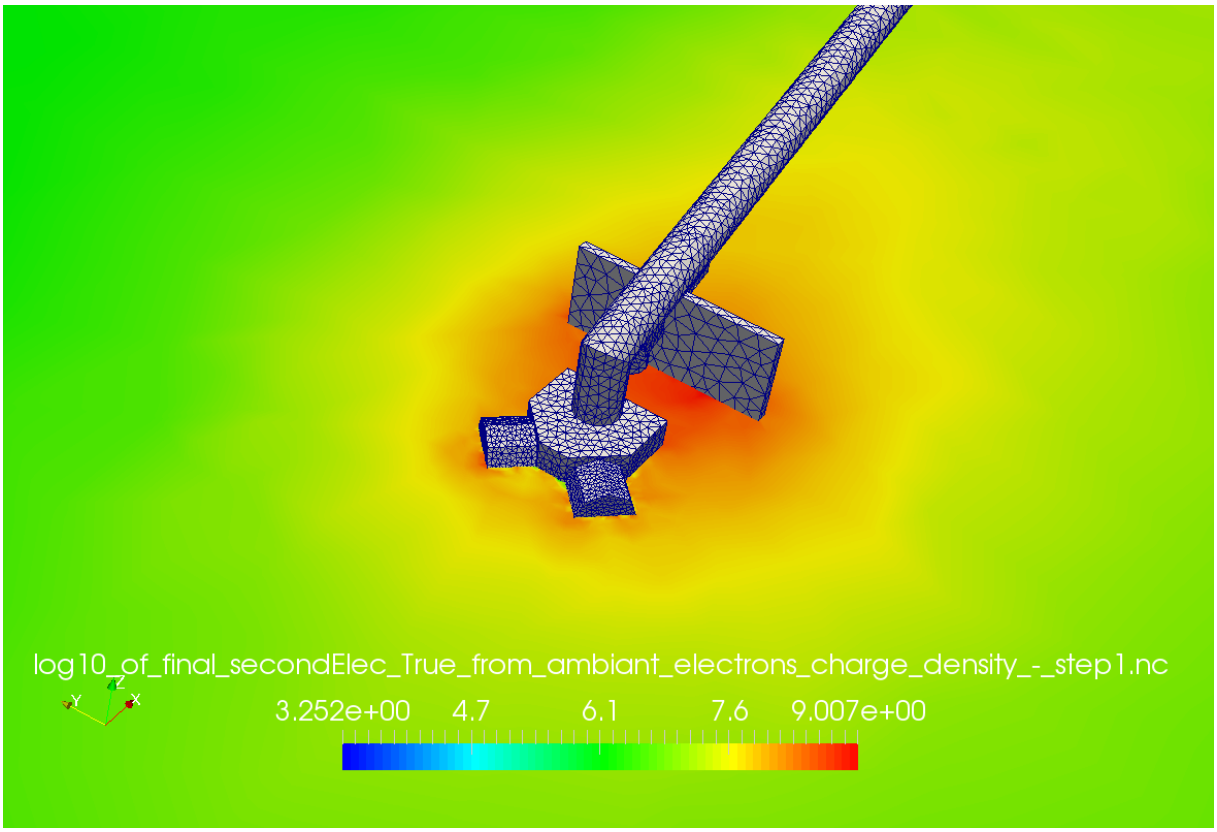

Figure 80: EAS Baffle Case – Log10 of SEE density in the vicinity of EAS.

13.2. EAS Baffle Case: energy distribution functions measured by EAS

EDF measured by EAS during this simulation are presented here-after (Figure 81and 82).

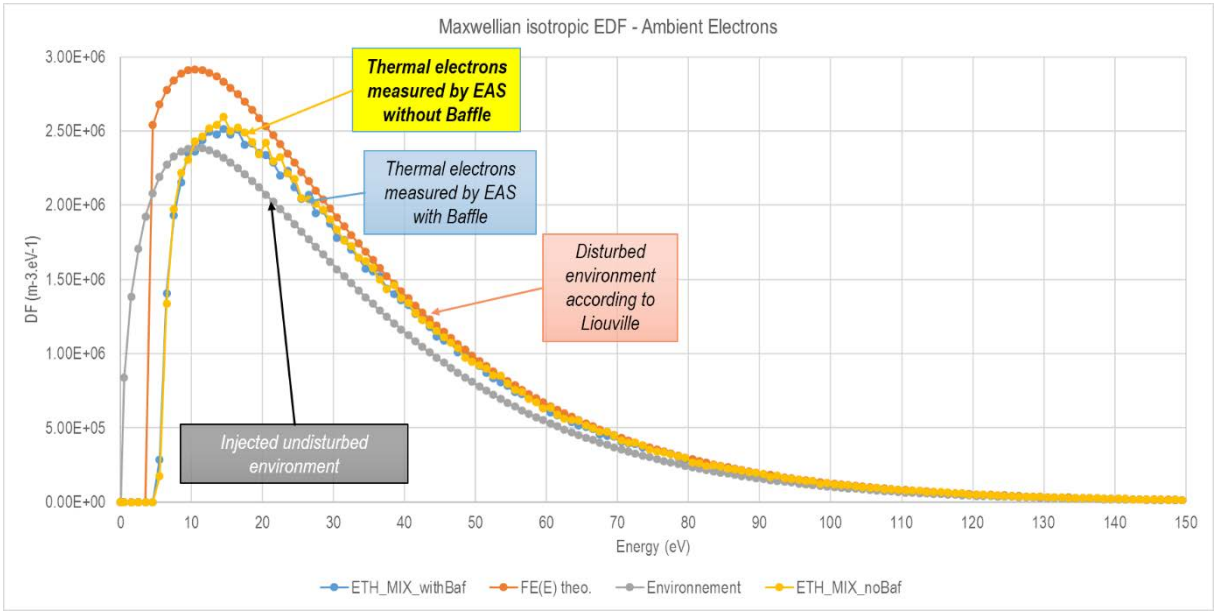

Figure 81: EAS Baffle Case - EDF of ambient electrons measured by EAS.

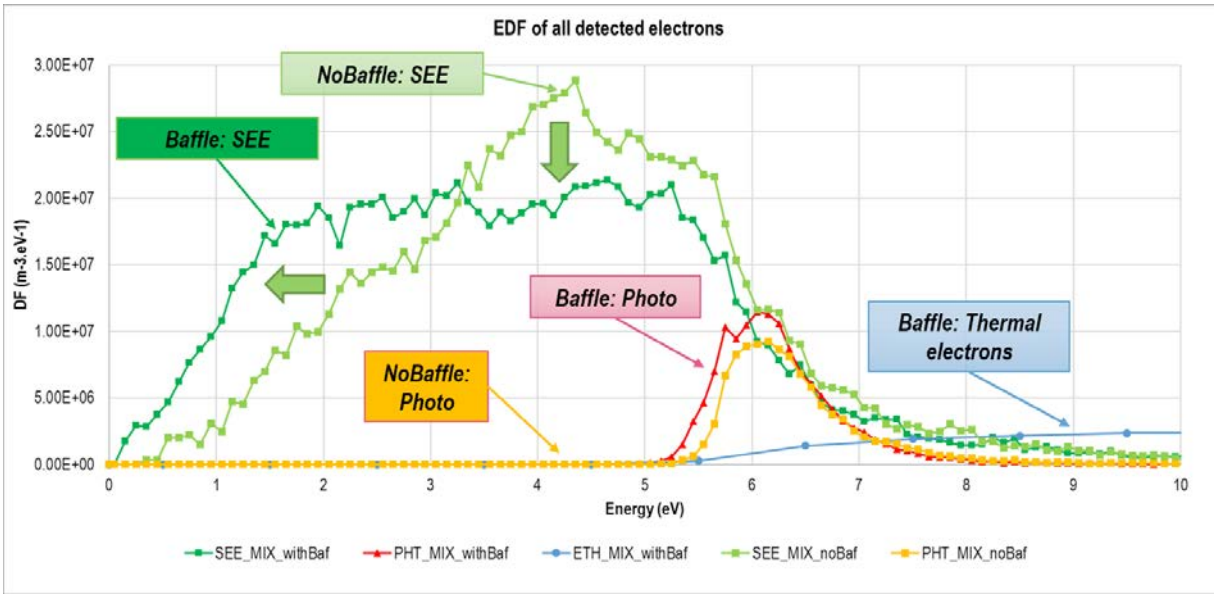

Figure 82: EAS Baffle Case - EDF of all electrons measured by EAS, comparison with no Baffle Case.

As before: blue curves on those Figures correspond to the sum and average of the 16 particle detectors in charge of collecting thermal electrons. On Figure 81, the gray curve represents the analytical distribution function actually injected by SPIS into the computational volume. The orange curve represents the ambient electron population that EAS should have theoretically measured, considering only its attracting potential of +4.2 V on its surface, and if this instrument was a simple sphere alone in the studied plasma. Finally, the real measured EDF is an intermediate EDF between the two previous ones, because of the attracting potential of the EAS instrument, combined with electrostatic and physical blockades to particle detection (spacecraft body + wake potential decrease). The yellow curve is the older ambient electrons EDF measured during the previous EAS no Baffle Case, for comparison. This Figure 81 shows that below Solar Orbiter and EAS potential (4.2 V): no ambient electrons can be measured.

Below 8 eV, electron measurements are highly polluted by secondary electrons. Integrating those EDF allows to recover the respective measured densities. For this EAS no Baffle case with spacecraft and EAS held at +4.2 V we obtain:

- N_0 = 1.04×10^8 m^{-3}, injected environment of ambient electrons,
- N_{theo} = 1.19×10^8 m^{-3}, expected density measurement for EAS alone in the plasma and charged at +4.2 V,
- N_{ThE_meas} = 1.04×10^8 m^{-3}, actual measurement of ambient electron density in this simulation conditions,
- N_{SEE} = 1.08×10^8 m^{-3}, secondary electron density measured by EAS,
- N_{Ph} = 1.32×10^7 m^{-3}, photoelectron density measured by EAS.

With the baffle, the ambient electron density measured by EAS (N_{ThE_meas}) is 1.2 % inferior to the one obtained without the baffle. This new element did impact ambient electron detection because of its physical presence and potential disturbance, even though this measurement discrepancy remains small. Surprisingly, fears concerning secondary electron fluxes on EAS generated by the baffle are disconfirmed. The baffle presence even reduced SEE quantity in measurements by 2.2% (we can consider that SEE proportions are equal). This phenomenon is visible on the corresponding EDF on Figure 82, when comparing the two green curves: the baffle just modified the EDF aspect, stopping the incoming electrons of “high” energies (from 3 to 6 eV) which did reach EAS without the baffle presence,

but increasing those of "lower" energies (below 3 eV), which probably come from this baflle itself. This will be investigated further.

If we include parasite electrons to this calculation: the total electron density measured reaches 2.25×10^{8} m^{-3}, which is an increase of 118 % regarding the undisturbed environment. We also notice an increase of photoelectron population detected. Results of computed densities are summed up in the following table.

Value	With Baffle (m^{-3})	Without Baffle (m^{-3})	Diff Δ w#w/o
N_{meas}	1.0365×10^{8}	1.0487×10^{8}	**-1.2%**
N_{SEE}	1.0822×10^{8}	1.0593×10^{8}	**-2.2%**
N_{photo}	1.3243×10^{7}	1.0791×10^{7}	**+23%**
N_{total}	2.2511×10^{8}	2.2158×10^{8}	**+1.6%**

13.1. EAS Baffle Case: advanced post-processed outputs provided by EAS numerical instrument

As already performed in Section 11.3 for the EAS Reference Case, and 12.3 for the EAS no Baffle Case, we can combine instrument specific outputs to obtain the global vision of EAS for those simulation conditions.

➢ EAS Baffle Case: Pointing maps, trajectories and origins of SEE

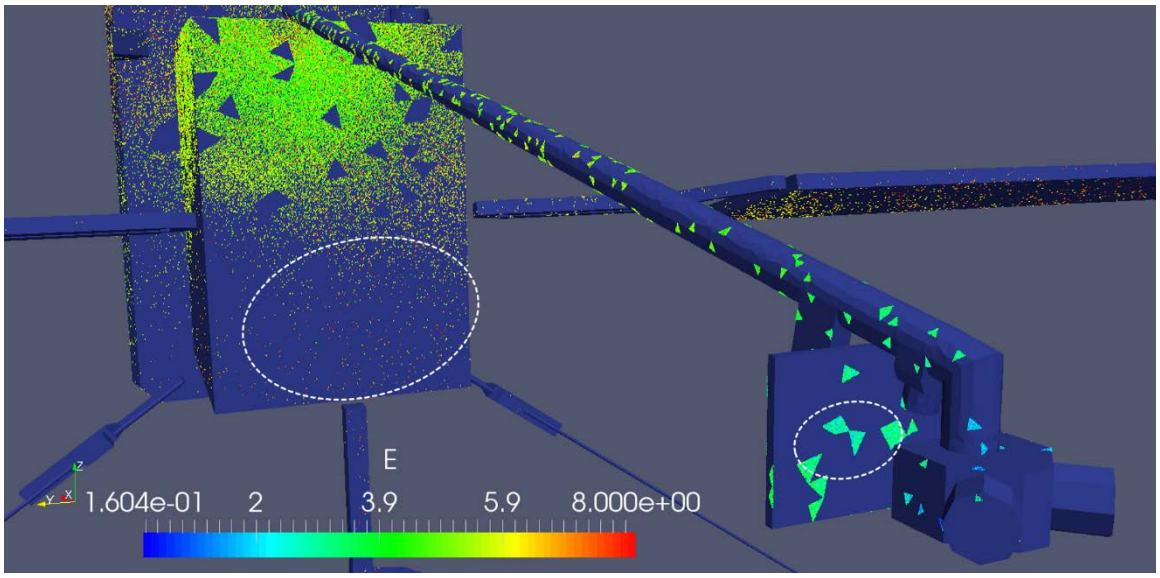

Figure 83: EAS Baffle Case --Origin of SEE detected by EAS, color-scaled by energy (eV) at detection

We can first compare secondary electron vision of EAS without/with baffle. First, concerning the flux of those particles. As explained before, it seems that, globally, the rate of SEE detected remains practically unchanged, as demonstrated in the previous Section thanks to the comparison of computed secondary density (~2% of difference), using detected EDF. Particles originated from the Solar Orbiter

body, blocked by the baffle, are “compensated” by those coming from the baffle itself. Only the aspect of the Energy Distribution Function is modified by this protection. Figure 83 above shows this “transfer” of SEE origins thanks to our *Scilab* routine processing.

This is also sown on the following Figure 84, where the baffle presence (represented by the white sketch at the center of the bottom pointing map) clearly affects particle detection at the middle of this image, with the absence of SEE flux. While on the top image particles can reach EAS when it points towards the spacecraft rear face. High SEE fluxes are also deviated when the baffle is mounted behind the instrument: on the bottom image it appears that most numerous secondary electrons do come from the baffle direction itself, while on the top image (without baffle) they arrive from directions almost aligned with the rear boom direction.

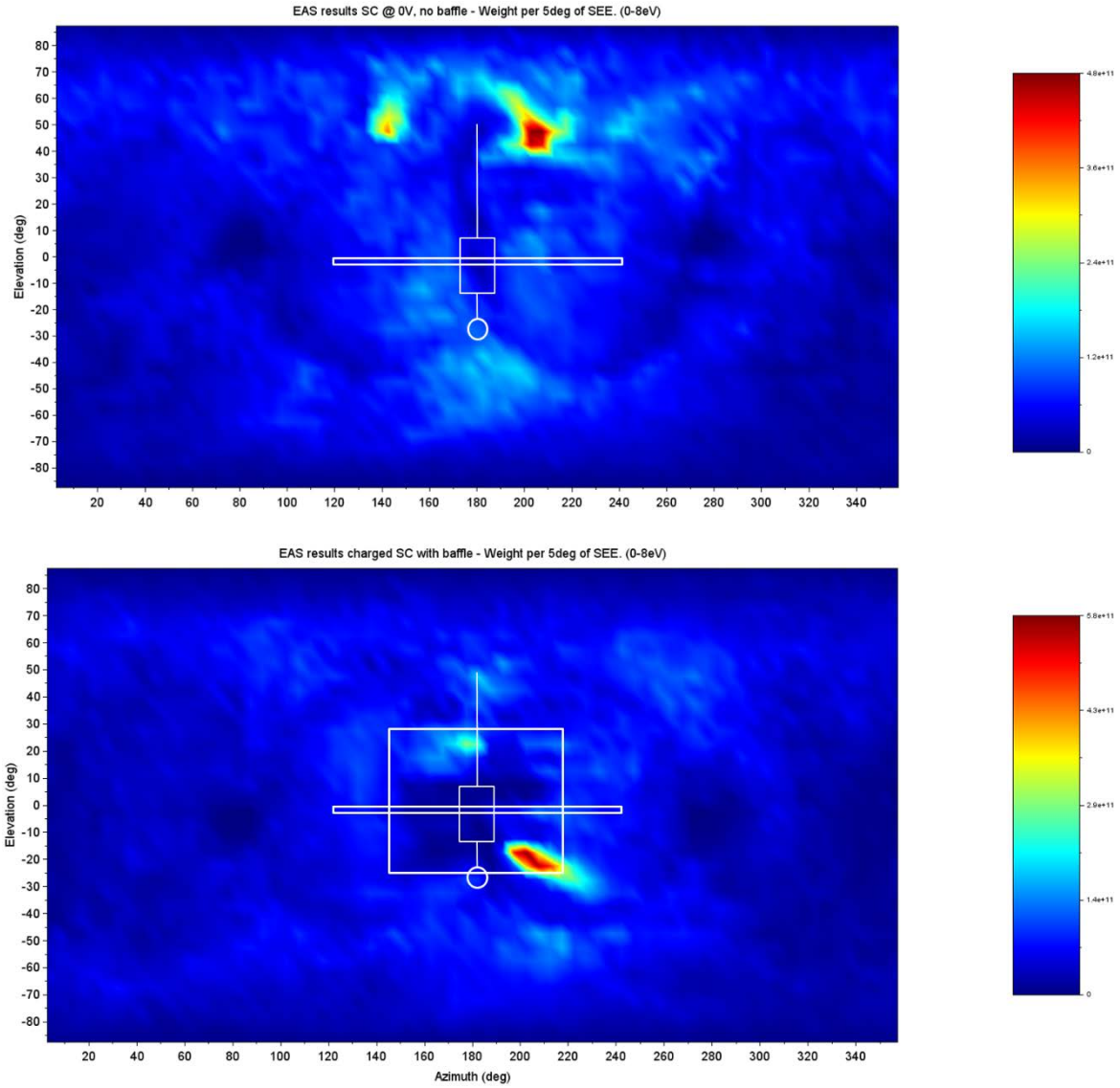

Figure 84: EAS pointing maps – Comparison of SEE detection fluxes: no baffle (top), with baffle (bottom) ($m^{-2}.s^{-1}$)

This phenomenon is also visible on the next Figure 85, displaying a comparison of secondary electron deflection at detection by the instrument without baffle (on top) and with it (bottom).

Note that those maps have been obtained using outputs of two other SPIS runs. It was indeed decided to try to enhance statistics with more performant simulations, using increased number of particle detector backtracked particles. Values "*instrument_NbOctreeMax*" and "*instrument_NbPartMax*" have been quadrupled, changing from respectively 10000 and 100000 to 40000 and 400000. This allowed to get richer and more precise results concerning particle detector output files. However, simulations got highly expensive in terms of memory cost and CPU time for computation. When previous cases "EAS no Baffle" and "Baffle Case" lasted around 24 hours, those enhanced simulations lasted between 5 and 7 days, depending on the used computer capacities.

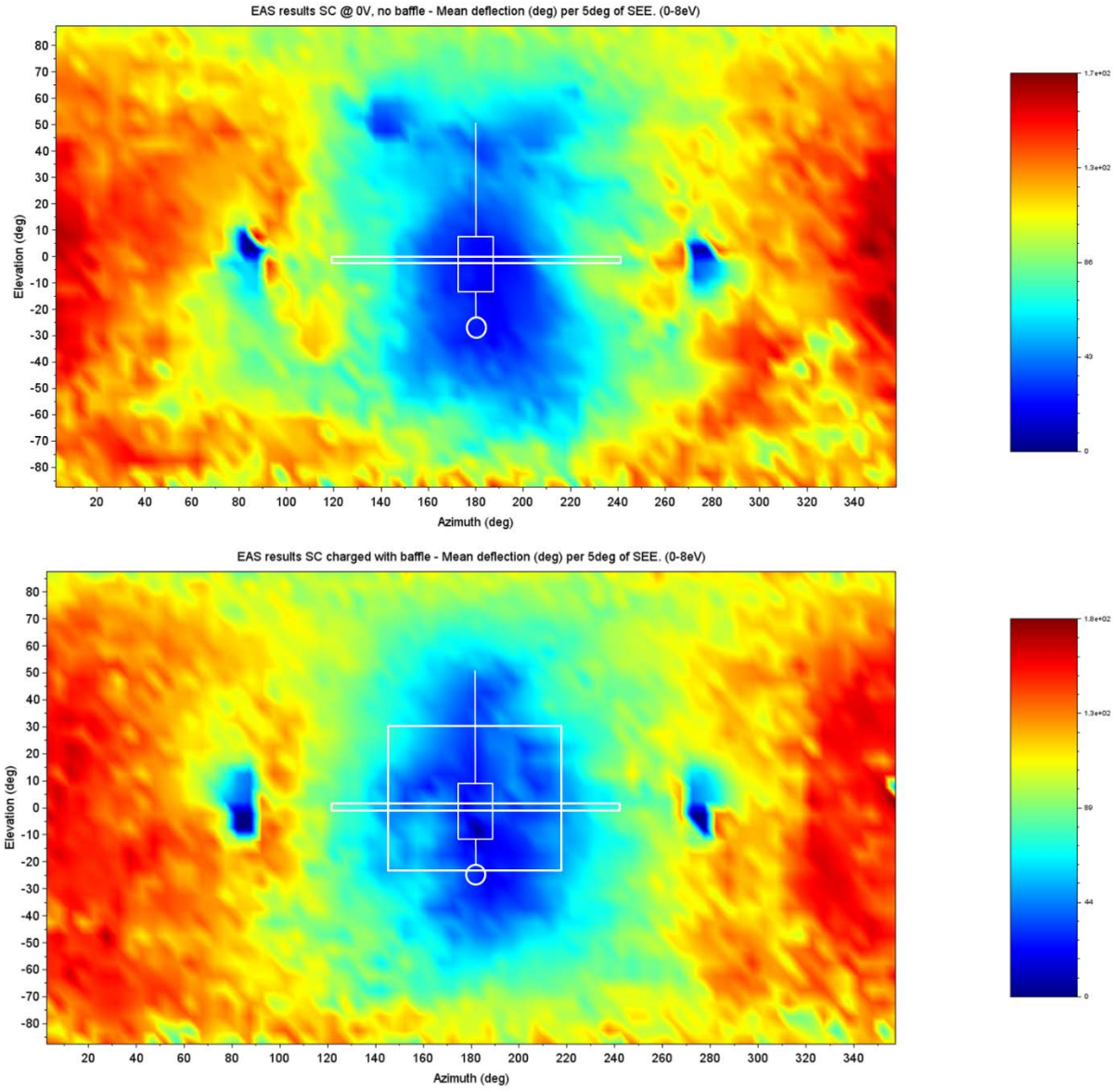

Figure 85: EAS pointing maps – Comparison of SEE deflection (°): no baffle (top), with baffle (bottom).

➢ EAS Baffle Case: Pointing maps, trajectories and origins of Photoelectrons

Let us now take a look to photoelectron behavior depending on the baffle presence. According to previous EDF integration, the baffle seemed to increase photoelectron presence within EAS detection. Indeed, the density of those particles rose by 23%, even though they remain negligible when compared to SEE parasites (a maximum density of 1.3×10^{7} m^{-3}, one order of magnitude lower then secondary electrons).

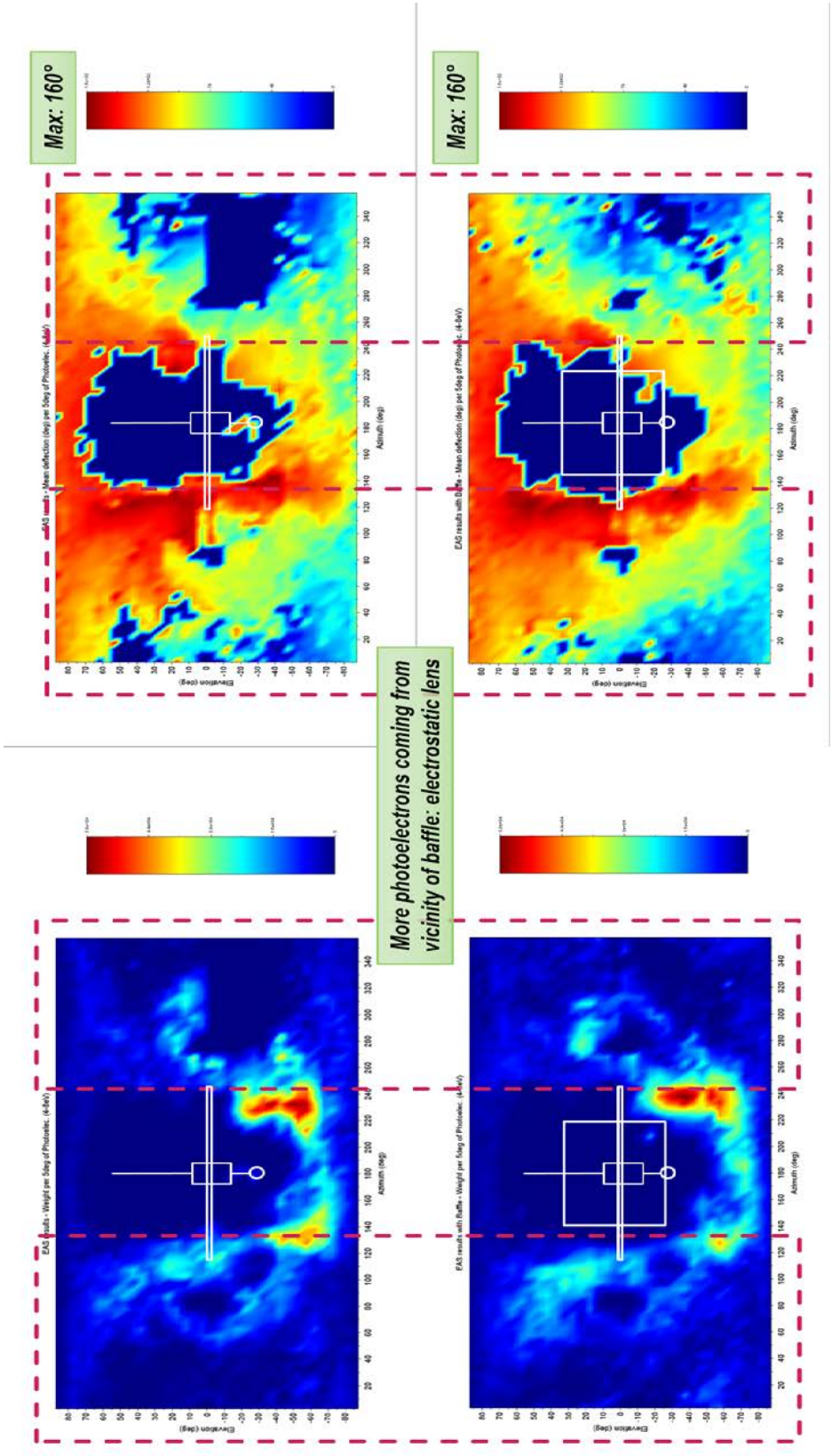
Max: 160°
Max: 160°
More photoelectrons coming from vicinity of baffle: electrostatic lens

Figure 86: EAS pointing maps – Comparison of Photoelectron deflections on the right (°): no baffle (top), with baffle (bottom) and measured Weight on the left (in density m^{-3}), no baffle (top), with baffle (bottom).

Figure 86 displays the comparison of photoelectron detection with and without baffle. It shows the modification of particle incoming directions, due to this protection baffle presence. Photoelectrons have been more importantly deflected around the baffle. This element acted like an electrostatic lens, capturing photoelectrons from wider areas around EAS, and redirecting them towards the sensors. Without the baffle, those electrons could continue their path towards -*X* part of the simulation volume, even when they passed by EAS.

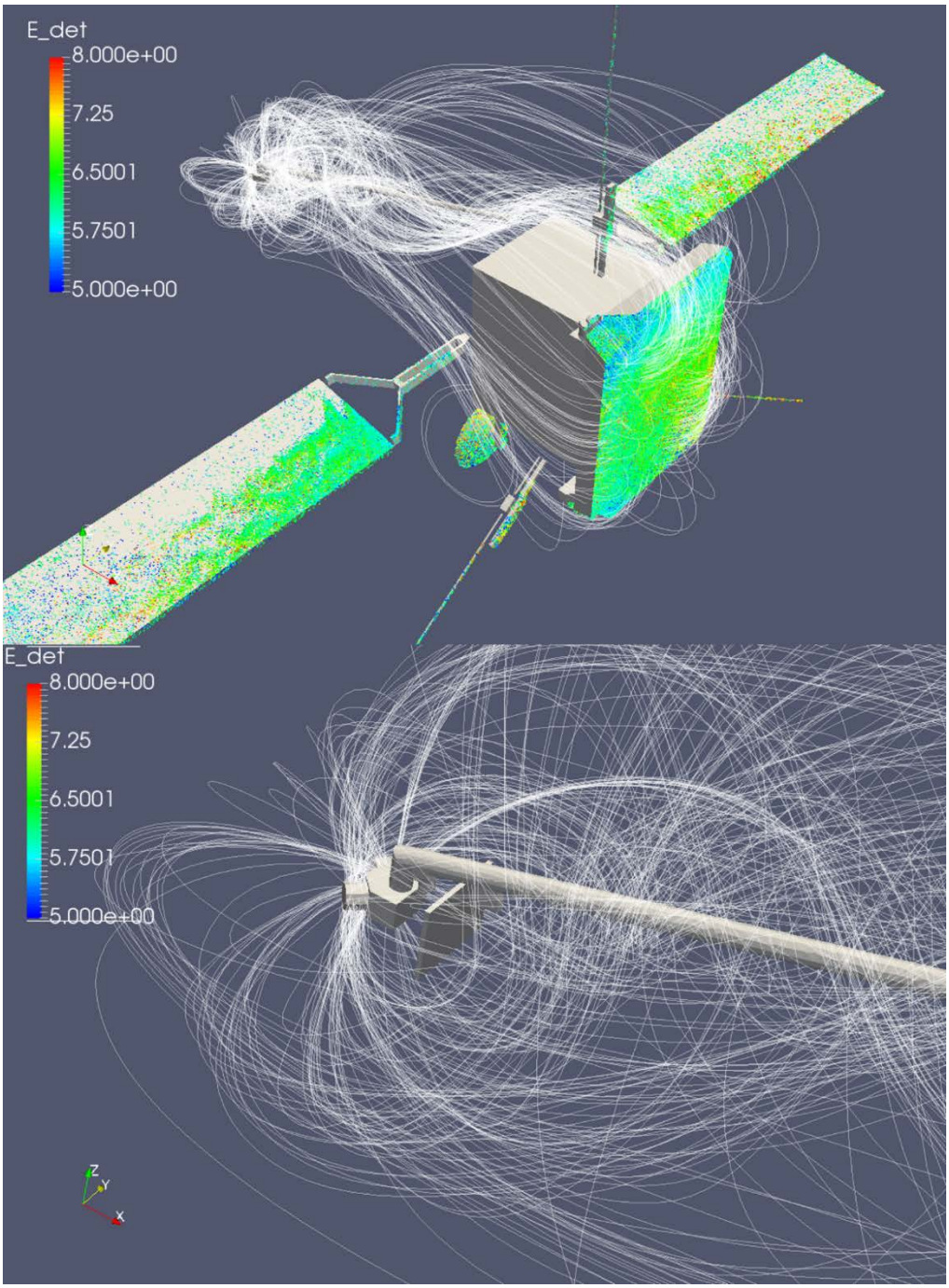

Figure 87: EAS Baffle Case - Trajectories of Photoelectrons with most important weight detected by EAS, combined to the origin of detected photoelectrons, and their energy at detection (in eV*). Top image is a global view of the system, with a focus on EAS displayed on the bottom image.*

Figure 87 illustrates this phenomenon, showing detected photoelectrons trajectories, curved by the baffle at its vicinity. The focus on EAS region on the bottom image illustrates the harvesting effect of the charged baffle surfaces on those particle trajectories, with a more complex rendering of photoelectrons paths in the vicinity of the instrument.

14. Conclusion on the SWA-EAS study

As detailed in the following section, this project achieved to comply to *almost* all SWA-EAS requirements for SPIS modelling.

Despite numerical issues of the SPIS code encountered when simulating both thin wires (for RPW antennas modeling) and particle detectors (for EAS) in the same the computational volume, which generated computation freezing and blocked situations, we could perform the necessary simulations using full 3D spacecraft CAD model, allowing us to bypass this bug, even though simulations lasted much longer than when using 1D wires. Note that the issue has been corrected since, but during our on-going work, and without verifications performed with validation or non-regression tests. This is why we could not use this version for this ESA study. This can however be performed later, through further simulations set up by MSSL teams for any future study with the latest SPIS version release (5.2.4).

This study provided answers to many questions raised from the EAS experiment. An adequate Solar Orbiter model including the desired EAS system and other modular elements (HGA, solar arrays, yokes, instruments, rear boom and the latest RPW model in 3D) was conceived and perfectly works. Another CAD model of the entire system including 1D RPW antennas has also been developed and should be tested by concerned users with the SPIS 5.2.4 version, checking if the bug correction did not generate any other inconsistency in the results. Our models are fully parametrized and easily modifiable. They have also been updated with latest data provided by ONERA concerning Elgiloy and Niobium materials photoemission properties, and simulations aiming at determining new stacer final potentials are on-going at LESIA. Those new RPW potentials might be more positive than the previous potentials obtained (between +2 and +3 V) and thus impact EAS measurements. This extension of the study has to be performed during another campaign of simulations by respective instrument teams.

However, and considering the material information available during this study, we could comply to *almost* all EAS requirements for SPIS modeling (see the next Section), providing EAS results of measurements and their interpretation, through extended analysis of SPIS outputs, for all the electron populations demanded.

This study also allowed to provide several tools and routines which permit the in-depth analysis of EAS simulation outputs. All required and necessary models and datasets were provided to MSSL and ESA in order to continue extended analysis of the spacecraft environment and its effects on the EAS measurements throughout the pre- and post-launch period.

15. EAS requirements for SPIS modelling: compliance table

The compliance table presenting EAS requirements for SPIS modelling and the corresponding achievements performed during this modelling work is displayed on the following pages.

Requirement Number	Requirement	Descriptive Explanation	Project Achievements
Spacecraft Model Requirements			
EAS-SPIS-0010	The project will provide a spacecraft model suitable for use in the SPIS toolkit and which appropriately supports the needs to assess the perturbations on the electron plasma environment.		Done. Spacecraft model provided to LESIA, MSSL and ESA
EAS-SPIS-0015	The model should include an adequately detailed description of the spacecraft boom and the sensors on the boom in their deployed configuration.		Done. All concerned surfaces included in the model provided to LESIA and ESA, together with EAS CAS model
EAS-SPIS-0020	The model should have the scope to include all spacecraft surfaces which will provide, or potentially may provide, a perturbation to the ambient electron environment.		Done. Model updated during the project. Latest relevant model provided. Elgilloy + Niobium material recent data on photoemission properties included in the latest model provided (but too late to be used in the here presented simulations)
EAS-SPIS-0025	The model should include all protective MLI on the spacecraft and within the material list.		Done. SC surfaces configuration used for simulations are listed in this report.
EAS-SPIS-0030	The spacecraft model will be sufficiently adaptable as to assess spacecraft wide perturbations on the large scale environment, and to assess detailed impact of individual perturbing surfaces, particularly those located near to the EAS apertures.		Done and assessed in all EAS simulations

EAS-SPIS-0040	An up-to-date model of the spacecraft	Updates of the current	Done. Every SC modification communicated during this study has been included in the CAD model. Only most recent photoemission parameters of RPW Elgiloy and Niobium have not been considered here (but now available on the latest CAD provided)
	should be generated to make sure that all important design modifications are included.	model will be required to include recent changes to the boom and bracket for SWA-EAS and movement of the STEIN instrument.	
EAS-SPIS-0045	The spacecraft model should be reviewed at regular intervals throughout the lifetime of the project to identify relevant design changes at spacecraft level.	For example, a review should be made after the completion of the delta-CDR to ensure design changes are captured.	Done, all model changes performed during this study have been reported and listed in this document
EAS-SPIS-0050	The spacecraft model development should remain flexible enough to include potentially relevant future changes.	Further changes may be required if, for example, the Prime introduces a series of baffles to the spacecraft design in order to address presently unresolved contamination issues.	Done. CAD model of spacecraft and its instruments are fully parametrized and can be easily updated. EAS baffle has also been included and tested in the here-presented simulations
EAS-SPIS-0060	The spacecraft model should be flexible and adaptable enough to provide the ability to assess the effect of movable surfaces (e.g. the HGA and the SA's) on the measurements of SWA-EAS.	It is anticipated that the orientation of these surfaces will continue to vary during the mission	Done. CAD model of spacecraft and its instruments are fully parametrized, including rotation properties of any movable surfaces
SWA EAS Modelling Requirements			
EAS-SPIS-0070	The project will construct a detailed model of the SWA-EAS sensor and its immediate environment such that a representative assessment of the impact of the spacecraft environment of the SWA-EAS measurements can be made.	May need to discuss the level of detail that needs to be included to achieve the representative results?	Done. EAS CAD model made, based on previous Airbud model, and adapted to this spacecraft model configuration in order to be fully integrated in simulations. Model has been provided to ESA and MSSL, with relevant configuration files of sensors
EAS-SPIS-0080	The modelling work should, as a minimum, be capable of assessing the impacts of the spacecraft ESC environment on ambient electrons in the range of 1 eV to 5 keV.	This is the operating energy range of the SWA-EAS instrument. [NR2]	Done. This is automatically performed by SPIS during simulations. Results analysis are here focused on lower energy ranges, considering the selected environment inputs for simulations.
EAS-SPIS-0090	The modelling work should be sufficiently accurate so as to reveal changes of the ambient electron energies from their undisturbed values at the level of 10%.	This reflects the dE/E of the SWA-EAS instrument. [NR2]	Partially done. The Energy Distribution Functions (EDF) provided by SPIS and treated through this work are precise enough to be integrated in order to recover further moments than density of the distribution of ambient electrons. Time constraints prevented us from extracting these aspects here. But SPIS provides automatically energies in outputs for every single particle detector
EAS-SPIS-0100	The modelling work should be sufficiently accurate so as to reveal changes of the ambient electron direction from their undisturbed trajectory at the level of better than 5 degrees.	This reflects the typical angular resolution of the SWA-EAS instrument. [NR2]	Done. Results provided in all EAS pointing maps for electrons thanks to the here developped Scilab routines

EAS-SPIS-0110	The modelling work should thus be capable of providing a ready comparison of the ambient electron 3D VDF with that expected to be measured by the SWA-EAS sensor in a given environment		Done and results provided through measured EDF presented and analyzed for all EAS cases
EAS-SPIS-0120	The model should be capable of identifying the detailed photo-electron emission profile of the Solar Orbiter surfaces in any given mission environment and be able to quantify the degree to which such electrons may contaminate the SWA-EAS measurements.		Done and results provided through measured EDF presented and analyzed for all EAS cases, as for EAS pointing maps, trajectories and origins of photoelectrons
EAS-SPIS-0130	The model should be capable of identifying the detailed secondary electron emission profile of the Solar Orbiter surfaces in any given mission environment and be able to quantify the degree to which such electrons may contaminate the SWA-EAS measurements.	This is particularly important for any surfaces located near the SWA-EAS apertures.	Done and results provided through measured EDF presented and analyzed for all EAS cases, as for EAS pointing maps, trajectories and origins of secondary electrons
EAS-SPIS-0130	A specific set of modelling runs should be undertaken, as early as practicable, to identify the detailed charging and the secondary electron emission profile, and their impact on the EAS measurements, of any baffle proposed to be mounted on the instrument boom as a means of mitigating the thruster contamination flux to EAS.	We should try to do this as soon as geometry and representative surface properties (initial bare surface and surface plus contamination film) can be identified.	Done thanks to last EAS simualtion case with baffle
EAS-SPIS-0140	The modelling work should thus be capable of providing a ready visualisation of the contribution of photo- and secondary electrons on top of the modifications to the ambient electron 3D VDF so that the latter can be compared with that expected to be measured by the SWA-EAS sensor in a given environment		Done and results provided for all the here-presented simulations in the EDF analyze sections
	Model Run Requirements		
EAS-SPIS-0150	The project should provide model runs which attempt to identify both the average conditions or impacts and the likely worst case conditions.	Including both the ambient worst case conditions and those associated with the worst case orientation of contaminating surfaces.	Partially done because of time constraints encountered with SPIS for modelling 1D RPW combined with particle detectors. Only average environment conditions are here considered
EAS-SPIS-0160	The project should provide model runs which address the range of distances to the Sun of 0.28-1.4 R_E, with priority to the perihelion distances	This is the range of distances over which SWA-EAS may be required to operate	Partially done because of time constraints encountered with SPIS for modelling 1D RPW combined with particle detectors. **But the priority to perihelion distance has been respected**
EAS-SPIS-0170	The model runs should provide a prediction of the overall spacecraft potential in a given environment, together with an assessment of the levels of differential surface charging.	This analysis will help verify the compliance of the spacecraft to SWA EID-B requirements. [NR3]	Done and results provided and analyzed for all EAS cases, respecting previous SC potentials obtained for the RPW study in this report
EAS-SPIS-0180	The model should provide a means to illustrate the trajectories of individual electrons into the SWA-EAS sensors given the spacecraft environment and ambient electric and magnetic fields		Done and results provided and analyzed for all EAS cases, using different illustrating methods such as EAS pointing maps, trajectories and origins of all electrons
EAS-SPIS-0190	The project shall have a deliverable which would allow continued analysis of the spacecraft environment throughout the post-launch period.	This is to allow the SWA-EAS instrument team to assess the effect of any unanticipated environment and/or evolution of the properties of problem surfaces throughout the mission.	Done. All CAD models, inputs, simulations packages, here-presented results and extended analysing tools (Scilab routines) have been provided to ESA and SWA-EAS teams in charge of future simulations